Mechanisms of Actomyosin Contractility in Cells

Matthew R. Stachowiak

Submitted in partial fulfillment of the
requirements for the degree of
Doctor of Philosophy
under the Executive Committee
of the Graduate School of Arts and Sciences

COLUMBIA UNIVERSITY

2011

ABSTRACT

Mechanisms of Actomyosin Contractility in Cells

Matthew R. Stachowiak

Many fundamental cellular processes hinge on the ability of cells to exert contractile force. Contractility is used by cells to divide, to migrate, to heal wounds, and to pump the heart and move limbs. Contractility is mediated by the actin and myosin cytoskeleton, a dynamic and responsive meshwork that assembles into various well-defined structures used by the cell to accomplish specific tasks. While muscle contraction is well-characterized, the contraction mechanisms of actomyosin structures in nonmuscle cells are relatively obscure. Here we elucidate the contraction mechanisms of two prominent and related actomyosin structures: the contractile ring, which constricts to divide the cell during cytokinesis, and the stress fiber, which is anchored to the extracellular matrix and allows the cell to exert contractile forces on its surroundings.

In the first part of the thesis, we develop a mathematical model to characterize the constriction mechanism of contractile rings in the *Schizosaccharomyces pombe* model organism. Our collaborators observed that after digesting the cell wall to create protoplasts, contractile rings constricted by sliding along the plasma membrane without cleaving the cell. This novel approach allowed direct comparison of our model predictions for the ring constriction rate and ring shape to the experimental data, and demonstrated that the contractile ring's rate of constriction is determined by a balance between ring tension and external resistance forces. Our results describe a casual relationship between ring organization, actin turnover kinetics, tension, and constriction. Ring tension depends on ring organization through the actin and myosin concentrations and their statistical correlations. These correlations are established and renewed

by actin turnover on a timescale much less than the constriction time so that rapid actin turnover sets the tension and provides the mechanism for continuous remodeling during constriction. Thus, we show that the contractile ring is a tension-producing machine regulated by actin turnover whose constriction rate depends on the response of a coupled system to the ring tension.

In the second part of the thesis we examine the contraction mechanisms of stress fibers, which have a sarcomeric structure reminiscent of muscle. We developed mathematical models of stress fibers to describe their rapid shortening after severing and to describe how the kinetics of sarcomere contraction and expansion depend on actin turnover. To test these models, we performed quantitative image analysis of stress fibers that spontaneously severed and recoiled. We observed that after spontaneous severing, stress fibers shorten by ~80% over ~15-30 s, during which ~50% of the actin initially present was disassembled. Actin disassembly was delayed by ~50 s relative to fiber recoil, causing a characteristic increase, peak, and decay in the actin density after severing. Model predictions were in excellent agreement with the observations. The model predicts that following breakage, fiber shortening due to myosin contractile force increases actin filament overlap in the center of the sarcomeres, which in turn causes compressive actin-actin elastic stresses. These stresses promote actin disassembly, thereby shortening the actin filaments and allowing further contraction. Thus, the model identifies a mechanism whereby coupling between actin turnover and mechanical stresses allows stress fibers to dynamically adjust actin filament lengths to accommodate contraction.

Contents

1. Introduction.....1

I. Cytokinesis and the Contractile Ring.....2

II. Stress fibers.....5

III. Outline.....6

2. Mechanism of Cytokinetic Ring Constriction in Fission Yeast.....8

I. Introduction.....8

II. Experimental Results.....11

III. Model of the Contractile Ring and Protoplast Constriction Kinetics.....15

IV. Model Results and Comparison to Experimental Data.....18

V. Discussion.....29

A. Experimental Procedures.....34

B. Detailed Description of the Contractile Ring Simulation.....36

3. Kinetics of Stress Fibers.....44

I. Introduction.....44

II. Model of Stress Fibers.....51

III. Stress Fiber at Constant Tension.....55

IV. Stress Fiber at Constant Length.....61

V. Application to Stress Fiber Relaxation Experiments.....69

VI. Discussion.....74

4. Recoil after Severing Reveals Stress Fiber Contraction Mechanisms.....80

I. Introduction.....80

II. Stress Fiber Forces.....83

III. Model of Severed Stress Fibers.....86

IV. Solutions of Model Equations.....90

V. Model Results and Comparison to Experimental Data.....91

VI. Discussion.....97

A. Equation for the Velocity Profile.....103

B. Equations and Solutions for the Sarcomere Profile and Collapsed Cap Length.....104

5. Coupling of Contraction and Actin Disassembly in Spontaneously Severing Stress Fibers.....106

I. Introduction.....106

II. Experimental Results.....109

III. Model of Stress fibers.....117

IV. Model Results and Comparison to Experimental Data.....121

V. Discussion.....124

A. Experimental Procedures.....127

6. Conclusion.....131

List of Figures

1.1 Actin, myosin, and sarcomeric structure....2
1.2 Cytokinesis and stress fibers....5
1.3 Outline of the systems studied in this thesis....7
2.1 Fission yeast protoplasts exhibit nodes and assemble contractile rings....12
2.2 Protoplast rings constrict by sliding along the membrane without septation....14
2.3 Model of protoplast constriction reproduces experimental constriction rates and ring shapes....19
2.4 Observed and prediction ring shapes in protoplasts....21
2.5 Best fit ring constriction profiles from 4 different models....22
2.6 Ring tension fluctuates in time, increases with increasing myosin concentration and is maximized for barbed end actin filament anchoring....23
2.7 Ring tension depends on the spatial organization of actin and myosin....25
2.8 Actin and formin turnover....28
2.9 Cross section of the simulated fission yeast contractile ring....37
3.1 Schematic of the stress fiber model....52
3.2 Proposed force-velocity relation for a nonmuscle myosin minifilament....53
3.3 Schematic of sequence of events during stress fiber relaxation....71
3.4 Comparison of model predictions for sarcomere length evolution to experimental data....72
3.5 Profile of sarcomere strengths for a stress fiber with 50 sarcomeres....73
3.6 Model predictions for the length evolution of all sarcomeres in a 50-sarcomere stress fiber....74
3.7 Sarcomere length profiles....74
4.1 Recoil of severed stress fibers....83
4.2 Force-length relations....85
4.3 Model of severed stress fibers....86
4.4 Recoil kinetics: model predictions compared to experimental results....92
4.5 Sequential sarcomere collapse....94

4.6 Evolution of the sarcomere length profile.....94
4.7 Force exerted by a severed stress fiber on its anchoring adhesion.....97
4.8 Effect of inhibition of myosin phosphorylation on stress fiber recoil.....101
4.9 Predicted recoil of severed stress fibers with different initial sarcomere lengths.....103
5.1 Stress fibers spontaneously fracture and recoil a constant fraction of their original length.....110
5.2 Recoil duration is independent of stress fiber length and contraction occurs uniformly along the fiber.....113
5.3 During recoil actin and other components are shed from the stress fiber while their densities increase.....115
5.4 Actin depolymerization lags behind recoil, causing the actin density to peak and then decay.....116
5.5 Mathematical model of stress fibers.....118
5.6 Effect of actin polymerization and depolymerization rates on recoil.....125

List of Tables

2.1 Parameter values used in the contractile ring simulation.....17

4.1 Parameter values used in the model of laser-severed stress fibers.....88

5.1 Parameter values used in the model of spontaneously severed stress fibers.....120

Acknowledgments

I wish to thank my adviser, Ben O'Shaughnessy, for dedicating himself tirelessly to our research. Without his expertise and commitment, this work would not have been possible. In the O'Shaughnessy group I was also fortunate to collaborate with Dr. Boris Guirao, Hayri Balcioglu, and my long term colleague Jason Warner.

I am also grateful to our collaborators Dr. Thomas Pollard and Dr. Caroline Laplante at Yale University, and Dr. Mary Beckerle, Dr. Mark Smith, Elizabeth Blankman, and Laura Luettjohann at the University of Utah. Their experimental efforts made my work far more interesting and satisfying.

Finally, I thank Alyssa DeSocio for her support and encouragement, without which I would have been lost.

To my parents.

Chapter 1

Introduction

Many fundamental cellular processes hinge on the ability of cells to exert contractile force. Examples include contractile force in cytokinesis to constrict the contractile ring and pinch the mother cell into two,[1] in cell motility to drag the cell forward,[2,3] in wound healing to help remodel the matrix,[4,5] in muscle contraction to pump the heart or move limbs,[6,7] and in damaged cells to repair the cytoskeleton.[8,9]

Contractility is mediated by the actin and myosin cytoskeleton. Actin proteins polymerize into double helical actin filaments (Fig. 1.1A). The heads of myosin-II motor proteins bind to actin filaments, and hydrolysis of ATP by myosin-II and release of the resulting free phosphate is associated with a conformational change in the myosin molecule that translates the myosin head and therefore also the bound actin filament.[10] By unbinding from the filament, releasing ADP, and going through successive hydrolysis cycles, myosin-II can translocate actin filaments. Since actin subunits are asymmetric, actin filaments are polar, and myosin-II always moves toward the "barbed end" and away from the "pointed end". Nonmuscle myosin-II proteins assemble into bipolar minifilaments (Fig. 1.1B).[11,12] Actin filaments, myosin filaments, actin filament crosslinking proteins, and other components assemble to form contractile actomyosin structures.

The "canonical" contractile machine is the myofibril in striated muscle, containing near-perfect interdigitated lattices of actin filaments and myosin filaments arranged precisely so that myosin causes contraction and tension rather than compression and expansion (Fig. 1.1C). The myofibril is built from many repeat units, or sarcomeres, arranged in series (Fig. 1.1C). In

nonmuscle cells, the actomyosin cytoskeleton forms contractile structures with far less ordered organization, and the organization and mechanisms have in most cases not been elucidated.

The aim of this thesis is to illuminate the mechanisms of contractility for two fundamentally important actomyosin structures in nonmuscle cells: (1) the contractile ring, which helps divide the cell during cytokinesis, and (2) stress fibers, which are actomyosin bundles similar in some respects to striated muscle.

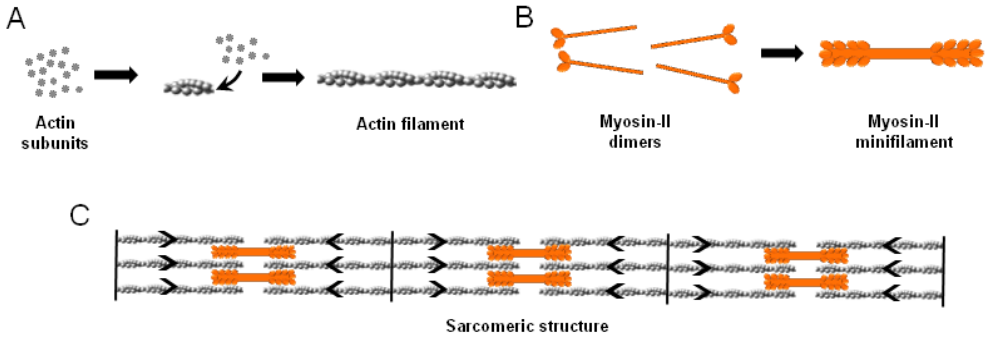

Figure 1.1: Actin, myosin, and sarcomeric structure.
(A) Actin proteins polymerize to form actin filaments.
(B) Myosin-II dimers assemble into minifilaments.
(C) Schematic of the basic sarcomeric structure. Vertical black lines: sarcomere boundaries. Myosin filaments (called "thick filaments" in muscle) reside in the center of sarcomeres, interacting with actin filaments on both sides. The actin filaments have alternating polarity (arrowheads point toward filament pointed ends), arranged so that when the myosin heads migrate toward actin filament barbed ends, contraction results. Muscle sarcomeres are ~2 μm long, while stress fiber sarcomeres are ~1 μm long. Muscle and stress fiber sarcomeres contain many other components, not pictured.

I. Cytokinesis and the Contractile Ring

Cytokinesis is the process whereby an actomyosin contractile ring pinches the mother cell into two daughters (Fig. 1.2A). It is the final stage of the cell cycle, following interphase (cell growth and DNA replication), prophase (chromosome formation), metaphase (chromosome alignment), anaphase (chromosome separation), and telophase (formation of two daughter nuclei). Constriction of the contractile ring is thought to be powered by actin-myosin interactions.

Importance

As an essential element of cell division, cytokinesis it is crucial to development of the embryo and the necessary replacement of cells which die through wear and tear in the adult.[1] Other roles include cell differentiation which can result from asymmetric cell division.[13] Failed cytokinesis has recently been proposed to play a role in tumorigenesis.[14-16] Additionally, inducing failure of cytokinesis in cancerous cells may have therapeutic potential since polyploidy can cause cell death.[17,18]

Fission yeast as a model organism for cytokinesis

Schizosaccharomyces pombe (fission yeast) is a widely used model organism for studying cytokinesis. Cytokinesis in fission yeast and animal cells is similar in many respects (Fig. 1.2A,B), as both entail formation and constriction of a contractile ring containing actin, myosin-II, α-actinin, formin, cofilin, and other conserved proteins.[19] The relative ease of manipulating the fission yeast organism has led to the measurement of a quantitative inventory of many key proteins in cytokinesis by using quantitative fluorescence microscopy,[20] offering a unique opportunity for quantitative mathematical modeling.

Assembly and constriction of the fission yeast contractile ring

Ring assembly begins during interphase when the anillin-like protein Mid1p exits from the nucleus and condenses into ~75 large membrane-associated protein complexes or "nodes" in a broad equatorial band near the nucleus.[21,22] After recruitment of myosin-II motor proteins, the nodes slowly diffuse in the membrane for ~10 min.[22] Then, the actin filament barbed end capping protein formin Cdc12p is recruited and nucleates a dense meshwork of actin filaments

connecting the nodes. A dynamical transition occurs, and nodes start to move coherently in stop-start motions, powered by forces from myosin-II, while condensing into a compact contractile ring over ~10 min.[22]

Following assembly, during anaphase, a ring maturation episode lasting ~25 min occurs during which capping protein Acp2p, myosin II isoform Myp2p, septin Spn1p and other proteins are recruited.[23] At the end of anaphase, the ring constricts over ~20-30 min.[23,24] During constriction, actin-binding proteins IQGAP Rng2p, formin Cdc12p, Cdc15p and α-actinin Ain1p maintain nearly constant concentration, i.e. they are shed in proportion to ring volume, while the concentration of myosin-II increases.[20]

Septation

Unlike animal cells, in fungi such as fission yeast the plasma membrane is surrounded by a cell wall made of a dense network of polysaccharides that provides mechanical protection, opposes turgor pressure and determines cell shape.[25] Thus, during cytokinesis in fission yeast the daughter cells must each be provided with intact cell walls. This is accomplished by the process of septation, the deposition of new cell wall in the wake of the constricting ring (Fig. 1.2B).[26,27] Thus, ring constriction and septation dynamics are directly coupled.

When the fission yeast cell wall is digested enzymatically, cells become swollen and spherical, and are called "protoplasts".[28-30] In previous work, complete contractile rings were observed at various latitudes in fixed protoplasts.[29] Thus, protoplasts may be a useful model system to study ring constriction in the absence of septation.

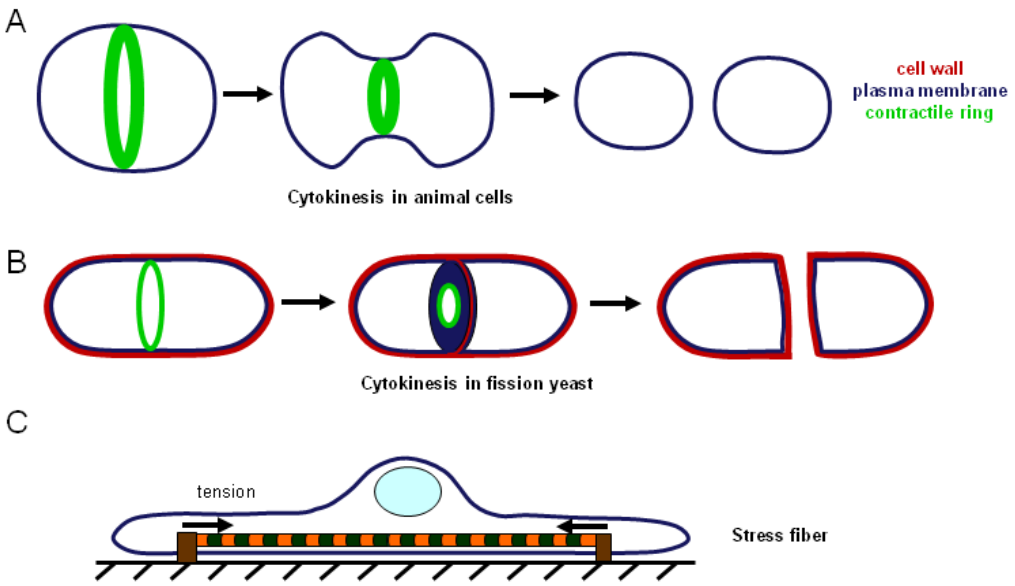

Figure 1.2: Cytokinesis and stress fibers.
(A) Cytokinesis in animal cells. The contractile ring pinches the cell into two daughter cells. The initial ring circumference is very roughly 20-100 μm.[31]
(B) Cytokinesis in fission yeast cells which have a cell wall. As the contractile ring constricts, new cell wall grows in the wake of the constricting ring in the process of septation. The initial ring circumference is ~10 μm.
(C) Illustration of a stress fiber (alternating green and orange bands indicate sarcomeres) anchored at each end by a transmembrane focal adhesion (brown) connected to the extracellular matrix. The stress fiber generates tension via myosin-mediated contraction.

II. Stress Fibers

Stress fibers are tensile actomyosin bundles often anchored at each end to the extracellular matrix via transmembrane protein complexes called focal adhesions (Fig. 1.2C).[32] Stress fibers mediate adhesion to the basal lamina in vascular endothelial cells under shear stress,[33,34] generate contractile forces in myofibroblasts during wound healing,[4,5] help orient the matrix in the developing intervertebral disk,[35] may provide tendons stability against stretch[36] and are associated with hepatic stellate cell activation which has a crucial role in liver fibrosis.[37,38] Considerable evidence suggests that stress fibers in stationary cells have periodic sarcomeric structure similar to striated muscle but somewhat less ordered: actin polarity is periodic[39] and regions of the actin cross-linking protein α-actinin alternate with myosin-rich regions along the

fiber axis.[40,41] Unlike striated muscle, stress fiber components are highly dynamic, with actin turning over on a time scale of several minutes.[42-44]

III. Outline

In Chapter 2 of this thesis, we present a mathematical model of contractile ring constriction during fission yeast cytokinesis. Studying ring constriction in fission yeast protoplasts that lack cell wall allowed us to investigate constriction in the absence of the complicated septation process (Fig. 1.3A). This allowed us to interrogate ring constriction mechanisms in a way not possible at present with normal yeast cells. This work was performed in collaboration with the laboratory of Dr. Thomas Pollard at Yale University.

Chapters 3-5 deal with stress fibers. In Chapter 3, we modeled an experiment in which stress fibers in living cells were treated with a drug that increases myosin-II activity, causing peripheral sarcomeres in stress fibers to contract and central sarcomeres to expand over ~5 min (Fig. 1.3B).[41] Since this relaxation time is of the same order as the actin turnover time, we hypothesized that contraction and actin turnover may be coupled. Our model therefore outlines a general mechanism of force-turnover feedback. In Chapter 4, we model an experiment in which severing of a stress fiber in a living cell with a laser was followed by rapid recoil of the stress fiber (Fig. 1.3C).[44] Our analysis suggested that stress fibers may contract non-uniformly after severing because of viscous coupling to the surrounding cytoplasm. Because there was a lack of quantitative experimental measurements of stress fiber dynamics, we initiated a collaboration with the laboratory of Dr. Mary Beckerle at the University of Utah. Results of this collaboration are presented in Chapter 5. We observed that stress fibers spontaneously sever and recoil in living cells (Fig. 1.3D). We performed quantitative image analysis and showed that actin

disassembly is directly coupled to contraction, as predicted by our model in Chapter 3. Our model therefore illuminates the mechanisms of contractility in stress fibers.

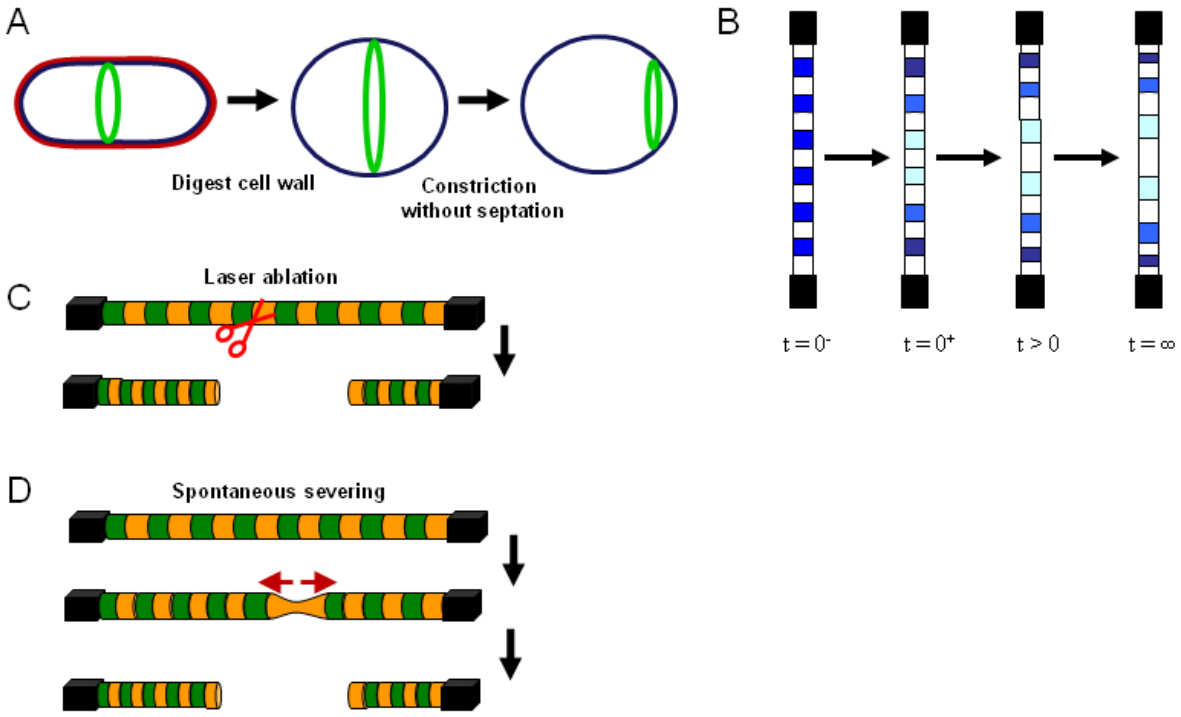

Figure 1.3: Outline of the systems studied in this thesis.
(A) Contractile rings constrict without septation in fission yeast protoplasts that lack cell wall (Chapter 2).
(B) Stress fibers treated with a myosin-activating drug contract in their peripheral regions and expand in their central regions (Chapter 3).
(C) Stress fibers recoil after being severed by laser ablation (Chapter 4).
(D) Stress fibers spontaneously sever and recoil (Chapter 5).

Chapter 2

Mechanism of Cytokinetic Ring Constriction in Fission Yeast

In this chapter, we describe collaborative work that combines experiments on fission yeast protoplasts lacking a cell wall with computer simulations to characterize the mechanism of cytokinetic contractile ring constriction. We performed the analysis and mathematical modeling, and Dr. Caroline Laplante in Dr. Thomas Pollard's laboratory at Yale University performed the experiments.

I. Introduction

Animal, fungal and amoeboid cells accomplish cytokinesis by constriction of an actomyosin contractile ring composed of widely conserved components.[19] Myosin-II motor proteins generate tension that drives constriction by binding to and pulling upon actin filaments.[45,46] The fission yeast *Schizosaccharomyces pombe* offers a unique opportunity to model ring constriction mathematically as more than 130 genes involved in cytokinesis have been identified and the amounts of many proteins in the ring were measured.[20,47] Ring assembly in fission yeast is known to occur via coalescence of ~75 membrane-anchored precursor nodes, protein assemblies that contain many structural and functional components of the ring.[21] Nevertheless, the biophysical mechanisms underlying ring constriction are poorly understood.

A critical question is how ring tension emerges from the spatial organization of actin and myosin. The highly ordered architecture of skeletal muscle is based on the sarcomere repeat unit that contains myosin-II and polarized actin filaments precisely arranged to generate tension. By

contrast, optical imaging of fission yeast contractile rings reveals no periodicity[24,48,49] and electron microscopy (EM) shows bundled actin filaments of mixed polarity at the base of the cleavage furrow[50] that appear to be randomly positioned[51]. Tension presumably depends on the relative positions and orientations of the actin and myosin, but in non-sarcomeric organizations this dependence has not yet been elucidated.

Anchoring of the ring to the cell membrane is thought to transmit tension and direct cytokinesis[52]. The strength of the anchoring and the anchor identities are unknown, but candidates include the membrane binding F-BAR protein Cdc15p, the integral membrane protein Chs2p and the glucan synthase Bgs1p that builds cell wall.[49,53,54] If the anchors have low mobility, other ring components that bind to these anchors would be effectively immobilized. Actin barbed ends may be anchored in this manner because the formin Cdc12p, which associates processively with growing actin filament barbed ends,[55] binds to candidate anchor Cdc15p.[56] Myosin-II may also be anchored as it remained localized to the division site after actin disassembly in animal cells[57] and fission yeast.[58] Whether or not these components are anchored is presumably relevant to the ring's tension-producing capability.

During constriction the contractile ring continuously remodels as its volume decreases.[59] Actin-binding proteins α-actinin Ain1p, Cdc15p and IQGAP homologue Rng2p are lost from the ring in proportion to the decrease in ring length, suggesting that filamentous actin is maintained at constant density by disassembly.[20] This could be achieved by continuous depolymerization of a fixed number of actin filaments as proposed for *C. elegans*.[31] However, high doses of the actin monomer sequestering agent latrunculin A (LatA) disintegrated all contractile rings in fission yeast in ~1 min, suggesting that polymerization also occurs.[24] Indeed, the mechanism of tension production may be coupled to polymerization as constriction was slower when actin

polymerization was suppressed.[24] While the actin remodeling mechanisms have not been characterized, normal constriction requires the actin filament nucleator formin Cdc12p and the actin severing protein cofilin Adf1p.[24,60]

Mathematical models are required to establish the ring constriction mechanism. Recent models proposed that constriction is driven by myosin, cortical tension and actin turnover and resisted by other factors including cytoplasmic viscosity, cell elasticity and actin crosslinkers.[61-63] However, a detailed model of the ring built from known molecular components is not presently available. Such a model is within reach for fission yeast because a quantitative inventory of ring proteins has been measured.[20] Nevertheless, predicting the constriction rate is problematic because constriction in yeast is closely coupled to septation, the poorly understood process of cell wall deposition in the wake of the constricting ring.[27] The constriction rate could be set by the response of the growing septum to ring tension. Alternatively, the ring could be dynamically autonomous, as proposed in a model for *C. elegans* embryos where the ring retained memory of permanent structural properties that determined its constriction rate.[31]

Here, we combined mathematical modeling and experimental study of the fission yeast contractile ring to elucidate constriction mechanisms decoupled from septation. In yeast protoplasts that lack cell wall,[29] we found that contractile rings constrict without septation by sliding along the plasma membrane. By comparing observations to predictions of a computer simulation of the ring that incorporated the key molecular components, we could isolate the mechanisms of ring constriction. Our results describe a causal relationship between actin turnover kinetics, ring organization, tension and constriction rate. Ring tension depends on its organization through the actomyosin component densities and their statistical correlations of sarcomeric character. The organization is renewed by actin turnover on a timescale much less

than the constriction time. Thus, rapid actin turnover sets the tension and provides the mechanism for continuous remodeling during constriction. By deforming protoplasts, we demonstrated that ring constriction rates and shapes depend on protoplast surface shape and result from tension working against external forces. Thus, the contractile ring is a tension-producing machine regulated by actin turnover whose constriction rate depends on the response of a coupled system to the ring tension.

II. Experimental Results

Fission yeast protoplasts exhibit nodes and assemble actomyosin contractile rings

To study the fission yeast contractile ring in the absence of septation, we prepared protoplasts by treating cells with lytic and lysing enzymes to digest the cell wall. Protoplasts lose the characteristic elongated morphology of fission yeast and adopt a rounded shape (Fig. 2.1A,B). In intact cells, actin patches visualized with the calponin homology domain of Rng2p fused to GFP (GFP-CHD)[64] localize to the poles and are hallmarks of polarized growth (Fig. 2.1C).[65] In protoplasts actin patches were distributed throughout the entire cortex, consistent with a loss of cell polarity (Fig. 2.1D).

We used time-lapse microscopy to investigate contractile ring assembly in protoplasts expressing the myosin-II regulatory light chain fused to three molecules of GFP (Rlc1-3GFP). Rlc1-3GFP concentrated in cortical puncta indistinguishable from the nodes that serve as ring precursors in intact cells.[21] Over the ~1 min time of observation, nodes in protoplasts underwent either 2-dimensional diffusion or stochastic, directed, stop-go motions. Diffusing nodes had a linear increase in their mean squared displacement (MSD) with time, $MSD(t) = MSD(0) + 4Dt$ (Fig. 2.1E). The diffusion constant, D, was 28.2 ± 3.1 nm^2/s (mean ± SEM, n = 75 nodes, 15

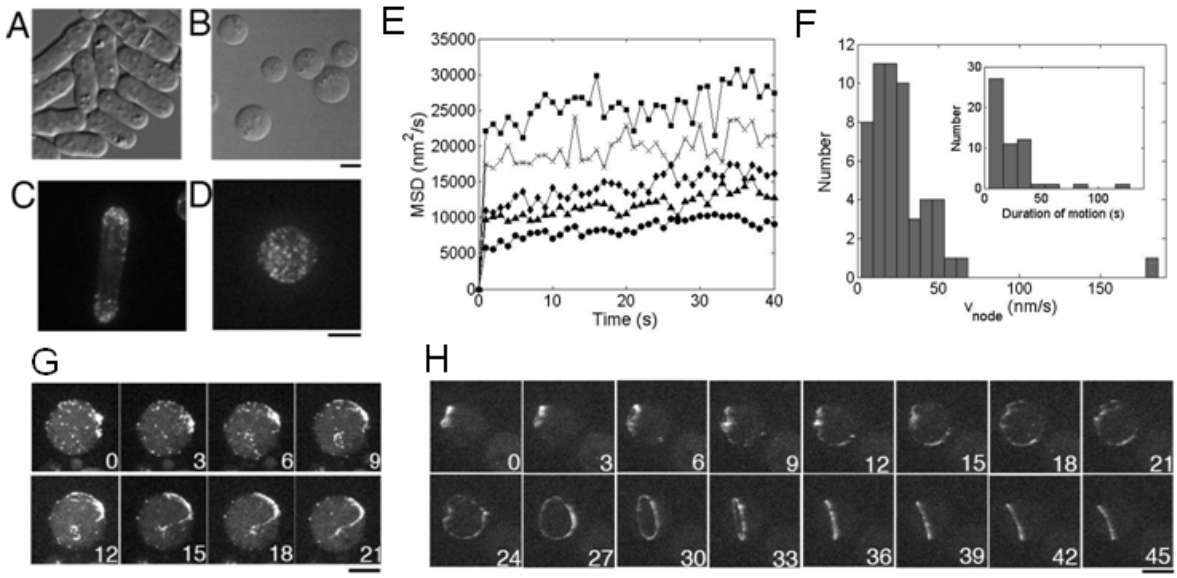

Figure 2.1: Fission yeast protoplasts exhibit nodes and assemble contractile rings.
(A and B) Differential interference contrast (DIC) micrographs of (A) intact fission yeast cells and (B) protoplasts.
(C and D) Actin patches visualized by GFP-CHD localize to intact cell poles (C), but distribute uniformly in protoplasts (D).
(E) MSD of 5 diffusing protoplast nodes.
(F) Velocity distribution of protoplast nodes undergoing directed motion. Inset: durations of motion.
(G and H) Rlc1p-3GFP protoplast nodes coalesce into a filament (G), and a ring assembles from an Rlc1p-3GFP filament originating from a disassembling ring (H). Time, min.
Fluorescent micrographs are z-stack projections taken on a spinning disk confocal microscope. All micrographs from C. Laplante and T.D. Pollard (Yale University). Scale bars: 10 μm.

cells), corresponding to a node drag coefficient γ_{node} of 150 pN·s/μm using the Einstein relation $\gamma_{node} = k_B T/D$. Nodes undergoing stop-go motions had mean velocity v_{node} = 27.3 ± 3.5 nm/s in bursts lasting ~22 s (n = 54 nodes, 13 cells, Fig. 2.1F). The average force exerted on each node is then $f_{myo} = \gamma_{node} v_{node} \approx 4$ pN. Thus, in protoplasts the node drag coefficient, velocity, duration of motion and force all lie within 25% of the values reported in intact cells.[22]

In intact cells, precursors of the contractile ring first appear in nodes forming a band around the cell equator. These nodes first undergo diffusion, followed by stop-go motion as they condense into a ring during mitosis. By contrast, protoplast nodes are distributed over the entire cortex (Fig. 2.1G). While we observed protoplast nodes condense into strands (Fig. 2.1G), we

did not directly observe nodes form a continuous ring. Instead, rings formed in various ways from long strands marked with Rlc1p-3GFP, including coalescence of separate short strands (n = 2), emergence of long strands from clusters of Rlc1-3GFP (n = 2) or growth from disassembling rings (Fig. 2.1H; n = 2).

Protoplast rings are tensile and constrict without septation in a myosin-dependent manner

The contractile ring in intact cells lies at the leading edge of the septum that grows between the two daughter cells, while protoplasts did not form septa nor cleave. Nevertheless, rings constricted in protoplasts by sliding against and deforming the plasma membrane, suggesting that the rings generated tension (Fig. 2.2A,B). The rings contained both myosin-II marked with Rlc1p-tdTomato and actin filaments labeled with the calponin homology domain of Rng2p fused to GFP (GFP-CHD) (Fig. 2.2C). The equatorial circumference of protoplasts was L_{proto} = 18.9 ± 1.1 μm (n = 7), almost twice that of intact cells (~11 μm). The ring constriction rate in protoplasts (rate of decrease of ring length) increased over time and had a time-averaged value of 0.22 ± 0.04 μm/min (n = 7), slightly less than the rate in intact cells, 0.30 ± 0.02 μm/min (n = 4, p = 0.09, Fig. 2.2D). Rings in temperature-sensitive *myo2-E1* protoplasts, in which a mutation in the actin-binding region of Myo2p causes weak binding to actin filaments in vitro,[66] constricted with a mean rate 0.08 μm/min, 2.6 fold slower than wild-type protoplasts (n = 3, p = 0.04, Fig. 2.2D). Thus, protoplast ring constriction depends on myosin-II.

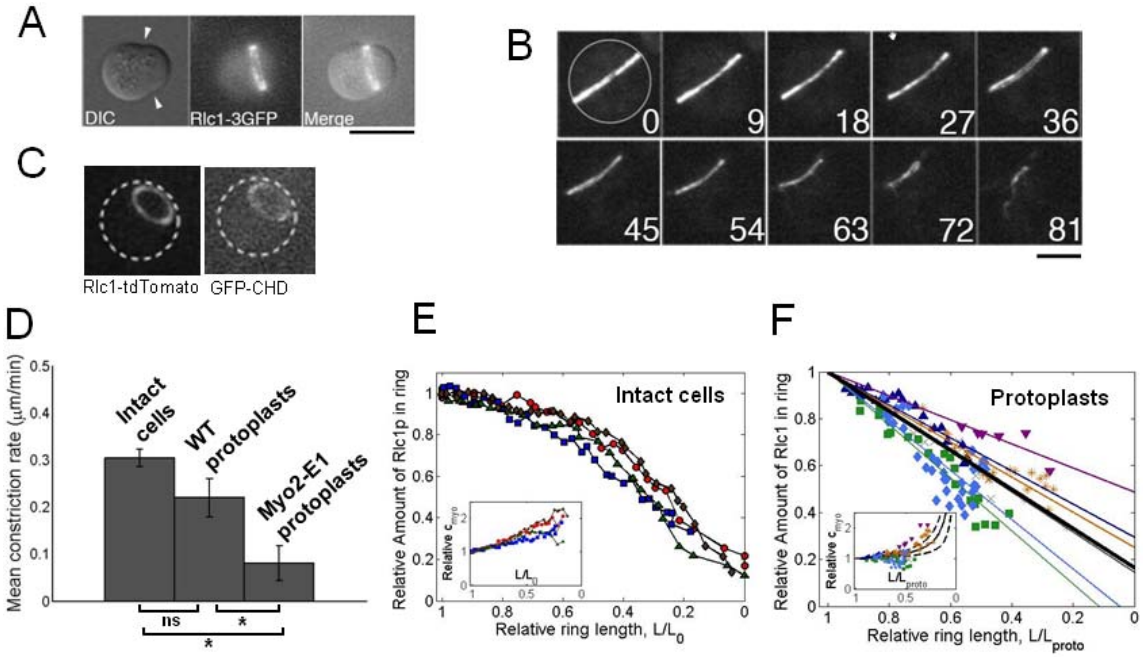

Figure 2.2: Protoplast rings constrict by sliding along the membrane without septation.
(A) The membrane is deformed where the contractile ring attaches (arrowheads), showing that the ring generates tension.
(B) Constriction of an Rlc1-3GFP protoplast ring (time, min).
(C) Myosin light chain Rlc1p-tdTomato and actin marker CHD-GFP colocalize in a protoplast ring.
(D) Ring constriction rates are similar in intact cells (n = 4) and wild-type protoplasts (n = 7) but reduced in *myo2-E1* mutant protoplasts (n = 3, mean ± SEM). Asterisks: statistical significance of $p < 0.05$; ns: not significant.
(E) Total myosin in the ring (Rlc1p-3GFP fluorescence, normalized to value at constriction onset) versus relative ring length for 4 intact cells. Inset: relative myosin concentration (fluorescence per ring length).
(F) As (E), but for 6 protoplasts. Each symbol denotes a different protoplast. Thin solid lines: best fit linear relations. Myosin amount is relative to value at $L = L_{proto}$ assuming a linear relation. Solid line: mean of best fit lines. Inset: relative concentration, showing mean (solid line) ± SEM (dashed lines).
Fluorescent micrographs, as for Fig. 2.1 except (A), epifluorescence wide field microscope. Protoplast boundary outlined in (A) and (B). All micrographs from C. Laplante and T.D. Pollard (Yale University). Scale bars: 10 μm.

During ring constriction the amount of myosin-II decreases but the concentration increases

Quantitative measurements of Rlc1p-3GFP fluorescence in both intact cells and protoplasts showed that myosin-II became more concentrated in rings as they shortened, although the total amount of myosin-II declined (Fig. 2.2E,F).[20] In intact cells, shedding of

myosin-II from the ring was faster during the latter half of the process, while the rate was almost constant for a given protoplast but more variable between protoplasts. The mean rate of myosin-II loss was similar in protoplasts (8.3% myosin loss per 10% ring shortening relative to initial length) and intact cells (8.6% loss per 10% shortening) and is a key input to our mathematical model of the ring.

III. Model of the Contractile Ring and Protoplast Constriction Kinetics

We developed a stochastic computer simulation of the fission yeast ring and applied it to constriction in protoplasts. The simulation makes testable predictions and outputs results that we directly compare to our experimental observations and those of prior studies. Table 2.1 summarizes the parameter values and Appendix B provides a detailed description of the model. In accordance with the quantitative inventory of ring proteins in fission yeast, formin, myosin, and α-actinin have concentrations equal to their directly measured values (see Table 2.1).

Ring organization. The model (Fig. 2.3A) is based on experiments suggesting that actin filaments and myosin-II appear to be randomly organized and anchored directly or indirectly to the plasma membrane. Accordingly, clusters of myosin-II oligomers are anchored to the membrane at random locations, and the concentration of myosin-II as a function of ring length is set by our relative measurements in protoplasts (Fig. 2.2F) after setting the concentration at the maximum ring length to the value in intact cells (Table 2.1). Actin filaments are randomly nucleated by formin Cdc12p, uncorrelated with the locations of myosin-II oligomers, the simplest assumption consistent with experiment. We also examined other possible random

organizations where correlations are present due to biased actin nucleation statistics, including the node-like arrangement in which actin barbed ends and myosin-II colocalize (see below).

Actin and formin turnover. After binding at random locations around the ring, formin Cdc12p instantly nucleates and grows actin filaments (Fig. 2.3B). Following the addition of an ATP-actin subunit to a filament, *S. pombe* actin hydrolyzes the bound ATP and dissociates the γ-phosphate in <10 s.[67] Since we predict below that actin turns over in ~11 s, and since cofilin Adf1p binding can accelerate phosphate release >10 fold,[68] we assume that most subunits are ADP-actin and that cofilin binds and severs with equal probability at any filament location. Thus the total severing probability increases with length, consistent with cofilin severing kinetics of ADP-actin measured in vitro.[69] We assume that segments severed from distal ends exit the ring as observed in vitro.[70]

In the model formin Cdc12p dissociates from rings with rate constant k_{off}^{for} = 0.023 s^{-1}, directly measured by fluorescence recovery after photobleaching (FRAP) (Fig. 2.8A).[71] The associated actin filament is assumed to exit the ring with its formin, since the barbed end residence time of formin Cdc12p measured in vitro exceeds 1000 s.[55]

We determined the parameters defining actin filament nucleation, growth and severing rates by demanding that model predictions matched 3 experimental measurements in intact cells: the initial formin concentration, the number of actin filaments in the ring cross-section, and the total ring disintegration time after LatA-induced actin polymerization shutdown (see Table 2.1). The latter was determined in the simulation by setting the polymerization rate to zero and recording the time when 90% of the initial actin had left the ring (Fig. 2.8B).

Forces in the ring. At steady state, these dynamic events generate a random organization (Fig. 2.3A). Myosin oligomers bind actin filaments that grow within reach and pull with a force

Table 2.1: Parameter values in the contractile ring simulation

Symbol	Meaning	Value	Legend
	Parameter values		
d	Ring thickness	0.2 μm	**(A)**
d_α	Actin filament lateral spacing: length of α-actinin crosslinks	35 nm	**(B)**
c_{myo}^0	Initial myosin-II heavy chain concentration	20 μM (3000 heavy chains per 10 μm of ring length)	**(A)**
n_{myo}	Number of myosin-II heavy chains per myosin cluster	40	**(C)**
n_{oligomer}	Number of myosin oligomers per cluster	2	**(D)**
f_{myo}	Myosin oligomer force when fully overlapped with actin	2.75 pN	**(E)**
w_{myo}	Myosin oligomer length	0.3 μm	**(F)**
ζ_α	α-actinin drag coefficient per unit length of actin filament overlap	9.4 pN·s/μm^2	**(G)**
$k_{\mathrm{off}}^{\mathrm{for}}$	Formin off rate	0.023 s^{-1}	**(H)**
r_{nuc}	Actin nucleation rate per ring length	20.8 μm^{-1} min^{-1}	**(I)**
r_{sev}	Actin severing rate per filament length by cofilin	1.8 μm^{-1} min^{-1}	**(I)**
v_{pol}	Formin-mediated barbed end actin polymerization rate	70 nm/s (26 subunits/s)	**(I)**
γ_{ring}	Ring-membrane drag coefficient	289 nN·s/μm	**(J)**
	Experimental measurements to which simulation results were fit to determine r_{nuc}, r_{sev}, and v_{pol}		
	Initial formin Cdc12p concentration	3 μM (150 formin dimers per 10 μm of ring length)	**(A)**
	Time for ring disintegration after large dose of LatA	55 s	**(H)**
	Number of actin filaments in the bundle cross section	20	**(K)**

Legend:

(A) From Wu and Pollard, 2005.[20]

(B) From Meyer and Aebi, 1990.[72] See also Fig. 2.9.

(C) Assumed the same as the number of heavy chains per node.[20] This, combined with the value for c_{myo}^0, results in 75 myosin clusters per 10 μm of ring length.

(D) Assuming that each myosin oligomer contains 20 heavy chains. Our results are not qualitatively affected by n_{myo} and n_{oligomer}, which have not been measured in fission yeast.

(E) Chosen to give an average force of 4 pN per myosin cluster, which matches our measured value of the force between nodes (see Fig. 2.9).

(F) From Verkhovsky and Borisy, 1993.[11]

(G) $\zeta_\alpha = \frac{1}{2}\rho k_\alpha \tau_{\mathrm{off}}$. ρ = 2.5 μm^{-1} is the crosslink density in intact cell rings given 250 α-actinin crosslinks and 150 actin filaments,[20] with 20 filaments in cross section[50]; k_α = 25 pN/μm is α-actinin crosslink shear stiffness estimated from in vitro actin-α-actinin bundles;[73] $\tau_{\mathrm{off}} \approx 0.3$ s is average crosslink lifetime.[74]

(H) From Yonetani et al, 2008,[71] Fig. 2.8.

(I) Fit to previous measurements of rings in intact cells.

(J) Fit to measured protoplast ring constriction curves (Fig. 2.3F).

(K) Estimated from published electron micrographs.[50] Together with the formin concentration, this implies a mean actin filament length of ~1.3 μm

proportional to the actin-myosin overlap up to a maximum force f_{myo} inferred from our measurements of node motions in protoplasts (Fig. 2.3C and Table 2.1). A second class of force is viscous drag due to the dynamic crosslinker Ain1p α-actinin that opposes relative filament motion with drag coefficient ζ_α per unit length (Fig. 2.3C and Table 2.1). Therefore, ring forces are stochastic as they depend on random relative positions of actin and myosin and are continuously updated due to filament turnover.

Ring Constriction. We calculated the ring tension at each ring length, $T(L)$, a valid procedure as constriction lasts much longer (~30 min) than the time for ring organization to attain steady state (~30 s, the formin turnover time). In protoplasts, rings constrict by sliding along the membrane (Fig. 2.2B), so we tested a model in which tension-driven ring sliding is resisted by drag forces due to anchors that connect the ring to the membrane with drag coefficient γ_{ring} (Fig. 2.3D). Balancing these forces, we calculated the constriction rate and hence the constriction profile $L(t)$ (Fig. 2.3F).

IV. Model Results and Comparison to Experimental Data

The fission yeast ring tension is tens of pN and increases during constriction due to the increasing myosin-II concentration

Rings in protoplasts slide along and deform the membrane, suggesting that the ring is tensile (Fig. 2.2A,B). We used the model to calculate tension during constriction. As expected, tension fluctuated considerably in time due to the constantly fluctuating ring organization. Initially, when the ring length equaled the protoplast circumference, tension fluctuated about a mean value $T = 37$ pN with standard deviation 5.4 pN on a timescale ~18 s (Fig. 2.6A), similar to

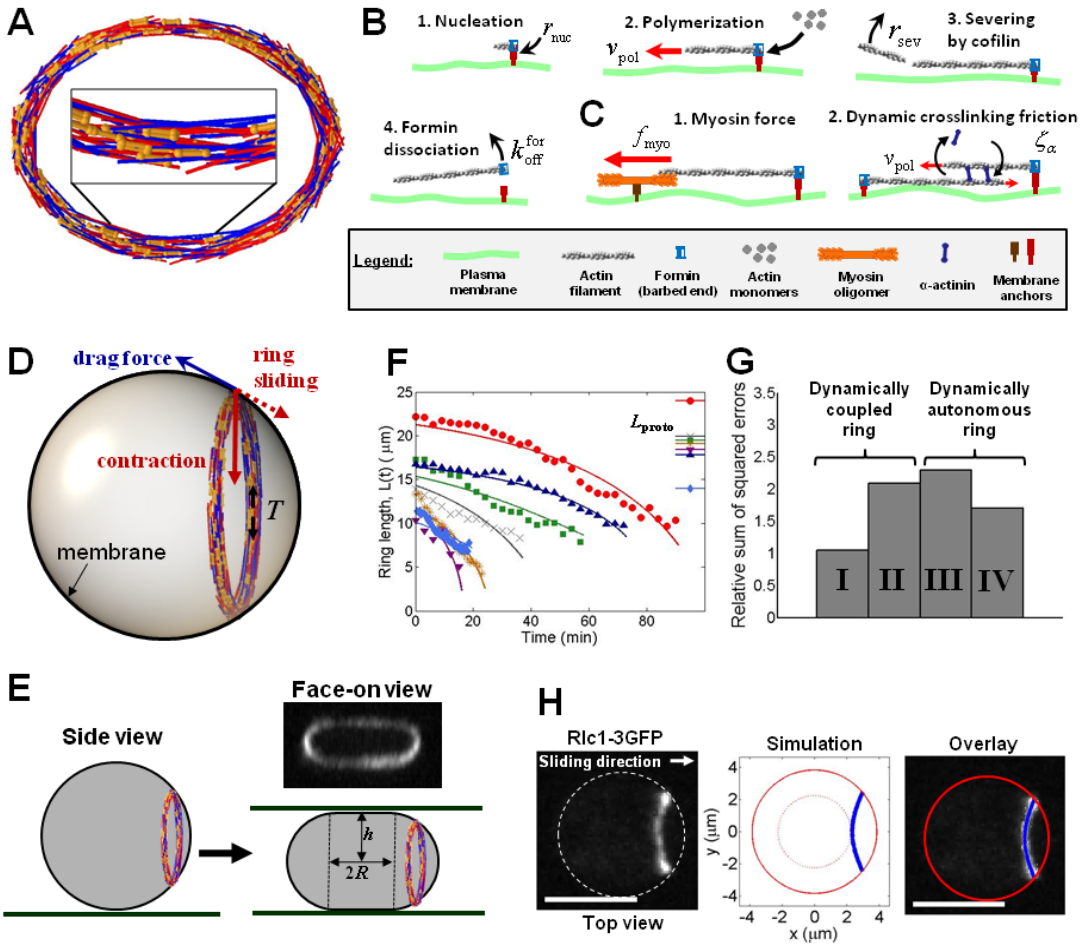

Figure 2.3: Model of protoplast constriction reproduces experimental constriction rates and ring shapes

(A) Computer simulation of the fission yeast contractile ring. Randomly positioned myosin-II oligomers (orange) interact with randomly positioned actin filaments of random polarity (red or blue). Myosin and actin are anchored. Parameters, as in Table 2.1.

(B) Actin turnover processes. Formin-mediated nucleation (r_{nuc} per ring length) and growth (polymerization velocity v_{pol}), cofilin-mediated severing (r_{sev} per filament length), formin dissociation (k_{off}^{for}).

(C) Forces that determine ring tension. Anchored myosins pull barbed-end-anchored actin filaments (tensile). Frictional drag from dynamic α-actinin crosslinkers (coefficient ζ_α per length) opposes relative motion of growing filaments (compressive).

(D) Force balance determines protoplast ring constriction dynamics. Ring tension T produces contraction force (red arrow) whose tangential component (dashed red arrow) drives ring sliding. Ring anchor drag forces oppose sliding (blue arrow).

(E) Protoplasts were deformed with coverslips and the shape characterized (radius R of flat portion, half protoplast height h). Top right: face-on view (maximum projection) of an Rlc1p-3GFP ring in a deformed protoplast.

(F) Protoplast ring constriction histories. Discrete markers: experiment. Solid lines: model fits of the tension-anchor drag model using constant total ring-membrane drag coefficient γ_{ring} as fitting parameter. Cell circumference shown at right. Other parameters, as in Table 2.1.

(G) Sum of squared residuals for fits to experimental constriction curves of (F) using different models. (I) Constant total drag coefficient model (shown in (F)). (II) Total drag proportional to ring length. (III) Constant constriction rate proportional to initial ring length. (IV) Constriction rate proportional to myosin concentration. Error values are relative to (I). All parameters except the fitting parameter γ_{ring}, as in Table 2.1. See also Fig. 2.5.

(H) Observed (left, Rlc1p-3GFP, maximum projection) and predicted (center, blue) shape of a constricting ring in a deformed protoplast, viewed from above (corresponds to the orange asterisks in (F) at t = 7 min, having h = 1.6 μm and R = 2.3 μm). Dashed white, solid red lines: cell boundary. Dotted red line: boundary of flat portion of cell. All parameters in the simulation from Table 2.1. Bar: 5 μm. See also Fig. 2.4.

All micrographs from C. Laplante and T.D. Pollard (Yale University).

the actin turnover time. Tension increased throughout constriction, reaching ~85 ± 27 pN after the ring had shortened by 80% (Fig. 2.6B). Tension is dominated by myosin forces that increase in direct proportion to the myosin concentration (Fig. 2.2F Inset and 2.6B Inset). A second, smaller component from dynamic α-actinin crosslinks contributes a nearly constant compression of ~35 pN (Fig. 2.6B) and originates in compressive drag forces produced by crosslinked filaments of opposite polarity that slide relative to one another due to actin polymerization at their immobilized barbed ends (Fig. 2.3C).

The ring is anchored ~20-fold more strongly than the combined precursor nodes and constricts at a rate set by the balance of ring tension against anchor drag forces

The contractile ring in protoplasts is anchored to the membrane and constricts by sliding parallel to it (Fig. 2.2A,B). To test if the constriction rate is set by ring tension working against anchor drag forces, we compressed protoplasts with coverslips to deform the cells from their spherical shape (Fig. 2.3E) and observed the evolution of ring shape and length during constriction (Fig. 2.3F,H). We simulated constriction in deformed protoplasts by inputting the measured myosin concentrations of Fig. 2.2F into our ring simulation to calculate ring tension, and then using the measured shape of each protoplast (Fig. 2.3H) to calculate the evolution of ring shape and length assuming tension is opposed by anchor drag (Fig. 2.3D and Appendix B). This model predicts that the ring adopts a bent shape, with the central ring portion lagging behind (Fig. 2.3H). The ring shapes we observed in 6 out of 7 protoplasts are in remarkable agreement with these predictions (Fig. 2.3H and Fig. 2.4). This is a demanding test of the model, as the predicted shapes are independent of the ring tension, drag coefficient and model parameters (see Appendix B). We then compared predicted and measured ring length

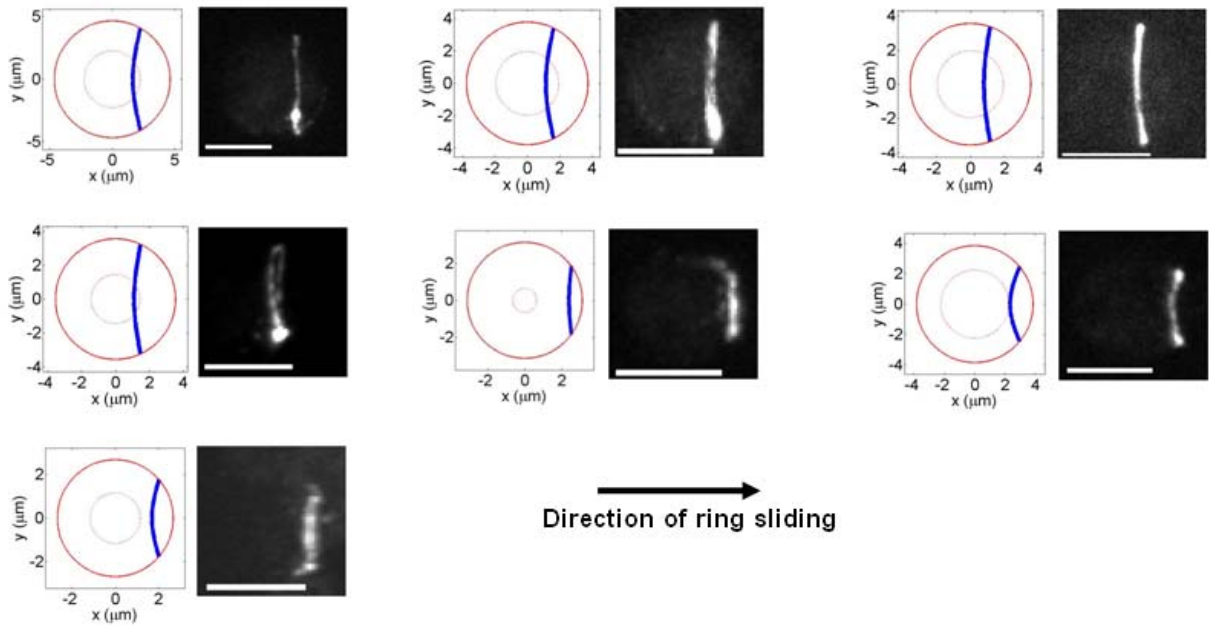

Figure 2.4: Observed and prediction ring shapes in protoplasts.
Observed (right, Rlc1p-3GFP) and predicted (left, blue) shapes of rings constricting in compressed protoplasts viewed from above. Solid red lines indicate the cell boundary, and dotted red lines indicate the boundary of the flat portions of the cells. The simulations reproduce the bent shape of the ring. Parameters, as in Table 2.1. All micrographs from C. Laplante and T.D. Pollard (Yale University). Bars: 5 μm.

constriction histories (L(t), Fig. 2.3F) using the total anchor drag coefficient γ_{ring} as a fitting parameter. The model replicated the curvature of the constriction profiles due to the increasing steepness of the protoplast surface (Fig. 2.3D-F), and yielded the best fit value $\gamma_{ring} = 289 \pm 9$ nN·s/μm, ~20 times the total drag coefficient of all intact cell precursor nodes.[22] Assuming that the anchoring drag decreases with ring length, $\gamma_{ring} \sim L$, significantly worsened the fit, (Fig. 2.3G and Fig. 2.5) suggesting that the number of anchors and the total drag coefficient remain constant.

Alternatively, the ring could be dynamically autonomous and determine its own constriction rate, as proposed for contractile rings in *C. elegans* embryos.[31] However, the tension-anchor drag model fit the experimental data significantly better than two dynamically autonomous models (Fig. 2.3G and Fig. 2.5). In the first, the ring has a constant constriction rate proportional to its initial length as in *C. elegans* embryos.[31] In the second, the constriction rate is

proportional to the myosin concentration but independent of protoplast shape and other external factors.

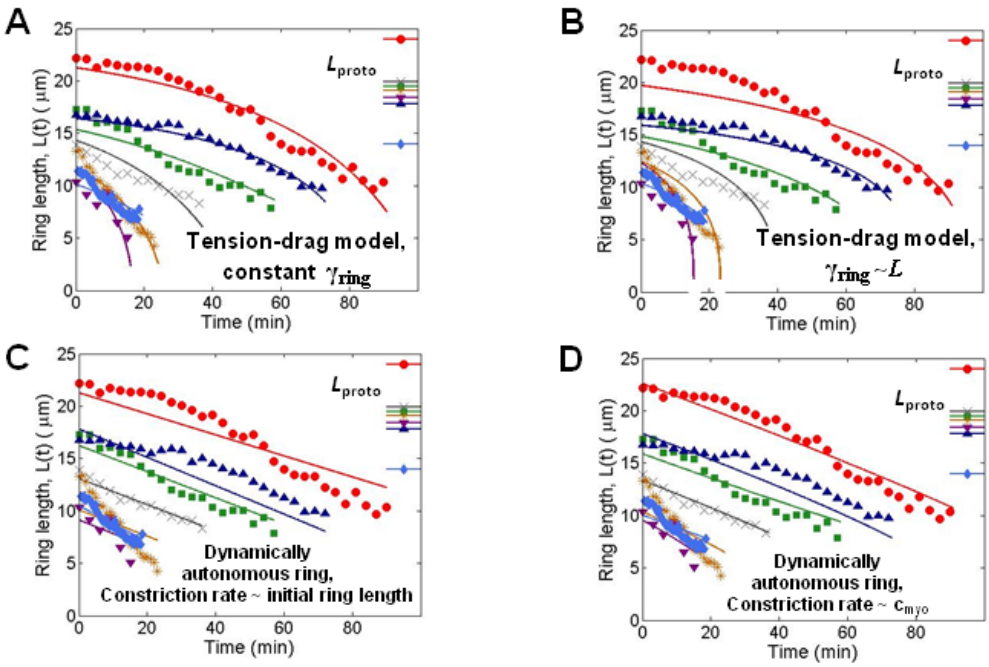

Figure 2.5: Best fit ring constriction profiles from 4 different models.
(A) The tension-drag model with constant drag coefficient matches the experimental measurements best. (B) The tension-drag model with a drag coefficient that decreases with ring length has constriction curves with larger curvature than observed.
(C and D) Dynamically autonomous rings with constant constriction rates proportional to initial ring length, as in Carvalho et al,[31] fail to reproduce the observed curvature in the constriction profiles (C), as do dynamically autonomous rings whose constriction rate is proportional to the myosin concentration (D).
All parameters, from Table 2.1. Ring tension as a function of ring length from Fig. 2.6B.

These results suggest that the ring is not autonomous and that the constriction rate results from ring tension acting on ring-membrane anchors. Further, following assembly the ring anchoring to the cortex strengthens ~20 fold in preparation for constriction and remains approximately constant during constriction.

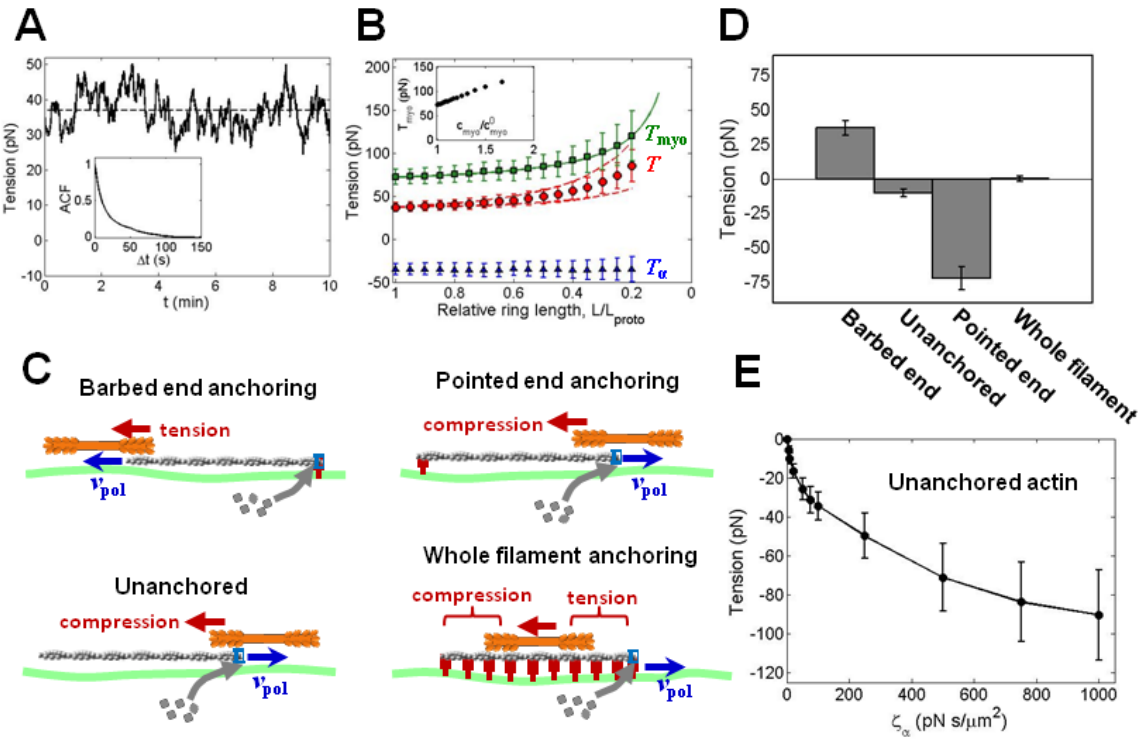

Figure 2.6: Ring tension fluctuates in time, increases with increasing myosin concentration and is maximized for barbed end actin filament anchoring.
(A) Ring tension fluctuations in the simulation reflect continuous renewal of actin organization ($L = L_{proto}$). Dashed line: mean. Inset: tension autocorrelation function exhibits memory time 18.2 s (exponential fit).
(B) Ring tension in simulation has a tensile myosin and a compressive frictional component. Evolution during constriction is plotted. Circles: net tension T. Dashed lines: uncertainty range (SEM) from myosin concentration measurements, Fig. 2.2F. Squares: myosin component T_{myo}. Triangles: α-actinin friction component T_{α}. Solid line: myosin component, analytical prediction (Eq. 2.1). Inset: Myosin component is proportional to myosin concentration.
(C) We tested 4 actin filament anchoring schemes for tension generating capability.
(D) Only barbed end anchoring produces tension.
(E) In rings with unanchored actin the compression is greater for larger α-actinin drag coefficient.
Parameters as in Table 2.1 except where otherwise indicated. Error bars: standard deviation of temporal tension fluctuations.

Barbed end actin anchoring is optimal for ring tension

Our model assumes that actin barbed ends are anchored to the inside of the plasma membrane because candidate anchor Cdc15p binds formin Cdc12p[56] and barbed ends are anchored in precursor nodes.[22] However, as other actin anchoring schemes have not been definitively excluded we tested their ability to generate tension (Fig. 2.6C-E; see Appendix B for details).

Our simulations revealed that tension was greatest when each actin filament is anchored at its barbed end because pointed ends grow toward myosins, correctly oriented for interactions that produce tension (Fig. 2.6C,D). Anchoring pointed ends produces filaments incorrectly oriented relative to myosin and results in highly compressive rings. Rings of actin filaments anchored along their lengths produce equal tension and compression forces, so the net tension is negligible (0.03 pN) (Fig. 2.6C,D). In the absence of actin anchors filaments translated about the ring and unanchored barbed ends tended to grow toward myosins, which then pushed the filaments away, causing ring compression due to crosslinker drag forces (-10.3 pN, Fig. 2.6D,E). This analysis shows that anchoring actin filament barbed ends is the only feasible scheme that produces substantial ring tension.

Tension in a randomly organized ring depends on correlations between actin and myosin

Since experiment suggests the ring has significant disorder, our basic model assumed completely random organization. However, as the available data does not preclude greater organization we simulated other organizations having actomyosin correlations due to bias in the actin nucleation statistics (Fig. 2.7A). When formins nucleated filaments oriented toward the nearest myosin oligomers, a peak developed in the actin-myosin cross correlation function $c_{\mathrm{ma}}(x)$ that measures the myosin density distance x from an anchored actin barbed end in the direction of the pointed end (Fig. 2.7C). Thus, filaments tend to be displaced from and oriented toward keys><key app="EN" db-id="r0x9fe20mxw5dcevwpbxwsacervtp525the tension was greater (43 ± 5.3 pN versus 37 ± 5.4 pN at constriction onset, Fig. 2.7D). When nucleation oriented filaments away from nearby myosin oligomers the correlation showed a trough

(antisarcomeric organizational bias) and the tension was less (29 ± 5.8 pN). We also tested the nodes-like organization, where formins bind in myosin-II regions only, which generated slightly less tension than the pure random case, $T = 33.5$ pN.

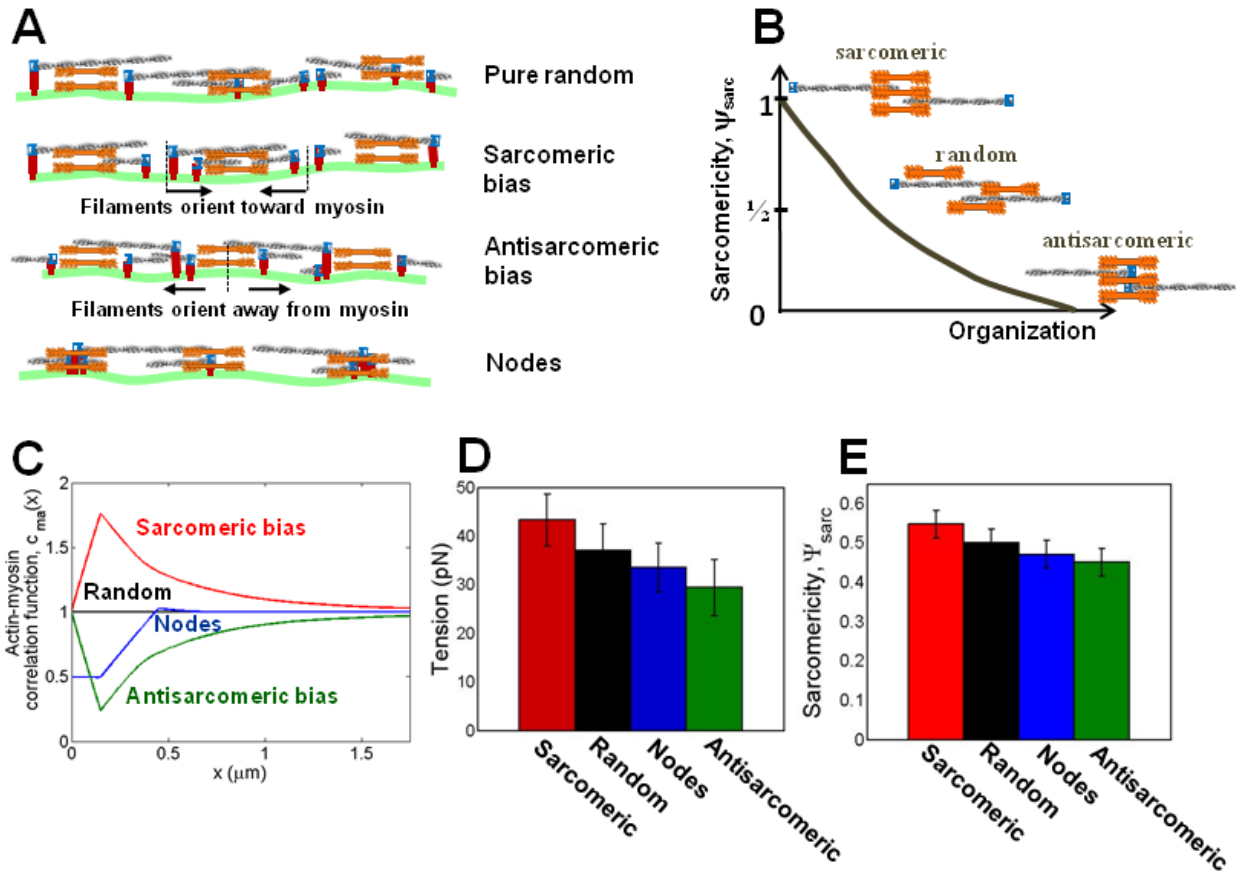

Figure 2.7: Ring tension depends on the spatial organization of actin and myosin
(A) Disordered ring organizations can be classified according to component correlations. For pure randomness, myosin and actin locations and actin polarity are statistically independent. With sarcomeric (antisarcomeric) bias actin filaments tend to orient toward (away from) nearby myosins. In the nodes-like case myosin and actin barbed ends colocalize (actin and myosin in the same node do not interact).
(B) For any random organization, the sarcomericity Ψ_{sarc} quantifies the degree of sarcomeric bias.
(C-E) In accordance with Eq. 1, higher sarcomericity organization produces greater tension. 3 examples of biased formin-mediated actin nucleation statistics were tested (see main text). For each, the actin-myosin correlation function $c_{ma}(x)$ (C), tension (D), and sarcomericity (E) were compared to unbiased (random) nucleation, our basic model.
Parameters, as in Table 2.1. Error bars: standard deviation of temporal tension fluctuations.

Our simulation results of Figs. 4-6 show that ring tension depends on the organizational statistics and myosin concentration c_{myo}. Thus we sought an exact interrelationship obeyed by

our stochastic ring model. In Appendix B we prove that the dominant myosin tension contribution is

$$T_{\mathrm{myo}} = Cf_{\mathrm{myo}} c_{\mathrm{fil}} c_{\mathrm{myo}} \left\langle l^2 \right\rangle \psi_{\mathrm{sarc}} \ , \tag{2.1}$$

where c_{fil} is the actin filament concentration, C is a constant proportional to the ring cross sectional area and $\langle l^2 \rangle$ is the mean square actin filament length whose origin is that longer filaments interact with more myosins. Ring organization enters through the "sarcomericity", ψ_{sarc}, which is directly related to the density correlation function $c_{\mathrm{ma}}(x)$ (Eq. 2.9 in Appendix B) and quantifies the sarcomeric character of a given disordered arrangement (Fig. 2.7B,E). For completely random organization $\psi_{\mathrm{sarc}} = ½$, while muscle ($\psi_{\mathrm{sarc}} \rightarrow 1$) and polarity-sorted organization[75] ($\psi_{\mathrm{sarc}} \rightarrow 0$) represent the extremes of sarcomericity and antisarcomericity, respectively. The specific nucleation schemes above generate intermediate sarcomericities (Fig. 2.7E) that closely correlate with tension and obey Eq. 2.1. Thus, ring tension depends quantitatively on actomyosin statistics through the sarcomericity.

Ring actin turns over ~3-fold faster than formin

The turnover time of formin Cdc12p in the ring, $t_{1/2}$ = 30 s (Fig. 2.8A), was measured using FRAP.[71] This measurement directly set the formin off rate constant in our ring simulation (Table 2.1). However, direct measurement of actin turnover has not been possible as labeled actin does not incorporate into the fission yeast ring.[20] Thus, we mimicked an actin FRAP assay in our simulation by identifying at some instant all the actin subunits in the ring (the 'bleached' population) and tracking the arrival of new ('unbleached') units. Using the model parameters from Table 2.1, from the simulated recovery curve we extracted the actin turnover time, $t_{1/2}$ = 11 s (Fig. 2.8A). Thus, we predict that actin turns over ~3-fold faster than formin because formin

can leave the ring only by dissociation from the membrane, whereas actin is removed both by formin dissociation and by cofilin-mediated filament severing (Fig. 2.8C).

Experiments in formin mutant cells are consistent with the model's turnover mechanisms

We tested whether our model is consistent with previous measurements in cells expressing formin mutants with deletions of both profilin binding domains (ΔPBD) from the FH1 domain. In these cells, compared to wild type the formin off rate measured by FRAP was smaller (k_{off}^{for} = 0.009 s^{-1} versus 0.023 s^{-1}, Fig. 2.8A) and the mean time for rings to completely disintegrate after high doses of LatA was greater (138 s versus 55 s).[71] We simulated the ring disintegration assay with mutant formin by using the experimentally measured k_{off}^{for} value, running to steady state and then setting v_{pol} = 0 and recording the time for 90% of the actin to disappear. To reproduce the observed disintegration time we used the actin polymerization rate of the mutant formin as a fitting parameter and found the best fit value v_{pol} = 12 nm/s (Fig. 2.8B). This is much less than our model's best fit value in wild type cells, 70 nm/s (Table 2.1), consistent with bulk assays showing that the mutant formin had dramatically reduced polymerization activity.[71] Thus, the assumed turnover mechanisms in our simulation (Fig. 2.3B) are able to capture the behavior of contractile rings with perturbed actin and formin turnover.

Ring tension and constriction rates depend on actin polymerization rates

Reducing actin polymerization rates in intact fission yeast cells with a low concentration of LatA or expression of a formin mutant slowed ring constriction by ~30% compared to wild-

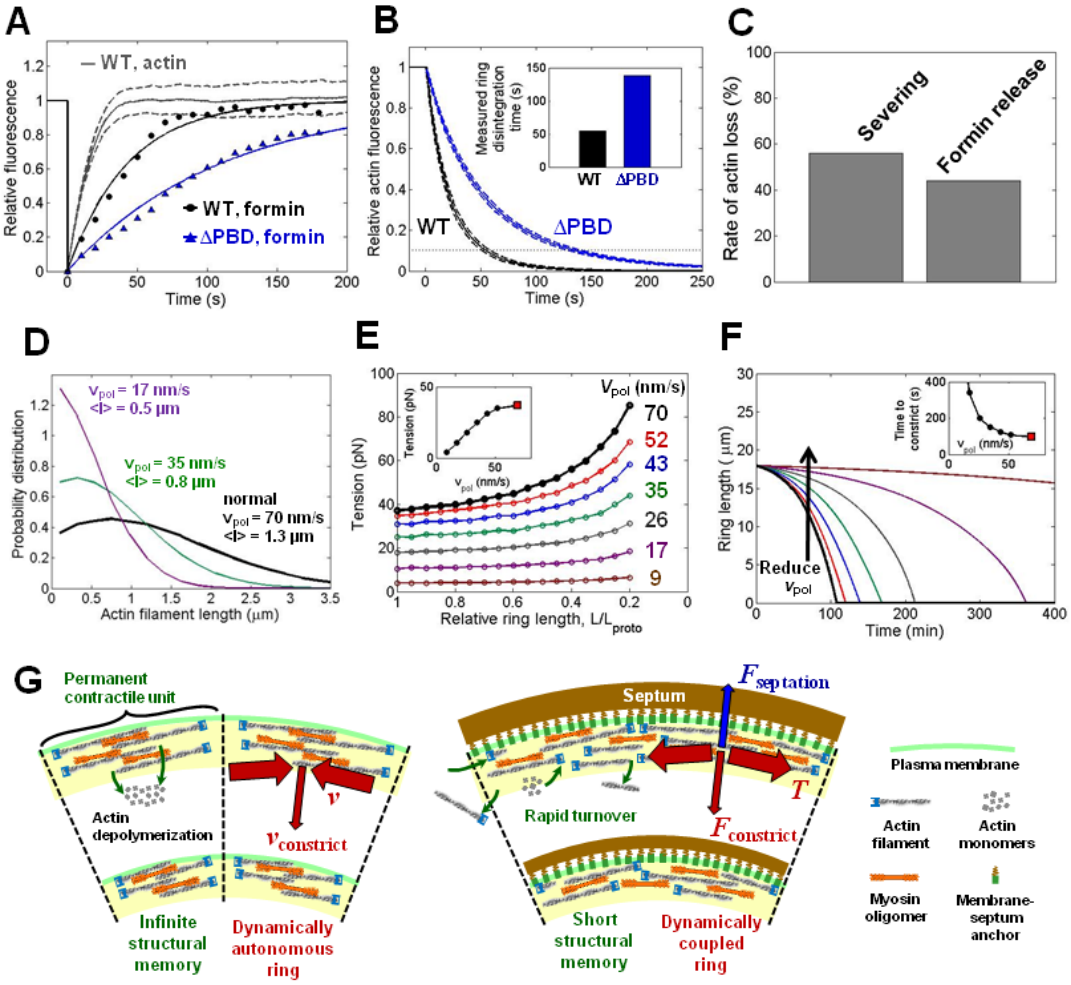

Figure 2.8: Actin and formin turnover.

(A) In simulated FRAP assays, actin recovered in $t_{1/2}$ = 11 s (gray solid line; dashed lines, standard deviations for 100 simulated rings). In experiments, formin recovered in $t_{1/2}$ = 30 s in wild-type yeast, circles, and $t_{1/2}$ = 66 s in ΔPBD formin mutants, triangles [71]. Solid lines: exponential fits for dissociation constant, $k_{\text{off}}^{\text{for}}$.

(B) Simulated contractile ring disintegration after treatment with a high concentration of LatA. Actin polymerization rate was chosen to match experiment (inset, Yonetani et al., 2008) for wild-type (v_{pol} = 70 nm/s) and ΔPBD mutant (v_{pol} = 12 nm/s) using 90% disintegration criterion (dotted line). Dashed lines: standard deviation for 100 simulated rings.

(C) Contributions to actin removal from the ring via cofilin-mediated severing and formin anchor release, simulations.

(D) Actin filament length distributions from simulations. Slower polymerization generates shorter filaments.

(E and F). Slower polymerization causes lower tension (E) and slower constriction (F), simulations. Insets: ring tension at constriction onset (E) and constriction time (time to constrict from $0.95L_{\text{proto}}$ to $0.2L_{\text{proto}}$) (F). Red squares: standard v_{pol} value, Table 2.1.

(G) Comparison of the mechanism of constriction proposed for *C. elegans* (left) [31] and our proposal for fission yeast (right). (Left) Permanent contractile units endow the ring with structural memory. The constriction rate is set by the intrinsic contraction velocity of sarcomere-like contractile units. (Right) Fission yeast rings have rapid turnover and a short structural memory. The constriction rate is set by a balance between ring tension and resistance forces from the septum (ring-membrane anchors in protoplasts).

Parameters as in Table 2.1, except where otherwise indicated.

type cells.[24] In agreement with these experiments, reducing the actin polymerization rate in simulations lowered both ring tension and constriction rates (Fig. 2.8E,F). The tension is lower in the simulations because slow polymerization generates shorter filaments (Fig. 2.8D) that couple to fewer myosins (Eq. 2.1), and reduced tension drives slower constriction. Thus, our model captures a mechanistic link between actin polymerization, ring tension and ring constriction kinetics.

V. Discussion

The fission yeast protoplast as a model system to study cytokinesis

While *S. pombe* is attractive for mathematical modeling of cytokinesis, constriction rates cannot be predicted as ring constriction is closely coupled to the poorly understood septation process. Similar issues arise in animal cells, where constriction couples to cortical flow,[76] membrane remodeling,[77] and cytoplasm displacement by the ingressing furrow. To overcome this obstacle, we studied fission yeast protoplasts in which rings constricted by sliding on the membrane without septation (Fig. 2.2B). This simplification allowed us to quantitatively compare predictions of our simulation to experimental observations (Fig. 2.3F,H), enabling us to interrogate ring constriction mechanisms directly in a way not possible at present with normal yeast.

While only a small fraction of mitotic protoplasts successfully assembled rings (<1% observed, Fig. 2.1G,H), node anchoring and myosin activity appeared little affected by the loss of cell wall as node drag coefficients and velocities were similar to those in intact cells. Compared to normal yeast, protoplast rings were longer (~19 μm versus ~10 μm) but

constriction rates and myosin concentration profiles were similar (Fig. 2.2D-F). Thus, our results suggest that contractile rings in protoplasts are largely normal.

How does tension emerge from the disordered, non-sarcomeric ring organization?

We observed ring shapes, ring constriction rates and membrane deformation that demonstrated the fission yeast contractile ring is tensile (Figs. 2.2 and 2.3). Generally, a contractile structure can produce tension only if components are crosslinked or are immobilized by anchoring. Our ring simulations showed that the actin filament crosslinker α-actinin provides only short-lived connections that generate compressive frictional forces (Figs. 2.3C and 2.6B), consistent with ring constriction in mammalian cells being retarded by over expression of α-actinin and accelerated by knocking down α-actinin expression.[78] Tension production required that actin filaments be anchored to the membrane at their barbed ends (Fig 2.6D). Indeed, actin barbed ends are anchored in a variety of tension-producing structures including striated muscles,[79] focal adhesions,[43] and contractile rings of newt eggs.[80]

The ring generates tension despite its apparently disordered organization, remote from the ordered sarcomeric arrangement of striated muscle. Our analysis showed that the tension depends on the sarcomericity ψ_{sarc} (Eq. 2.1 and Fig. 2.7), a statistical property that quantifies the degree to which the positions and polarities of myosin-II and actin have sarcomeric tension-producing bias. Its value for the *S. pombe* ring is unknown, but may be measurable by electron or super-resolution fluorescence microscopy. We found that completely random organization ($\psi_{sarc} = 0.5$) produces approximately one half the tension of sarcomeres ($\psi_{sarc} = 1$) but the tension would be greater if sarcomeric bias were present ($\psi_{sarc} > 0.5$). Given that contractile rings form from nodes containing both myosin-II and formin Cdc12 that may persist after assembly of rings,

we simulated a node-like organization that produced about the same tension (ψ_{sarc} = 0.47) as the pure random case (Fig. 7).

Ring tension in fission yeast is much smaller than in animal cells

To our knowledge the only measurements of contractile ring tension are 10-15 nN in fertilized sand dollar and sea urchin eggs.[81] Our model predicts much smaller tensions of ~40-80 pN in the fission yeast contractile ring (Fig. 2.6B), as expected given the much smaller cross sectional area of the ring. However, the yeast ring is weak even allowing for size differences: the stress is 1.3-2.6 nN/μm^2 (assuming 0.2 μm diameter, see Table 2.1), compared with ~25 nN/μm^2 in animal cells,[81] 5 nN/μm^2 on focal adhesions,[82] and 250 nN/μm^2 in striated muscle.[83] This may reflect differences in actomyosin packing densities or organization (Eq. 2.1). Small tensions of 8 pN were also predicted to be sufficient to drive cell division in *E. coli*.[84]

Ring anchoring transmits and stabilizes ring tension

Ring-membrane anchors presumably transduce the ring tension into centripetal force that could drive constriction. Indeed, defectively anchored rings in *Drosophila* cells detached centripetally from the cortex.[52] We found that the ring-membrane drag coefficient was ~20-fold larger than the total of all precursor nodes during ring assembly,[22] which correlates with the 10-fold increase of candidate anchor Cdc15p in the ring as the ring matures.[20] However, if our prediction that anchor strength is approximately constant during constriction (Fig. 2.3F,G) is correct, Cdc15p is not the only anchor because the amount of Cdc15p decreases during constriction.[20]

The reinforcement of ring anchoring before constriction may both secure the ring to the membrane and stabilizing ring organization and tension. Weaker anchoring may be advantageous during ring assembly when myosin forces pull nodes into a tight ring with velocities ~30 nm/s.[22] However, were such weak anchoring to persist into constriction, actin and myosin would slide ~0.9 μm during the ~30 s actin filament lifetime. This displacement is similar to the mean filament length and would significantly dissipate ring organization and tension. Thus, anchor reinforcement justifies our model assumption that actin and myosin are in effect immobilized in the membrane.

Actin and formin turnover

While actin FRAP assays of the ring have not been possible, should this be achieved in the future it would be possible to test our prediction that actin turns over ~3-fold faster than formin ($t_{1/2}$ = 11 s, Fig. 2.8A) because in addition to filaments leaving the ring when their formin anchors dissociate, actin is also removed by cofilin-mediated severing (Fig. 2.8C). Our simulations also revealed that the time for complete ring disintegration after inhibiting polymerization with LatA, which has been used as an indirect measure of actin filament turnover,[24] overestimates the actin turnover time by a factor ~5 (1 min versus 11 s).

We used our model to fit for the values of key turnover parameters which have not been measured in the ring (Table 2.1). The formin-mediated actin polymerization rate was 70 nm/s, ~3 times less than the rate of filament extension from the precursor nodes,[22] while the actin filament severing rate per unit filament length was 1.8 $min^{-1}\mu m^{-1}$, ~6 fold faster than the rate at which the optimal concentration of cofilin Adf1p severs muscle actin filaments in vitro.[69] Other reactions in

fission yeast were also predicted to be underestimated by in vitro assays using purified proteins.[85]

Mechanism of constriction

Our results describe the fission yeast contractile ring as a dynamically coupled tension-producing machine regulated by actin turnover that determines the organization (Fig. 8G). Actin turnover kinetics set the ring tension since tension depends on ring components and their organization: the rates of filamentous actin nucleation, polymerization and depolymerization and the bias in these processes set the density, length distribution and sarcomeric correlations on which tension depends (Eq. 2.1 and Fig. 7). Thus, constriction can be regulated by actin turnover since tension drives constriction. For example, constriction rates would be lowered were the formin-mediated actin polymerization rate reduced, since actin filaments would then be shorter and the tension lowered as shorter filaments couple to fewer myosins (Eq. 2.1). This prediction is in qualitative agreement with published data.[24]

An essential feature of the ring mechanism is that turnover is much faster than constriction. As the actin organization is renewed every ~30 s, the tension is constantly refreshed on a similar timescale as is manifest in the simulated tension fluctuations with memory times of ~18 s (Fig. 6A). This could prevent dissipation of tension that would otherwise occur due to motion of anchored ring components which are known to have finite mobility in the membrane given that rings can slide. Rapid turnover may also endow rings with robustness in the face of perturbations, since structural defects could be healed in <1 min. On the long timescales of constriction (~30 min, Fig 3F), in effect the ring is being continuously remodeled. Thus rapid turnover provides the mechanism for ring remodeling: as the ring shortens it quasi-statically

presents fewer and fewer binding sites for formins that nucleate actin. Hence, the number of filaments decreases in proportion to ring length but local organizational statistics and actin density are constant, consistent with the reported constant actin density and decrease in formin numbers during constriction.[20]

This picture of the contractile ring contrasts with that proposed for *C. elegans*.[31] To explain the proportionality between constriction rate and initial ring length during early embryo divisions, it was proposed that the ring never loses memory of its initial structure and is dynamically autonomous, i.e. constriction rates depend only on intrinsic properties of the ring. We find the *S. pombe* ring has a short structural memory time and the constriction dynamics are not autonomous: by studying deformable protoplasts we could show that the ring produces tension, but its constriction rate depends on conditions external to the ring. Experimentally, ring shapes and constriction rates depended on the shape of the protoplast surfaces on which they moved. On flattened protoplasts, constricting rings adopted curved shapes matching those predicted by a model assuming tension works against ring-membrane drag forces (Fig. 3H). This was a stringent test, as the predicted shapes are independent of the values of the tension, drag forces and model parameters. Thus, our analysis suggests the primary function of the ring is to generate tension and the constriction rate in intact yeast is set by the response of the septation system to the ring's tension output (Fig. 8G).

Appendix A: Experimental Procedures

Strains and protoplast preparation. Cells expressed fusion protein Rlc1p-3GFP under the control of their native promoters and from their endogenous locus. *S. pombe* cells were grown to OD_{595} of 0.2 and 8-10 ml of cells were harvested by centrifugation in tabletop

Beckman for 5 minutes at 2000 rpm. The cell pellet was resuspended in the yeast Lytic/Lysis enzyme cocktail (2.5 mg/mL Lytic enzyme (MP Biometicals), 2.5 mg/mL Lysis enzyme (Sigma-Aldrich) dissolved in E-buffer (50 mM Sodium Citrate, 100mM phosphate buffer pH 6.0) with 0.6 M sorbitol) and incubated for 1 hour at 30ºC. The protoplasts were washed twice with E buffer + 0.6 M sorbitol. The pellet was resuspended in 50 µl mounting medium (50% EMM5S in E buffer with 1.2 M sorbitol, 100 µl NPG 10X and 2.5 mg/mL of each Lytic and Lysing enzyme). The protoplasts in suspension were mounted onto a glass slide, covered with a coverslip, sealed with VALAP, and immediately imaged.

Microscopy. Cells were imaged by fluorescence and DIC microscopy using either a spinning disk confocal microscope or a conventional wide field microscope.

Node measurements. A single focal plane of protoplasts expressing Rlc1-3GFP was imaged for 100-550 seconds with a 1 s time interval. Node MSDs were measured by tracking the position of the maximum intensity pixel in each node and following the procedure described previously.[22] Velocities of nodes undergoing stop-go motion were calculated by dividing the node displacement in a burst of motion by the duration of the motion. The brightest pixel of the node was tracked.

Measurement of ring length and cell circumference. The Reslice function in ImageJ software (http://rsb.info.nih.gov/ij/) was used to view the ring face-on, and then ring length L was measured by tracing the ring in a maximum intensity projection. The protoplast circumference L_{proto} was measured by tracing the perimeter of the cell in a maximum intensity projection after viewing it from the same angle as the ring.

Quantitative fluorescent microscopy. Stacks of Rlc1p-3GFP fluorescent images were obtained spanning the entire cell spaced 0.336 µm apart, and then combined using a sum

projection in ImageJ. Ring intensity was measured by measuring the fluorescence intensity inside a polygon drawn around the ring, and then subtracting background measured in a nearby region within the cell. A photobleaching correction curve was obtained by measuring the fluorescence intensity of the entire cell.

Appendix B: Detailed Description of the Contractile Ring Simulation

Ring geometry

The simulated contractile ring is a torus with length L and cross sectional diameter d (Fig. 2.3A and Fig. 2.9). The x-axis follows the ring in the counterclockwise direction. Formin-capped actin filaments reside in a hexagonal lattice of $N_{\text{tube}} = 31 \approx d^2/ d_\alpha^2$ tubes aligned with the x-axis, where d_α is the lateral spacing between tubes (Fig. 2.9). Each actin filament remains in one tube for its entire lifetime. Anchored and immobilized myosin clusters have random positions in a complementary lattice of myosin tubes, each of which is surrounded by three actin tubes (Fig. 2.9). Each cluster comprises two myosin oligomers of length w_{myo} in adjacent myosin tubes.

Actin and formin turnover

(i) *Nucleation*. New formin proteins enter the ring in randomly chosen actin tubes. The number entering during a time step Δt follows a Poisson distribution with mean $r_{\text{nuc}}L\Delta t$, where r_{nuc} is the nucleation rate per ring length. Each new formin immediately nucleates an actin filament which has barbed end to the $-x$ (polarity $p = +1$) or $+x$ ($p = -1$) direction. We tested 4 types of actin nucleation statistics: completely random (random x and p), sarcomeric (random x,

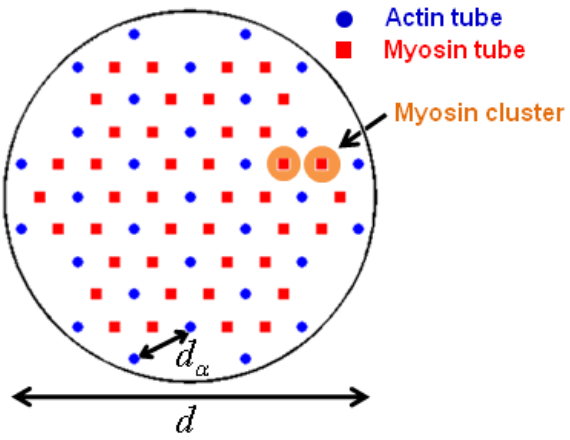

Figure 2.9: Cross section of the simulated fission yeast contractile ring.
Actin filaments in the simulated ring occupy a hexagonal lattice of actin tubes (blue circles), with neighboring tubes separated by distance d_α. Myosin clusters composed of two adjacent myosin-II oligomers (example shown in orange) reside in a complementary lattice of myosin tubes (red squares), each of which borders three actin tubes. Myosin oligomers only interact with overlapping actin filaments in bordering actin tubes. Myosin clusters are assumed to contain n_{myo} = 40 myosin-II heavy chains, the number measured in nodes in intact cells (Table 2.1). Each myosin cluster borders four actin filament tubes; two of these actin tubes border both myosin oligomers, and the other two border only one of the oligomers. Therefore a force per oligomer of f_{myo} = 2.75 pN results in an average force of 4 pN on a neighboring actin filament, as in our measurements of protoplast nodes (Table 2.1).

oriented toward nearest myosin), antisarcomeric (random x, oriented away from nearest myosin), and nodes (nucleation only in myosin regions, random p). (ii) *Growth*. Actin filaments grow at their barbed ends length $v_{pol}\Delta t$ each time step, where v_{pol} is the polymerization rate. (iii) *Severing*.Each actin filament is severed by cofilin with probability $r_{sev}l\Delta t$ each time step, where l is the filament length and r_{sev} the severing rate. Severing is equally likely everywhere along the filaments, and the resulting free portion of a severed filament is deleted from the simulation. (iv) *Removal*. Each formin unbinds from the ring with probability $k_{off}^{for}\Delta t$ in each time step, where k_{off}^{for} is the formin off rate. Both the dissociated formin and its associated actin filament are deleted from the simulation.

Balancing formin binding and unbinding rates gives a steady state formin concentration of $4r_{nuc}/(\pi d^2 k_{off}^{for})$. Comparing to the measured formin concentration allowed us to set the value of r_{nuc} because d and k_{off}^{for} have been measured (see Table 2.1). The values of r_{sev} and v_+ were

determined simultaneously by fitting to data from two other experiments, as described in Table 2.1.

Forces, velocities, and tension

Forces. (i) Myosin oligomers pull on overlapping actin filaments in neighboring tubes with force $p_i f_{myo} w_{ik}/w_{myo}$, where w_{ik} is the length of overlap between actin i and myosin k. (ii) Dynamic actin crosslinker α-actinin Ain1p offers viscous resistance to relative motion of overlapping filaments in neighboring actin tubes with force $-\zeta_\alpha \Delta l_{ij} \Delta v_{ij}$, where ζ_α is the drag coefficient per length of overlap, Δl_{ij} is the length of the overlap between neighboring actin filaments i and j, and Δv_{ij} is their relative velocity.

Actin filament velocities. We tested 4 types of actin filament anchoring. When barbed ends are anchored, polymerization pushes the pointed end away from the immobilized anchor, resulting in actin filament velocity $v_i = p_i v_{pol}$. When pointed ends are anchored, or when filaments are anchored along their entire length, new actin subunits elongate the filament at the barbed end without causing filament motion, $v_i = 0$, and there are no dynamic crosslinking forces. When actin filaments are unanchored, actin filament velocities are determined by requiring the sum of forces on each filament to vanish:

$$\sum_k f_{myo}(w_{ik}/w_{myo})\left(p_i - v_i/v_{myo}^0\right) - \zeta_\alpha \sum_j \Delta l_{ij} \Delta v_{ij} = 0 \ . \qquad (2.2)$$

The first term is the total myosin force on actin filament i, where $v_{myo}^0 = 0.4$ μm/s is the unloaded working velocity of myosin.[66] For simplicity we assumed a linear myosin force-velocity relation. The second term is the total dynamic crosslinking force on filament i. At each simulation timestep, Eq. 2.2 is solved for all filament velocities allowing update of filament positions.

Ring tension. The tension averaged over the ring length is given by

$$T = \sum_{i=1}^{N} T_i^{\mathrm{fil}} l_i / L\,, \tag{2.3}$$

where T_i^{fil} is the tension of actin filament i averaged over its length, and the sum is over all N actin filaments. With anchored actin filaments the tensions can be expressed as sums of independent contributions from myosin forces and crosslinking forces: $T = T_{\mathrm{myo}} + T_{\alpha}$, and $\mathrm{T_i^{fil}} = T_i^{\mathrm{myo}} + T_i^{\alpha}$. At each simulation timestep, T_i^{fil} was calculated for each filament from viscous and myosin forces and then Eq. 2.3 was used to calculate the ring tension. For simplicity we only calculated the tension in the actin filaments and neglected the tension within the myosin oligomers themselves, which is valid if the myosin oligomer is more compliant than the membrane to which it is anchored. Even if this condition is not satisfied, this is a small correction to the tension because while myosin oligomers and actin filaments are equally abundant (150 of each per 10 μm of ring length, see Table 2.1), the myosin clusters are much shorter (0.3 μm versus 1.3 μm average actin filament length, see Table 2.1) and therefore contribute less to the tension (Eq. 2.3).

Each simulation was performed at fixed L because constriction lasts much longer than actin and formin turnover. Reported tensions are averaged over many simulations with different random myosin positions, and each simulation was run for >250 times the formin turnover time.

Analytical calculation of the myosin-generated tension

Here we derive Eq. 2.1, an expression for T_{myo} (the ring tension contributed by myosin forces when actin filaments are anchored at their barbed ends). The tension generated by myosins in one actin filament averaged over its length is

$$T_i^{\text{myo}} = \left(f_{\text{myo}} / l_i\right)\int_0^{l_i} x\rho_{\text{myo}}(x \mid 0)dx \tag{2.4}$$

where $\rho_{\text{myo}}(x|0)$ is the number density of myosin oligomers in neighboring myosin tubes distance x from the filament's barbed end in the direction of the pointed end, assuming the barbed end is at $x = 0$. The integral is therefore taken from the filament's barbed end to its pointed end. The myosin density contributed by each oligomer is equal to $1/w_{\text{myo}}$ within the width of the oligomer and zero elsewhere. Using Eq. 2.3 to calculate the total myosin tension and converting the sum to an average over all actin filaments yields

$$T_{\text{myo}} = f_{\text{myo}} \frac{N}{L}\left\langle \int_0^l x\rho_{\text{myo}}(x \mid 0)dx \right\rangle, \tag{2.5}$$

where N is the number of actin filaments (formins). Next we normalize the myosin density by its mean value $\rho_{\text{myo}} = (N_{\text{myo}}/N_{\text{tube}})/L$, where N_{myo} is the number of myosin oligomers in the ring:

$$T_{\text{myo}} = \frac{f_{\text{myo}}}{N_{\text{tube}}} \frac{N_{\text{myo}}}{L} \frac{N}{L}\left\langle \int_0^l x \frac{\rho_{\text{myo}}(x \mid 0)}{\rho_{\text{myo}}} dx \right\rangle . \tag{2.6}$$

Finally, we define the myosin heavy chain concentration $c_{\text{myo}} = n_{\text{myo}}N_{\text{myo}}/(LA)$ and the actin filament concentration $N/(LA)$, where A is the cross sectional area and n_{myo} the number of myosin heavy chains per oligomer. We now obtain Eq. 2.1,

$$T_{\text{myo}} = Cf_{\text{myo}}c_{\text{fil}}c_{\text{myo}}\left\langle l^2 \right\rangle \psi_{\text{sarc}} , \tag{2.7}$$

where the constant C is given by

$$C = \frac{AA_{\text{tube}}}{n_{\text{myo}}} . \tag{2.8}$$

The geometric factor $A_{\text{tube}} = A/N_{\text{tube}}$ is the cross-sectional area per actin tube, which is on the order of d_α^2. In our simulation's hexagonal lattice (Fig. 2.9), $A_{\text{tube}} \approx 0.78\, d_\alpha^2$. The sarcomericity ψ_{sarc} is

$$\psi_{\text{sarc}} = \frac{1}{\langle l^2 \rangle} \left\langle \int_0^l x c_{\text{ma}}(x) \mathrm{d}x \right\rangle , \tag{2.9}$$

where the integral is ensemble averaged over the actin filament length distribution. The actomyosin correlation function $c_{\text{ma}}(x)$ is the average normalized myosin density position x away from a barbed end, in the direction of the pointed end, written as

$$c_{\text{ma}}(x) = \frac{\left\langle \rho_{\text{myo}}(x) \rho_{\text{fil}}(0) \right\rangle}{\rho_{\text{myo}} \rho_{\text{fil}}} , \tag{2.10}$$

where ρ_{fil} is the linear actin barbed end density in one actin tube. Here, we used the fact that $\langle \rho_{\text{myo}}(x|0) \rangle \rho_{\text{fil}} = \langle \rho_{\text{myo}}(x) \rho_{\text{fil}}(0) \rangle$. For a completely random organization, Eq. 2.10 gives $c_{\text{ma}}(x) = 1$ and Eq. 2.9 gives $\psi_{\text{sarc}} = ½$.

This approach can be extended to pointed end and whole filament anchoring. Consider actin filaments anchored to the membrane at fraction α of the filament length away from the barbed end. Thus for barbed end anchoring $\alpha = 0$, and for pointed end anchoring $\alpha = 1$. Forces between the anchor and the barbed end cause compression, and myosin forces between the anchor and the pointed end create tension. The ring tension is still given by Eq. 2.7, but with a modified sarcomericity,

$$\psi_{\text{sarc}} = \frac{1}{\langle l^2 \rangle} \left\langle \int_{-\alpha l}^{(1-\alpha) l} x c_{\text{ma}}(x) \mathrm{d}x \right\rangle . \tag{2.11}$$

Therefore, with random actomyosin organization ($c_{\text{ma}} = 1$), the sarcomericity is $\psi_{\text{sarc}} = \alpha - ½$. Pointed end anchoring ($\psi_{\text{sarc}} = -1/2$) creates compression in the ring with the same magnitude as the tension generated by myosin with barbed end anchoring. It is simple to show that whole-filament anchoring is equivalent to anchoring at the center of the filament ($\alpha = ½$) so that $\psi_{\text{sarc}} = 0$ and $T_{\text{myo}} = 0$.

Application of the simulation to constriction in protoplasts

The ring simulation outputs the ring tension as a function of ring length, $T(L)$. We used this to calculate the constriction profiles of protoplast rings sliding along the membrane. The sliding velocity is determined by balancing two forces: (i) the component of ring tension T tangential to the membrane, and (ii) drag forces opposing the sliding arising from ring-membrane anchors (Fig. 2.3C). For a spherical protoplast, it is simple to show that the ring length obeys

$$\gamma_{\text{ring}} \frac{\mathrm{d}L}{\mathrm{d}t} = -4\pi^2 T(L)(1 - L^2 / L_{\text{proto}}^2) \ , \tag{2.12}$$

where L_{proto} is the protoplast circumference.

We observed ring constriction in compressed protoplasts (Fig. 2.3E,H) whose shape is described by the following function, where z is the direction normal to the substrate:

$$\begin{aligned} z(x,y) &= \pm h && 0 < x^2 + y^2 < R^2 \\ z(x,y) &= \pm\left[h^2 - \left(\sqrt{x^2 + y^2} - R\right)^2 \right]^{1/2} && R^2 < x^2 + y^2 < (R+h)^2 \end{aligned} \ , \tag{2.13}$$

where R is the radius of the flat circles capping the protoplast and h is half the total protoplast height. The substrate is at $z = -h$. The ring is described by the vector $\mathbf{r}(s) = \langle x(s), y(s), z(s) \rangle$, parameterized by the initial arc length along the ring, s. The force balance per unit length of ring is

$$\gamma_{\text{ring}} \frac{\mathrm{d}\mathbf{r}}{\mathrm{d}t} = TL\kappa\left[\mathbf{n} - \mathbf{N}(\mathbf{N} \cdot \mathbf{n})\right] \ , \tag{2.14}$$

where κ is the local ring curvature, $\mathbf{n}$ is the unit vector normal to the ring, and $\mathbf{N}$ is the unit inward normal vector to the protoplast surface (Eq. 2.13). Note that according to Eq. 2.14, for a given initial condition the values of T and γ_{ring} only scale the rate of the evolution of the ring and do not affect the shape of the ring.

Procedure for obtaining simulated ring constriction curves. For each of the 7 compressed protoplasts that we observed with constricting rings, we measured the protoplast shape parameters R and h. The maximum possible ring length is then $L_{proto} = 4R + 2\pi h$. Then for each protoplast, we evolved the shape of the contractile ring by numerically solving Eq. 2.14 from an initial condition in which the ring was confined to the plane $x = 0.1$ μm. After a brief transient, ring shapes were independent of the initial condition and the values of γ_{ring} and T only affected the rate of ring sliding. Ring tensions $T(L)$ were taken directly from the corresponding measurement of relative myosin concentration (Fig. 2.2F). Ring lengths at each time were calculated from the ring shape to give $L(t)$. One value of γ_{ring} was used to fit all 7 measured protoplast constriction curves simultaneously.

Chapter 3

Kinetics of Stress Fibers

In this chapter, we switch from the contractile ring to another prominent actomyosin cytoskeletal structure, the stress fiber. We present a model of the stress fiber in which actin turnover is coupled to mechanical stresses, motivated by an experiment that showed that the stress fiber sarcomere relaxation time is of the same order as the actin turnover time. The model predicts that the rate of sarcomere length changes is limited by the turnover rate, and model results are in agreement with the experiment. This work was published in 2008.[86] The model is extended and its predictions directly tested against a larger dataset in Chapter 5.

I. Introduction

The cytoskeleton is a highly dynamic network of semi-flexible protein filaments and other components. Two prominent elements are myosin-II motor proteins and actin filaments having the important property of polarity with two distinct ends, the 'barbed' and the 'pointed' end. Since the motor domains of myosins bind to actin filaments and tend to move towards the filament barbed ends, myosins can exert contractile force when appropriately constrained. Actin structures often exhibit continuous turnover in which actin subunits exchange with cytosolic actin. Many of the cytoskeleton's dynamical functions hinge on these two closely related properties: contractility and renewal. Cytoskeletal structures assembled from actin, myosin and other components exert contractile forces, often closely coordinated with filament assembly and disassembly. Contractile structures enable the exertion and sensing of forces, cytoskeleton remodeling, regulation of local cellular rigidity and shape and many other functions.[87]

In this chapter, we aim to elucidate mechanisms underlying the behavior of a basic cytoskeletal contractile structure: the stress fiber. We seek to understand how actin filament turnover and contractile forces may work together to generate the measured characteristics. We are particularly motivated by a recent experimental study of stress fibers where surprisingly nonuniform contractility was observed after stimulation, some fiber regions being contractile and others expansive.[41]

Stress fibers are tensile actomyosin bundles anchored at each end to the extracellular matrix via transmembrane protein complexes called focal adhesions. They are both force producers and force sensors[44,88] and can endow the cell with anisotropic dynamically adjustable rigidity as required.[89] *In vivo*, stress fibers arise in vascular endothelial cells under shear stress[33,34] where they mediate adhesion to the underlying extracellular matrix (the basal lamina) and in contractile cells (myofibroblasts) involved in wound healing[4] which exert forces to close the wound[5]. Beyond its intrinsic importance, the stress fiber is possibly the simplest and most accessible cellular actomyosin contractile machine and establishing its organization and mechanisms may illuminate general cortical contractility and presumably more complex structures such as the contractile ring in cytokinesis.[1,90]

Along the stress fiber axis regions containing the actin cross-linking protein α-actinin alternate with regions containing myosin-II[40] and the polarity of the actin is periodic.[39] In addition, a nonmuscle form of the giant spring-like protein titin, c-titin, localizes to stress fibers in a periodic pattern[91] These observations are consistent with a sarcomeric structure similar to that of muscle fibrils,[92] albeit one that may be somewhat less ordered. This is shown schematically in Fig. 3.1: the myosin-containing regions (analogous to the A-bands in muscle) lie in the middle of each sarcomere which is symmetric about its center plane; two oppositely-

oriented actin filaments of equal length lie on either side of the center plane, their pointed ends in the myosin region and their barbed ends near the sarcomere boundaries in the α-actinin-containing regions (analogous to the Z-line regions in muscle). One sarcomere consists of many such filament pairs plus myosin arranged in parallel into an approximately cylindrical bundle, while the stress fiber is built from many such sarcomeres connected in series.

The contractile force in stress fibers is produced by nonmuscle myosin-II molecular motors, likely in the form of bipolar minifilaments, aggregates of 10–30 myosin molecules approximately 0.3 μm in length.[11,12,93] Similar to thick filaments in striated muscle, minifilaments are symmetric with myosin motor domains located at both ends and separated by a bare zone. Thus, similarly to muscle, according to the scheme of Fig. 3.1 minifilaments exert inward contractile force since myosins move towards actin barbed ends. Motor activity is regulated biochemically by phosphorylation of the myosin regulatory light chain[94]: when phosphorylated (unphosphorylated) a given myosin molecule is active (inactive). Each sarcomere has multiple minifilaments which may be aggregated as observed previously in fibroblast lamellipodia.[11]

Because stress fibers in stationary cells usually exert isometric tension and changes are slow, it has been difficult to observe their dynamics and hence identify mechanisms. However, a recent experimental study has provided the first measurements of the kinetics of intact stress fibers in living cells. Using agents that increase myosin phosphorylation, Peterson *et al* stimulated the myosin in stress fibers of living fibroblasts.[41] Tagging myosin II regulatory light chain and α-actinin with green fluorescent protein, time-dependent sarcomere lengths were tracked, providing detailed kinetic information previously unavailable. Interestingly, the effect of stimulation was dramatically spatially nonuniform: myosin in the peripheral regions became

more phosphorylated than myosin in the center and then, over the course of ~10 min, peripheral sarcomeres contracted while those close to the fiber center expanded. While the overall length of the fiber decreased little, individual sarcomeres changed lengths considerably. Under normal conditions all sarcomeres were approximately 1 μm in length, while sarcomeres contracted or expanded by as much as 0.5 μm after stimulation.

Here, we develop a quantitative model of stress fibers and apply the model to describe the experiments of Peterson *et al*. Previous theoretical work on actomyosin fibers[95,96] addressed nonpolar bundles motivated in part by experiments in which disordered bundles of actin and myosin fragments in the absence of passive crosslinkers contracted *in vitro.*[97] These bundles are very different from stress fibers, which have a more ordered structure, passive crosslinkers, and actin turnover (discussed below). The formation and alignment of many stress fibers in a cell has been theoretically studied[98-100], but these works addressed collective behavior and did not attempt detailed descriptions of individual stress fibers. Denoth *et al* modeled muscle fibrils and studied how sarcomeres having different properties influence each other, which is related to our interest here.[101] However, no model exists which relates stress fiber mechanisms to physical structure.

In addition to myosin's active contractile force, our model includes a passive elastic force due to cellular titin. The recent discovery that c-titin is associated with stress fibers in a periodic spatial pattern[91] strongly suggests the role of a template, similar to that in muscle, which maintains the periodic α-actinin–myosin arrangement and provides passive elasticity in response to sarcomere length changes tending to undo the templated arrangement. Single molecules of titin from muscle cells have elastic constants $k_t \approx 3.75$ pN/μm at lengths relevant for stress fibers.[102] In fact, we find that stress fibers cannot reach steady state without the inclusion of such

passive elasticity; within our model's general framework, we are forced to introduce a titin-like presence to explain the experiments of Peterson et al.[41]

The final element in our model is actin turnover, which plays a central role. Several experimental studies have shown that actin in stress fibers turns over on a timescale of minutes[42-44], similar to the sarcomere expansion/contraction timescales observed by Peterson et al[41] and suggesting a possible role in the kinetics. Thus actin polymerization/depolymerization processes occur along the fibers, possibly localized to specific centers of activity. Actin has been observed to preferentially incorporate into the Z-line-like α-actinin regions,[103] where the barbed ends are located. This suggests growth at the barbed ends, possibly assisted and/or regulated by protein machinery. It is natural to speculate that formin may assume such a role,[104] since it is known to nucleate and regulate growth of unbranched actin filaments of the type stress fibers contain. However, while formin is involved in the creation of stress fibers,[43,105] no evidence exists to date for their presence in mature fibers. Turning to depolymerization, this may occur at the relatively unstable pointed ends. Another possibility is that the actin severing protein cofilin is involved; stress fibers thicken and become more prominent in cofilin knockdown cells.[106]

Given the poor current understanding of turnover, we adopt the simplest possible model, assuming growth at the barbed ends at rate v_+ (filament length per second), and depolymerization rate v_- at the pointed ends. A key point is that in steady state these are equal, $v_+ = v_-$, and hence one or both must presumably be regulated: when a filament becomes too long or short, polymerization and/or depolymerization rates will adjust accordingly. That is, filament length and polymerization/depolymerization rates are presumably coupled. (A proposed mechanism whereby v_+ and v_- adjust independently of filament length suffers from the difficulty that even when $v_+ = v_-$ growth rate fluctuations, characterized by a 'length diffusivity', would lead to

uncontrolled growth or attrition.[107]) This coupling may be mechanical or biochemical. Here for simplicity we take v_+ fixed and allow v_- to be regulated via the following mechanical mechanism. For a given sarcomere length, the longer the filaments the greater the overlap of the oppositely oriented filaments at their pointed ends in the A-band-like myosin regions; this overlap will eventually build up a resistance force, if only because only so much actin filament can fit into the limited space and specific geometry. This force is the feedback, increasing v_- and allowing a steady state overlap where $v_+ = v_-$. The two essential ingredients are: (i) resistance force dependence on overlap and (ii) depolymerization rate dependence on resistance force. Our picture is motivated in part by the observation that the pointed ends of actin in stress fiber sarcomeres almost always overlap[108] and that overlap forces arise in striated muscle, often described with a length-dependent tension.[109]

A key parameter in our model is p^*, the characteristic overlap force which must be attained before depolymerization is significantly increased. Though we invoke a specific feedback mechanism here, we propose that regardless of the details of the actual depolymerization-length coupling mechanism certain basic features identified by this model have generality. An example is p^*, the characteristic force where polymerization/depolymerization rates become modified.

What forces does turnover generate? This is simplest to see in steady state, where actin filaments treadmill at rate v_+. It follows that the myosins are effectively walking along their actin tracks with velocity v_+ (see Fig. 3.1) and the force they exert is reduced from the stall force by λv_+ where $-\lambda$ is the slope of the myosin force–velocity relation near stall (assuming a small force reduction). Equivalently, one can think of myosins as always pulling with the stall force and λ as an effective internal drag coefficient provided by the myosin system; λv_+ is then the viscous drag

force due to treadmilling, which will contribute to the stress fiber tension. This illustrates how the tension in general depends on turnover rates.

We will see that the magnitude of the turnover rate is naturally measured by an important parameter,

$$r \equiv \lambda v_+ / p^*. \tag{3.1}$$

For the experiments of Peterson et al,[41] we estimate $r \approx 0.1$. In this slow turnover limit, $r << 1$, the dissipative turnover force is small but we find that turnover governs the sarcomere relaxation kinetics: one of our principal predictions is that the sarcomere relaxation time is $\tau_{sarc} = p^*/(k_t v_+)$. Applied to the system of Peterson et al,[41] this yields a relaxation time of order minutes, in agreement with the observed kinetics.

The plan of this chapter is as follows. In section II, we detail the various components of a stress fiber and assemble our model equations. In section III, isotonic boundary conditions are considered, the simplest case where sarcomeres are independent which nonetheless reveals most of the physics of stress fiber kinetics. We find that the overlap force and depolymerization rate are fast variables, relaxing very rapidly to a quasi-steady state and subsequently following the slow sarcomere length variables. Two possible limiting cases emerge, large turnover rate ($r >> 1$) and small turnover rate ($r << 1$), exhibiting qualitatively different behavior. We argue that typical stress fiber systems, in particular those of Peterson et al,[41] belong to the $r << 1$ case. Isometric boundary conditions are treated in section IV, in which coupling between sarcomeres is necessary to enforce constant length. In section V, we apply our model to the experiments of Peterson *et al*[41] and demonstrate that the predicted dynamics are in good agreement with the experiment. We conclude with a discussion in section VI.

II. Model of Stress Fibers

Each end of the stress fiber of N sarcomeres, $n = 1, 2, \ldots, N$, is connected to a focal adhesion, a transmembrane protein complex adhered to the extracellular matrix. Fig. 3.1 shows a schematic of the structure of one sarcomere and the forces involved. The total contractile force exerted by a myosin minifilament is

$$f_{\text{myo}} = f_{\text{s}} - \lambda v_{\text{myo}}, \tag{3.2}$$

where f_{s} is the stall force per minifilament and $v_{\text{myo}}/2$ the myosin velocity relative to its actin track. Thus v_{myo} is defined for convenience to be the sum of the myosin working speeds at each end of the minifilament. $-\lambda$ is the slope of the myosin force–velocity relation at the stall force. Fig. 3.2 shows schematically such a relation with a form similar to that measured for muscle.[92] To our knowledge, no such measurements exist for nonmuscle myosin minifilaments. For our main purpose here, analysis of the experiments of Peterson et al,[41] Eq. 3.2 is an accurate description since the observed velocities were very small, $v_{\text{myo}}/2 << v^0_{\text{myo}}$, where v^0_{myo} is the zero-load myosin working velocity (see Fig. 3.2). The only relevant feature of the force-velocity relation is the magnitude of λ.

Stress fibers contain a form of titin arranged periodically along the fiber axis.[91] Its sequence is very similar to that of striated muscle titin,[91] which passively resists stretching of the sarcomere.[110] Cellular titin is likely to have a similar role in stress fibers, so we assume an elastic restoring force. Assuming similar properties to muscle titin,[102] for the range of experimentally observed sarcomere lengths (~1 μm) a relation linear in sarcomere length x is valid:

$$f_{\text{titin}} = k_{\text{t}} x, \tag{3.3}$$

where k_{t} is the titin force constant whose value in muscle is $k_{\text{t}} \approx 3.75$ pN/μm.[102] *In vitro*, titin assembles with myosin into stress-fiber-like structures in a one-to-one ratio.[111] Thus we assume

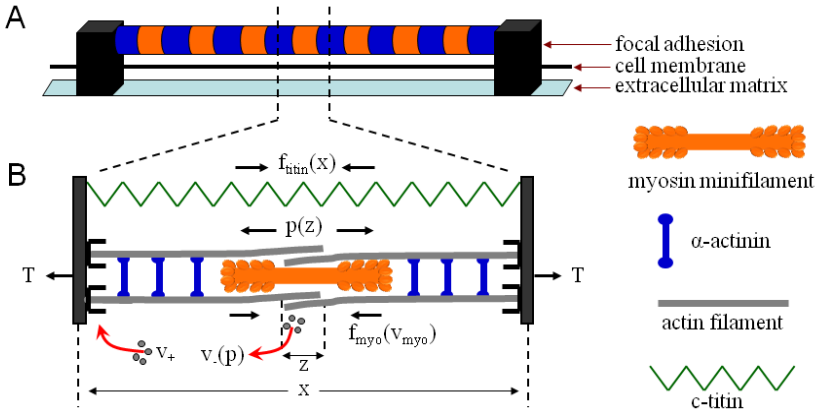

Figure 3.1: Schematic of the stress fiber model.
(A) Along the stress fiber axis, regions containing myosin (orange) alternate with regions containing α-actinin (blue). Each end of the fiber connects to a focal adhesion, a transmembrane protein complex that is anchored to the extracellular matrix.
(B) Considerable evidence indicates stress fibers have a sarcomeric structure built from actin (gray), myosin (orange), and titin (green). Our model incorporates a contractile force f_{myo} from the motor activity of nonmuscle myosin II minifilaments depending on the relative myosin-actin velocity v_{myo} and a passive elastic force f_{titin}, proportional to sarcomere length x, from the giant protein c-titin. The fiber tension T is transmitted from neighboring sarcomeres and is expansive. Also acting to expand the sarcomere is the force p resisting overlap of actin filaments at their pointed ends (shown schematically as if resulting from bending of overlapped filaments). The overlap force is a function of the amount of overlap z and tends to augment the pointed end depolymerization rate v_-. Actin polymerization occurs at constant rate v_+ at barbed ends. The barbed ends lie in the α-actinin-containing regions (shown blue in part (A)) somewhat analogous to the Z-lines in striated muscle. Note v_+ and v_- are defined per sarcomere so each is the sum of identical contributions from the two oppositely oriented actins defining the sarcomere.

one titin molecule per minifilament, and Eq. 3.3 represents the force per minifilament.

Evidence suggests that opposing actin filaments in stress fibers are normally overlapped at the pointed ends in the central A-band-like zone,[108] unlike striated muscle where there is no overlap over much of the range of operating sarcomere lengths.[112] Here we assume overlap above a certain threshold generates a resistance force p per minifilament which for simplicity follows a linear law,

$$p = kz\,, \quad (z > 0)\,, \tag{3.4}$$

where k is the force constant and z is the amount of overlap above the threshold value. The force vanishes for $z < 0$. Its precise origin is unknown but contributions may include simple excluded

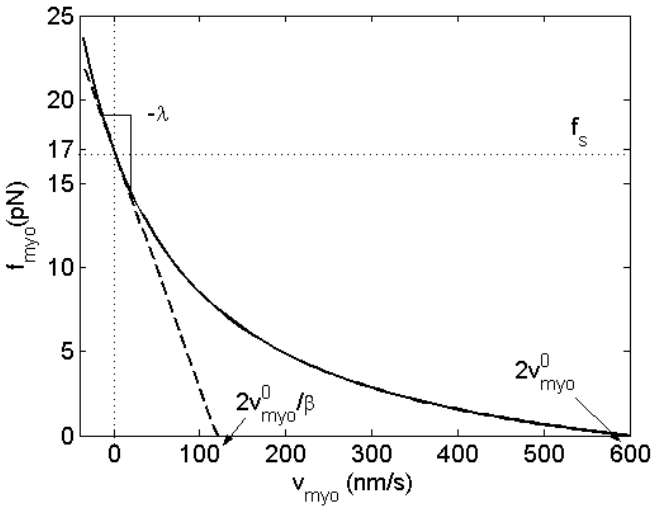

Figure 3.2: Proposed force-velocity relation for a nonmuscle myosin minifilament.
The net force generated by the myosins, f_{myo}, is shown as a function of twice the actin filament–minifilament relative velocity, v_{myo}. (Thus v_{myo} would be the sarcomere shrinkage rate in the absence of polymerization.) Principal features include the zero-load myosin working velocity, v^0_{myo}, the stall force f_s and the slope at the stall force, −λ, which can be interpreted as a myosin internal drag coefficient. Only v^0_{myo} has been measured directly for nonmuscle myosin II, found to be v^0_{myo} ≈ 300 nm/s in gliding assays.[113,114] We assume that the stall force per myosin molecule and the shape of the force-velocity relation are as for muscle myosin II. The internal myosin drag coefficient is $\lambda = \beta f_s/(2\,v^0_{myo})$ where $f_s/(2\,v^0_{myo})$ would be the coefficient for a linear force-velocity relation and β accounts for curvature. We set β = 5, the value for striated muscle.[92,115]

volume, among opposing actin filaments or actin filaments and myosin, and actin filament bending.

As discussed in the introduction we account for actin turnover by assuming simple treadmilling of actin monomers, adding at constant rate v_+ at the barbed ends and dissociating at regulatable rate v_- at the pointed ends (see Fig. 3.1). Note that these rates are defined per sarcomere, and thus are the sum of identical contributions from actin filaments of both polarities. At one or both ends cappers or other polymerization machinery may be involved, but this is unknown. Since the pointed end overlap force p is caused by filament growth, it is assumed to influence pointed end depolymerization according to

$$v_- = v_-^0 \, e^{p/p^*} , \tag{3.5}$$

where p^* is a characteristic force level at which this feedback becomes substantial. Here v_-^0 is the force-free depolymerization velocity. From general considerations one expects a linear dependence at small p and a strong possibly exponential form at large p.[116] The particular form of Eq. 3.5 is simply a convenient interpolation between these two limits and does not qualitatively affect our results. The only important feature is that depolymerization is amplified at some characteristic force, p^*.

Let us now assemble the sarcomere dynamics from the above forces according to the scheme of Fig. 3.1. Consider a given sarcomere of length x in a fiber at tension T per myosin minifilament. The force balance on this sarcomere reads

$$T = f_{\text{myo}} + f_{\text{titin}} - p \ , \tag{3.6}$$

and the myosin working velocity is

$$v_{\text{myo}} = v_+ - \dot{x} \ , \tag{3.7}$$

where the dot denotes differentiation with respect to time.

Thus, combining Eqs. 3.2–3.4, 3.6 and 3.7, the length kinetics are

$$\lambda \dot{x} = -k_t x + kz - f_s + \lambda v_+ + T , \tag{3.8}$$

together with the length constraint

$$\dot{x} + \dot{z} = v_+ - v_-^0 \, e^{kz/p^*} \tag{3.9}$$

Equations 3.8 and 3.9, plus appropriate boundary conditions (for example, isotonic or isometric) and initial conditions on length x and overlap z are a closed system.

In the following, we have in mind experiments where initially a fiber is far from steady state. In Peterson et al[41] this is induced by a position-dependent phosphorylation stimulus, such that stall force f_s and internal drag coefficient λ are different in different sarcomeres. Thus $x(0)$

and $z(0)$ deviate from their $t\to\infty$ values for the given sarcomere. It is understood that x, z, f_s and λ are in general different in different sarcomeres.

Steady state values will be denoted by subscript ∞. We will often deal with the deviations from steady state,

$$y \equiv x - x_\infty, \quad \delta z \equiv z - z_\infty, \quad \delta T \equiv T - T_\infty. \tag{3.10}$$

III. Stress Fiber at Constant Tension

Under isotonic conditions the stress fiber is held at constant tension while the total length, $L = \sum_{n=1}^{N} x_n$, can vary. Thus sarcomeres are independent of each other, a considerable simplification. This will help us to understand the more complex and probably more physiologically important isometric kinetics (section 4) which are realized in the experiments of Peterson et al.[41] Moreover, an intriguing possibility would be to create isotonic conditions in experiments involving controlled deformable substrates.

In what follows, we assume that at $t = 0$ the fiber is perturbed from steady state, for example, by a sudden change in applied tension or myosin phosphorylation profile. First, let us establish what the steady state will be under these new conditions. Then we analyze the process of relaxation to this new steady state.

Steady state

In steady state, the polymerization and depolymerization rates are equal. This can only be achieved by the overlap z adjusting to the value z_∞ such that $v_- = v_+$. Thus, from Eq. 3.9,

$$z_\infty = z^* \ln(v_+ / v_-^0) , \quad z^* \equiv p^*/k . \tag{3.11}$$

z^* is the characteristic overlap where depolymerization is substantially promoted. Clearly, the condition $v_+ > v_-^0$ must be satisfied for this mechanism of turnover regulation. Since depolymerization responds with exponential strength, even away from steady state the overlap z will normally be of order z^* or less. From Eq. 3.8, the steady state sarcomere length x_∞ is given by

$$k_t x_\infty = T - f_s + \lambda v_+ + k z_\infty \ . \tag{3.12}$$

Note the effect of turnover: both the polymerization term, λv_+, and that associated with depolymerization, kz_∞, tend to lengthen the sarcomere for a given tension. The former is the dissipative work done by myosin against internal viscosity to maintain the steady state treadmilling rate v_+; the latter is the compressive overlap force needed to equalize the actin on and off rates.

Relaxation kinetics: two timescales

A striking and simplifying feature of the kinetics now emerges: it turns out that the overlap z is a fast variable, enslaved to the slow sarcomere length variable x. Our procedure will be to first assume the two relevant timescales separate, and then after solving the dynamics perform a self-consistency check which yields a necessary condition for this to be true; we will see that for realistic parameter values this condition is indeed satisfied. Typically, overlap and polymerization rate relax in order seconds, while length relaxation requires minutes.

It is convenient to deal with the sarcomere length and overlap relative to their ultimate steady state values, y and δz. Strong sarcomeres ($y > 0$) will contract, whereas weak sarcomeres ($y < 0$) will expand. In this language, Eqs. 3.8 and 3.9 become

$$\lambda \dot{y} = -k_t y + k\, \delta z \ , \tag{3.13}$$

and

$$\dot{y} + \dot{z} = v_+ - v_-^0 e^{z/z^*} \quad . \tag{3.14}$$

Eliminating $\dot{y}$ from Eqs. 3.13 and 3.14 yields the overlap dynamics:

$$\lambda \dot{z} = \lambda v_+ (1 - e^{\delta z/z^*}) - k\,\delta z + k_t y, \tag{3.15}$$

after using Eq. 3.11. Near steady state the overlap z is of order z^*, so the two z-dependent terms have characteristic values λv_+ and p^*, respectively. The dimensionless turnover parameter $r \equiv \lambda v_+/p^*$, introduced in Eq. 3.1, measures the relative magnitude of this pair. This is a key parameter: the physics of relaxation are qualitatively different in the two cases of small and large r, respectively.

Fast turnover, $r >> 1$

In this case the myosin-associated drag force is much larger than the overlap force, so the overlap dynamics, Eq. 3.15, simplify to

$$\lambda \dot{z} \approx \lambda v_+ (1 - e^{\delta z/z^*}) + k_t y \quad . \tag{3.16}$$

Assume y is slowly varying and can be treated as approximately constant in Eq. 3.16. Then in a timescale $\sim\tau_{olap}$ the overlap relaxes to a value obeying

$$\lambda v_+ (1 - e^{\delta z/z^*}) \approx -k_t y \quad , \quad \tau_{olap} = z^*/v_+. \tag{3.17}$$

This is the quasi-steady state relation, rapidly established in time $\sim\tau_{olap}$. It describes the subsequent enslavement of the overlap variable z to the slow sarcomere length variable y.

To better understand the nature of this early relaxation process, note that for large enough r we can expand the exponential in Eqs. 3.16 and 3.17 so the short time dynamics and quasi-steady state approximate

$$\dot{z} \approx -\frac{v_+ \delta z}{z^*} + \frac{k_t y}{\lambda} \quad , \quad k\,\delta z = k_t y/r \qquad (t > \tau_{olap}). \tag{3.18}$$

Provided $r > k_t y/p^*$, expanding the exponentials is valid. It follows that the $k\delta z$ term can be neglected in Eq. 3.13 and hence the relative change in y by the time τ_{olap} is order $k_t/(rk) << 1$. Thus, during the fast phase sarcomere length is essentially constant, $y = y_0 \equiv y(t = 0)$, as is the sarcomere velocity $\dot{y} \approx -k_t y_0/\lambda$. Noting that the rate of increase in the filament length l_{fil} is equal to $v_+ - v_-$, the overlap dynamics (Eq. 3.18) can be rewritten as $\dot{z} = dl_{fil}/dt - \dot{y}$. This articulates the physical process during the fast phase as follows. Considering a contractile sarcomere as an example, initially the overlap increases as the sarcomere shrinks at constant filament length, $\dot{z} = -\dot{y}$ (since initially $dl_{fil}/dt = 0$); but this increase in overlap increases the depolymerization rate, so now $dl_{fil}/dt < 0$. This continues until in quasi-steady state the rate of decrease of filament length just matches the constant sarcomere shrinking rate. Since $\dot{y}$ is a constant, the fast timescale for $\dot{z}$ to relax is the polymerization relaxation time in Eq. 3.18, z^*/v_+. When quasi-steady state is reached the overlap is fixed (or more precisely, it is changing very slowly) and the filament length is decreasing as it 'melts' into the overlap region. Overall, during the early fast phase overlap is tuned until the filament grows or shrinks together with, and at the same rate as, the shrinking or growing sarcomere.

For longer times, $t >> \tau_{olap}$, sarcomere lengths change slowly with overlap enslaved according to Eq. 3.18, $k\,\delta z = k_t y/r$. Note that the deviation of the overlap from its steady state value is very small. The overlap and hence filament shrinkage rate decrease in proportion to the sarcomere excess length y. The slow y dynamics are obtained by using the quasi-steady state relationship for z, Eq. 3.17, in Eq. 3.14:

$$\lambda \dot{y} \approx -k_t y \quad , \quad y = y_0 e^{-t/\tau_{sarc}} \quad , \quad \tau_{sarc} = \lambda/k_t, \tag{3.19}$$

where y_0 is the initial value of y. Note that for these times the overlap is relaxed and the $\dot{z}$ term negligible. Thus, sarcomere length has simple exponential relaxation kinetics. The relaxation time τ_{sarc} is identified as the time required for the sarcomere to change length so the force imbalance caused by the initial perturbation is corrected by a suitable stretch or contraction of titin, the titin forces working against the myosin-derived internal drag coefficient λ. The timescale is independent of v_+, reflecting the fact that the filament length is continuously and very rapidly readjusted to the current conditions and actin growth/shrinkage is not rate limiting. Interestingly, under all conditions in this model, the presence of titin is required for the fiber to reach a new steady state.

The self-consistency condition for timescale separation is

$$\tau_{olap}/\tau_{sarc} = k_t/(kr) << 1. \tag{3.20}$$

Now we will see later that the overlap spring constant k typically exceeds that of the weak titin spring, $k_t \approx 3.75$ pN/μm.[102] Thus, the timescales are well separated and the above procedure is validated for large r.

Slow turnover, $r << 1$

We will argue in below that for real stress fibers the turnover parameter r is normally very small. Then the overlap resistance is much larger than the internal drag term in the short time z dynamics (Eq. 3.15), which are now

$$\lambda \dot{z} \approx -k\,\delta z + k_t y. \tag{3.21}$$

Treating the slow y variable as constant, it follows that the overlap relaxes ($\delta z \sim 1 - e^{-t/\tau_{olap}}$) after time τ_{olap} to a quasi-steady state value obeying

$$k\,\delta z = k_t y \quad , \quad \tau_{olap} = \lambda/k. \tag{3.22}$$

Whereas for large r the overlap relaxation time derived from turnover, in the present case of slow turnover the filament length is approximately fixed and the quasi force balance, Eq. 3.22, is achieved by translating the entire filament by adjusting the overlap. Since y is assumed to change little in τ_{olap}, only the overlap force p changes substantially during this process. It thus sets the timescale, $\tau_{olap} = \lambda/k$, working against the weak myosin internal drag. For instance, if the tension was reduced at $t = 0$, the overlap force would quickly increase to balance the now effectively stronger myosin. From Eq. 3.14 with the small turnover terms discarded, the changes during τ_{olap} obey $\Delta y \approx -\Delta z$. Thus in order that the relative change in y be small, it is required that $k >> k_t$ be satisfied. This condition is expected to be satisfied for actual stress fibers (see below).

Using this quasi-steady state z value in Eq. 3.14 with $\dot{z}$ neglected, the slow y dynamics are

$$\dot{y} = v_+(1-e^{-k_t y/p^*}). \tag{3.23}$$

Thus,

$$y = -(p^*/k_t)\ln[1 + (e^{-y_0 k_t/p^*} - 1)\, e^{-t/\tau_{sarc}}] \quad , \quad \tau_{sarc} = p^*/(k_t v_+) . \tag{3.24}$$

If the initial value y_0 exceeds p^*/k_t, then Eq. 3.24 describes an initial rapid phase where y drops from y_0 to ~p^*/k_t, followed by the late behavior

$$y \approx (p^*/k_t)\, e^{-t/\tau_{sarc}} \quad , \quad t >> \tau_{sarc}. \tag{3.25}$$

During this relaxation, the titin spring force must adjust for the sarcomere length to reach a new steady state. Since the overlap changes very little during quasi-steady state ($\Delta z/\Delta y = k_t/k << 1$ from Eq. 3.22), the actin filaments must change length if the sarcomere is to change length. This length change depends on the slow turnover processes which are rate limiting. Hence the turnover 'viscous drag', p^*/v_+, sets the relaxation time τ_{sarc}.

The condition for timescale separation is

$$\tau_{olap}/\tau_{sarc} = (k_t/k)r << 1, \tag{3.26}$$

which is always satisfied for this slow turnover case.

Connection between the *r* parameter and timescales

It is illuminating to note that the turnover parameter *r* can be written as the ratio of the overlap relaxation timescales in the two cases,

$$r = \frac{\lambda / k}{z^* / v_+} \quad . \tag{3.27}$$

These timescales originate in the two different mechanisms for changing the overlap: turnover and overlap force. The fastest process sets the overlap relaxation time.

Similarly, *r* can be written as the ratio of the two sarcomere relaxation timescales:

$$r = \frac{\lambda / k_t}{p^* / (k_t v_+)} \ . \tag{3.28}$$

In contrast to the short time overlap dynamics, the *slowest* mechanism sets the timescale for long time sarcomere relaxation.

IV. Stress Fiber at Constant Length

Under isometric conditions the total length of the stress fiber, $L = \sum_{n=1}^{N} x_n$, is constant. This is probably the more physiologically relevant condition because stress fiber ends are often connected to immobile focal adhesions. Our particular interest in the present paper is to model the experiments of Peterson *et al*,[41] where conditions were approximately isometric: though focal adhesions slowly moved centripetally as the stress fiber contracted, the relative change in the

entire fiber length was significantly less than the relative length changes of individual sarcomeres.

We consider an initially uniform fiber, every sarcomere having length $l = L/N$. Note the mean length will equal l at all times. At $t = 0$, a perturbation is imposed such that the myosin activity profile is nonuniform along the fiber. We assume the myosin heads of a sarcomere work independently in parallel, so changing the number of active heads changes the maximum force that can be generated but not the maximum velocity. Thus the slope λ increases in proportion to the stall force f_s. The activity of a given sarcomere is characterized by the relative deviation of its stall force and slope from the mean values:

$$\varepsilon \equiv \frac{f_s - \bar{f}_s}{\bar{f}_s} = \frac{\lambda - \overline{\lambda}}{\overline{\lambda}} \quad . \tag{3.29}$$

Angular brackets and overbar will be used interchangeably to denote averages over all sarcomeres, e.g. $\overline{\lambda} \equiv \langle \lambda \rangle$. A sarcomere with $\varepsilon > 0$ ($\varepsilon < 0$) is relatively strong (weak). Average values such as $\langle \varepsilon^2 \rangle$ represent the variation in sarcomere activities across the entire fiber.

In the experiments of Peterson et al[41] the variation in measured phosphorylation levels was small, $|\varepsilon| << 1$. In this case one can obtain explicit analytical expressions which clearly articulate the basic mechanisms. We specialize to this case at the end of this section.

Steady state

In steady state the overlap must adjust to equalize the actin on and off rates, so z_∞ is unchanged from the expression for the isotonic case, Eq. 3.11. Averaging Eq. 3.8 in steady state over all sarcomeres gives the steady state tension,

$$T_\infty = \bar{f}_s - v_+ \bar{\lambda} + k_t l - k z_\infty . \tag{3.30}$$

Note that if a perturbation changes the average level of myosin activation then the steady state tension will change by an amount $\Delta T_\infty = \Delta \bar{f}_s - v_+ \bar{\lambda}$.

Subtracting Eq. 3.8 from its average, both at steady state, gives the steady state sarcomere length

$$k_t x_\infty = k_t l - \varepsilon \bar{f}_s + v_+ \varepsilon \bar{\lambda} . \tag{3.31}$$

Stronger sarcomeres ($\varepsilon > 0$) will end up shorter than weaker ones ($\varepsilon < 0$).

Relaxation kinetics

In terms of the relative variables, the sarcomere dynamics (Eqs. 3.8 and 3.9) are

$$\lambda \dot{y} = -k_t y + k\, \delta z + \delta T(t) , \quad \dot{y} + \dot{z} = v_+ (1 - e^{\delta z / z^*}) \quad . \tag{3.32}$$

These are as for isotonic conditions except for the new time-dependent tension term. Just before the $t = 0$ perturbation the fiber was uniform and at steady state, so using Eq. 3.31 the initial conditions ($t = 0+$) are

$$k_t y_0 = \varepsilon (\bar{f}_s - v_+ \bar{\lambda}) , \qquad z(0) = z_\infty . \tag{3.33}$$

The tension is determined by the isometric constraint. Dividing the first expression of Eq. 3.32 by λ and averaging,

$$\delta T = \frac{k_t \langle y / \lambda \rangle - k \langle \delta z / \lambda \rangle}{\langle 1 / \lambda \rangle} \quad . \tag{3.34}$$

It follows that the initial tension is lower than T_∞

$$\delta T(0) = \frac{\langle \varepsilon / (1+\varepsilon) \rangle}{\langle 1/(1+\varepsilon) \rangle} \left(\bar{f}_s - v_+ \bar{\lambda} \right) \approx - \langle \varepsilon^2 \rangle \left(\bar{f}_s - v_+ \bar{\lambda} \right) , \quad (|\varepsilon| << 1), \tag{3.35}$$

after using $\lambda = (1 + \varepsilon)\,\overline{\lambda}$. Interestingly, for small ε this deviation is second order, proportional to the squared sarcomere strength fluctuation.

Eliminating $\dot{y}$ from Eq. 3.32 gives the isometric overlap dynamics

$$\lambda \dot{z} = \lambda v_{+}(1-e^{\delta z/z^{*}}) - k\,\delta z + k_t y - \delta T \ . \tag{3.36}$$

Fast turnover, *r* >> 1

Discarding the overlap force term in Eq. 3.36, the overlap relaxation kinetics are

$$\lambda \dot{z} \approx \lambda v_{+}(1-e^{\delta z/z^{*}}) + k_t y - \delta T \ . \tag{3.37}$$

The overlap relaxes after time τ_{olap} to the following quasi-steady state relation

$$\lambda v_{+}(1-e^{\delta z/z^{*}}) \approx -k_t y + \delta T\,,\ \ \frac{\delta z}{z^{*}} = \ln\left(1+\frac{k_t y - \delta T}{\lambda v_{+}}\right)\ \ ,\ t \geq \tau_{olap} = \frac{z^{*}}{v_{+}} \ . \tag{3.38}$$

Thus the long time slow dynamics (Eq. 3.32) are

$$\lambda(\dot{y} + \dot{z}) \approx -k_t y + \delta T \ . \tag{3.39}$$

Now, from Eq. 3.38

$$\dot{z} = \left(\frac{k_t \dot{y}}{kr} - \frac{\delta \dot{T}}{kr}\right)\ln\left(1+\frac{k_t y - \delta T}{\lambda v_{+}}\right) \ . \tag{3.40}$$

Inserting this into Eq. 3.39, the first term $\sim k_t \dot{y}\,/(kr)$ is negligible while the second term $\sim \delta\dot{T}\,/(kr)$ relaxes to essentially zero after the short timescale τ_{olap}. It follows that $\dot{z}$ can be discarded in the slow dynamics:

$$\dot{y} + \frac{k_t y}{\lambda} \approx \frac{\delta T}{\lambda}\ \ ,\ \delta T = \frac{k_t \langle y/\lambda \rangle}{\langle 1/\lambda \rangle}\ \ , \tag{3.41}$$

where the slow tension dynamics were obtained by averaging the sarcomere length dynamics whose relaxation time is of order

$$\tau_{\text{sarc}} = \bar{\lambda}\,/k_{\text{t}}\ . \tag{3.42}$$

Note that the ratio of timescales is very small, $\tau_{\text{olap}}/\tau_{\text{sarc}} \approx k_{\text{t}}/(kr)$, justifying the separation of the fast and slow dynamical episodes when the polymerization parameter r is large.

Solving the length dynamics (Eq. 3.41) analytically is difficult in general. However, when the variation among sarcomeres is small, $\varepsilon << 1$, the leading order solution is easily obtained as follows. Using $\lambda = (1 + \varepsilon)\,\bar{\lambda}$ we have

$$\delta T = -\left\langle \varepsilon k_{\text{t}} y \right\rangle\ ,\ \dot{y}\ + k_{\text{t}} y/\lambda = 0\ ,\ (\varepsilon << 1)\ , \tag{3.43}$$

having solution

$$k_{\text{t}} y(t) = \varepsilon(\,\bar{f}_{\text{s}} - v_{+}\bar{\lambda}\,)\,\mathrm{e}^{-t/\tau_{\text{sarc}}}\ ,\qquad \delta T = -\left\langle \varepsilon^2 \right\rangle(\,\bar{f}_{\text{s}} - v_{+}\bar{\lambda}\,)\,\mathrm{e}^{-t/\tau_{\text{sarc}}}\ , \tag{3.44}$$

where we used the initial condition (Eq. 3.33) and the fact that y changes very little during the fast episode. Thus while sarcomere length deviations are first order, tension deviations are very small and second order, proportional to the squared fluctuation in phosphorylation levels across the fiber.

Slow turnover, $r << 1$

Discarding the turnover term in Eq. 3.36, the overlap dynamics approximate

$$\lambda\,\dot{z}\ \approx -k\,\delta z + k_{\text{t}} y - \delta T\ ,\ \delta T \approx \frac{k_{\text{t}}\left\langle y_0/\lambda \right\rangle - k\left\langle \delta z/\lambda \right\rangle}{\left\langle 1/\lambda \right\rangle}\,. \tag{3.45}$$

The expression for the tension was obtained as follows. In this small polymerization limit the filament length is approximately unchanged on the overlap relaxation timescale τ_{olap}, i.e. the turnover terms in Eq. 3.32 effectively vanish whence $\langle \dot{z} \rangle = -\langle \dot{y} \rangle = 0$. Thus the mean relative overlap $\langle \delta z \rangle$, initially zero, remains approximately zero throughout this early episode. Dividing

the overlap dynamics in Eq. 3.45 by λ and averaging then gives the expression for δT after assuming y changes negligibly during τ_{olap}. Note that the same result is available directly from Eq. 3.34.

In solving the fast dynamics system (Eq. 3.45) the length variable y is treated as constant; self-consistently, therefore, its relative change must be small. This is a closed system for the N overlaps and the tension, having N eigenvalues of order $\bar{\lambda}/k$. Thus after a timescale of order τ_{olap} it will relax to the quasi-steady state relation

$$k\delta z \approx k_t y - \delta T\,, \quad (t > \tau_{olap} = \bar{\lambda}/k)\,. \tag{3.46}$$

Our starting point for the slow y dynamics is the length constraint (Eq. 3.32)

$$\dot{y} = v_+(1-e^{k\delta z/p^*}) - \dot{z} \approx v_+(1-e^{(k_t y-\delta T)/p^*}) + \delta\dot{T}/k \quad , \tag{3.47}$$

where we used the quasi-steady state expression (Eq. 3.46) to eliminate the overlap and $k_t \dot{y}/k$ was discarded since the overlap spring constant typically greatly exceeds that of titin. Averaging and using the isometric constraint yields the tension dynamics

$$\delta\dot{T} = -kv_+\left\langle 1 - e^{(k_t y-\delta T)/p^*}\right\rangle \quad . \tag{3.48}$$

Note that to determine the tension it is important to include the contribution from $\dot{z}$, namely the $\delta\dot{T}$ term. Indeed the average value, $\langle\dot{z}\rangle$, is the mean rate of increase in the filament length and omission of this term would miss an important intermediate time behavior in the tension, as will become clear.

The closed system, Eqs. 3.47 and 3.48, is solved to yield y and δT time profiles. In general this is difficult. Fortunately we can execute this procedure exactly to leading order for the experimentally relevant case of small ε. This is done in the next section.

Slow turnover: small sarcomere variation, ε << 1.

This subsection treats the situation relevant to the experiments of Peterson et al[41]: slow turnover (r << 1) and small variation across the fiber, ε << 1.We now solve the equations established in the previous section to leading order in ε.

It will be shown that for all times $y \sim \varepsilon$ is first order, whereas $\delta T \sim \varepsilon^2$ is second. Now in Eq. 3.45 $y = y_0$ is essentially constant, and from Eq. 3.33 $k_t y_0 \approx \varepsilon \bar{f}_s$, neglecting the small turnover term. Thus the tension term can be discarded in the overlap dynamics, Eq. 3.45, giving simple exponential behavior

$$k\delta z = \varepsilon \bar{f}_s (1 - e^{-t/\tau_{olap}}), \quad \tau_{olap} = \bar{\lambda}/k. \tag{3.49}$$

Using this result for the tension in Eq. 3.45 one gets to leading order

$$\delta T = -\left\langle \varepsilon^2 \right\rangle \bar{f}_s e^{-t/\tau_{olap}} \qquad t \le \tau_{olap}. \tag{3.50}$$

This confirms that the tension deviation is *second* order during the fast relaxation episode. Tensions change relatively little due to cancellation of the effects of sarcomeres which are, respectively, contractile and expansive relative to the mean.

Note: (i) for $t > \tau_{olap}$, since to first order $k_t y = k\delta z$ from Eq. 3.46, and from Eq. 3.49 $k\delta z = k_t y_0$, it follows that y retains its initial value to this order. This confirms that its relative changes in the early fast phase are small (second order or higher), a requirement for the slow-fast separation. (ii) Equation 3.50 is invalid for times beyond τ_{olap}, when the effects of the neglected (de)polymerization terms become important.

Turning to the long time behavior, let us obtain the sarcomere length evolution to leading order from Eq. 3.47. Discarding the second-order tension terms, expanding to order ε and using the initial condition $k_t y_0 = \varepsilon \bar{f}_s$ one has

$$\dot{y} = -\frac{k_t v_+}{p^*} y \ , \qquad k_t y = k_t y_0 \, \mathrm{e}^{-t/\tau_{\mathrm{sarc}}} = \varepsilon \bar{f}_s \, \mathrm{e}^{-t/\tau_{\mathrm{sarc}}} \ , \quad \tau_{\mathrm{sarc}} = \frac{p^*}{k_t v_+} \ . \tag{3.51}$$

This is one of our principal conclusions. Since relaxation requires actin filament lengths to attain their equilibrium value, the sarcomere length relaxation time τ_{sarc} is set by the slow rate-limiting turnover processes. This confirms that the timescale ratio is small, $\tau_{\mathrm{olap}}/\tau_{\mathrm{sarc}} = k_t r/k << 1$, justifying the fast–slow separation. Note that in fact our expansion in (47) presumed $\varepsilon < p^*/\bar{f}_s$ a slightly more stringent condition on ε. For example, we estimate $p^*/\bar{f}_s \approx 0.25$ for the experiments of Peterson et al.[41]

Finally, let us derive the tension to leading order. Using our result for y (Eq. 3.51) in the tension dynamics (Eq. 3.48), expanding the exponential and noting the average of all $O(\varepsilon)$ terms vanishes one finds the tension obeys a first-order differential equation

$$\delta \dot{T} = \frac{r \delta T}{\tau_{\mathrm{olap}}} + \frac{\langle \varepsilon^2 \rangle \bar{f}_s^2}{2 p^*} \frac{r}{\tau_{\mathrm{olap}}} \mathrm{e}^{-2t/\tau_{\mathrm{sarc}}} \ , \tag{3.52}$$

after retaining the leading $O(\varepsilon^2)$ terms only. This phase begins at $t \geq \tau_{\mathrm{olap}}$ when δT is close to zero, see Eq. 3.50. Thus we take as initial condition $\delta T(0) = 0$, since τ_{olap} is a much smaller timescale than those featuring in Eq. 3.52. After assuming $\tau_{\mathrm{olap}}/(r\tau_{\mathrm{sarc}}) = k_t/k << 1$, the solution is the difference of two exponentials

$$\frac{\delta T}{\bar{f}_s} = \frac{\langle \varepsilon^2 \rangle \bar{f}_s}{2 p^*} \left(\mathrm{e}^{-2t/\tau_{\mathrm{sarc}}} - \mathrm{e}^{-rt/\tau_{\mathrm{olap}}} \right) \ , \tag{3.53}$$

confirming that the tension deviation is $O(\varepsilon^2)$. The time evolution of the tension is interesting: in addition to the expected sarcomere relaxation time τ_{sarc}, a second much shorter timescale τ_{olap}/r features, intermediate between the short (τ_{olap}) and long (τ_{sarc}) scales. For example, in the experiments of Peterson et al[41] we estimate $\tau_{\mathrm{olap}} \approx 1$ s, $\tau_{\mathrm{olap}}/r \approx 10$ s and $\tau_{\mathrm{sarc}} \approx 6$ min. The tension

is initially a rising exponential involving the shorter timescale, $\delta T \sim 1 - \mathrm{e}^{-rt/\tau_{\mathrm{olap}}}$. A peak value $\delta T_{\max}$ is then reached after time

$$t_{\max} = \frac{\tau_{\mathrm{olap}}}{r} \ln\left(\frac{r\tau_{\mathrm{sarc}}}{2\tau_{\mathrm{olap}}}\right) \quad , \quad \frac{\delta T_{\max}}{\bar{f}_{\mathrm{s}}} = \frac{\left\langle \varepsilon^2 \right\rangle \bar{f}_{\mathrm{s}}}{2p^*} \quad . \tag{3.54}$$

For the experiments of Peterson et al,[41] we predict $t_{\max} \approx 29$ s. The late stages, comprising most of the decay, entail exponential fall off $\sim \mathrm{e}^{-2t/\tau_{\mathrm{sarc}}}$ with time constant one half of the long sarcomere relaxation timescale.

V. Application to Stress Fiber Relaxation Experiments

Our model identifies two qualitatively distinct classes of kinetics, depending on the value of the dimensionless turnover rate parameter, r. To which class do actual stress fibers belong? We estimate the overlap force where depolymerization is first amplified as $p^* = mk_{\mathrm{B}}T/\delta \approx 4$ pN, where $\delta = 2.7$ nm is the effective actin monomer size.[116] Here $m = 3$ is the number of actin filaments per minifilament, which we take to be the same as that in muscle.[117] The polymerization velocity is available from turnover experiments in which an actin renewal timescale of ~5 min was measured.[44] For the end-to-end treadmilling turnover mechanism employed in our model, this translates into a barbed end polymerization rate that is the sarcomere length, ~1 μm,[41] divided by the turnover time, or $v_+ \approx 3$ nm/s. Next, we estimate roughly the slope of the myosin force-velocity relation $\bar{\lambda} \approx \beta \bar{f}_{\mathrm{s}} / \left(2v_{\mathrm{myo}}^0\right)$, where v_{myo}^0 is the zero-load myosin velocity and the factor β accounts for curvature in the relation (see Fig. 3.2). Although β is unknown for nonmuscle myosin, we use $\beta = 5$, the value for striated muscle.[92,115] Each myosin molecule can exert ~1.7 pN of force at stall[83] and each myosin minifilament contains 10–30

myosin molecules.[11] Assuming ten molecules on each side of the minifilament gives $\bar{f}_s \approx 17$ pN. We also take $v_{myo}^0 \approx 300$ nm/s from gliding assays.[113,114] Thus we estimate

$$r \approx \frac{\beta \bar{f}_s v_+}{2p^* v_{myo}^0} \approx 0.1 \quad . \tag{3.55}$$

This suggests that real stress fibers will normally follow slow turnover kinetics, the $r << 1$ case treated in the previous section.

We now apply our framework to the approximately isometric studies by Peterson *et al.*[41] This type of experiment is schematized in Fig. 3.3. Initially the fiber was in nearly uniform steady state, all sarcomeres of approximately equal length and having the same level of phosphorylation. At time $t = 0$, the addition of a myosin activator apparently caused an imbalance in the number of myosins phosphorylated in different sarcomeres: sarcomeres near the fiber ends became more activated than those near the center. The peripheral sarcomeres then contracted while those in the center expanded. After some minutes the fiber reached a new steady state.

The data of Peterson et al[41] indicate that $|\varepsilon|$ is small because the apparent ratio of myosin activation in end sarcomeres to those in the center was ~1.15. Our model thus predicts that the fast overlap dynamics will be those of Eq. 3.49, $k\delta z = \varepsilon \bar{f}_s (1 - e^{-t/\tau_{olap}})$ where the overlap relaxation time is $\tau_{olap} = \bar{\lambda}/k$. From the discussion above, $\bar{\lambda} \approx 1.4 \times 10^{-4}$ N·s/m. The value of the overlap force constant k is unknown. Assuming overlap builds up a substantial force over some fraction of the full sarcomere length ~1 μm, we crudely estimate the critical overlap $z^* = 50$ nm, giving $k = 0.1$ pN/nm. The overlap relaxation timescale is then $\tau_{olap} \approx 1$ s. Note that provided k is much larger than the titin force constant k_t (required for the relative sarcomere length change to

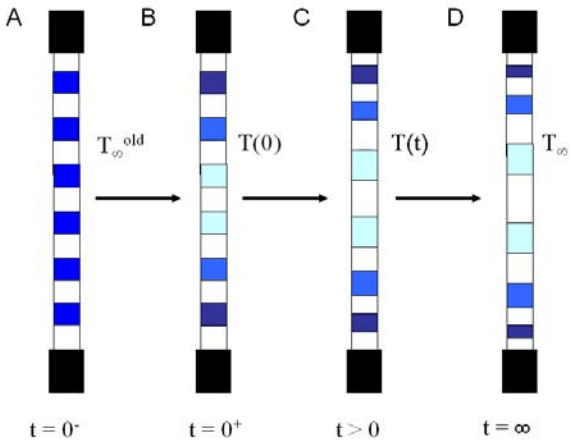

Figure 3.3: Schematic of sequence of events during stress fiber relaxation.
Blue regions containing myosin alternate with white regions containing α-actinin and $T(t)$ denotes the tension at time t.
(A) Before $t = 0$, the stress fiber is at steady state with all sarcomeres of approximately equal length and having equal myosin activities.
(B) At $t = 0$ a perturbation is applied causing variable numbers of active myosin heads in different sarcomeres. Stronger sarcomeres are represented as darker than weaker ones, with strength relative to the mean characterized by the parameter ε. The tension immediately changes to some new value, $T(0)$.
(C) Nonuniform myosin strength causes the sarcomeres to start changing length until a new steady state is reached in (D) where the stronger sarcomeres are now shorter than the weaker ones. The tension evolves throughout to enforce a constant stress fiber length.

be small during the fast overlap adjustment phase) the sarcomere length dynamics are insensitive to the value of k.

Turning to the long time relaxation, since it is likely that the condition $\varepsilon < p^*/f_s \approx 0.24$ is satisfied (see Fig. 3.5) for the sarcomeres in Peterson et al[41] it follows that the relevant model prediction is given in Eq. 3.51: $y = y_0 e^{-t/\tau_{sarc}}$ with $\tau_{sarc} = p^*/(k_t v_+)$. For initially uniform stress fibers, $y_0 = \varepsilon f_s/k_t$ from Eq. 3.33. Taking $k_t \approx 3.75\times10^{-3}$ pN/nm,[102] the sarcomere length relaxation timescale is $\tau_{sarc} \approx 6$ min.

In Fig. 3.4, model predictions for sarcomere length versus time are directly compared to experiment. Experimental data is reproduced from Fig. 3.4 of Peterson et al.[41] Peterson *et al* measured the kinetics of central sarcomeres (defined to be within a 10 μm region about the stress fiber midpoint) and peripheral sarcomeres (defined to be within 7 μm of a focal adhesion) under

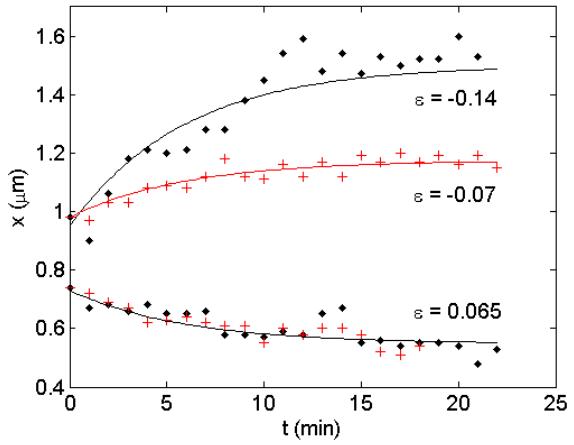

Figure 3.4: Comparison of model predictions for sarcomere length evolution to experimental data.
Experimental data reproduced from figure 4 of Peterson et al.[41] Plus signs: experimental data from cells stimulated by calyculin A. Diamonds: experimental data from cells stimulated by LPA. Shrinking sarcomeres are from peripheral regions of stress fibers and expanding sarcomeres from the central region. Solid lines are analytical solutions from Eq. 3.51, $y = y_0 e^{-t/\tau_{sarc}}$, where $\tau_{sarc} = p^*/(k_t v_+) \approx 6$ min and initial sarcomere length was chosen to match the experimental data. ε was used as a fitting parameter. All other parameter values are as estimated in section 5: the minifilament stall force $\bar{f}_s$ = 17 pN, the myosin internal drag coefficient $\bar{\lambda}$ = 1.4×10^{-4} N·s/m, the barbed end polymerization velocity v_+ = 3 nm/s, the characteristic overlap force p^* = 4 pN, and the titin spring constant k_t = 3.75×10^{-3} pN/nm.

the influence of two different myosin activators. These data are compared to our analytical solutions from Eq. 3.51 using ε as a fitting parameter since the full ε profile was unknown in the experiment. All other parameter values were chosen as estimated above. The predicted relaxation kinetics are in good agreement with the experimental data. The differences in the magnitude of expansion may be attributable to differences in how the two myosin activators affect the ε profile or the average amount of myosin in each sarcomere.

To make predictions pertaining to all sections of the fiber, a full ε profile is needed, which can be roughly estimated from the data of Peterson et al.[41] The apparent ratio of myosin activation in end sarcomeres to those in the center was ~1.15. Assuming a continuous symmetric profile, the simplest possibility is a quadratic profile as shown in Fig. 3.5 for a fiber of 50 sarcomeres, a typical stress fiber length. The fluctuations in ε are then $\langle \varepsilon^2 \rangle \approx 0.002$ and $\langle \varepsilon^2 \rangle^{1/2} \approx 0.04$.

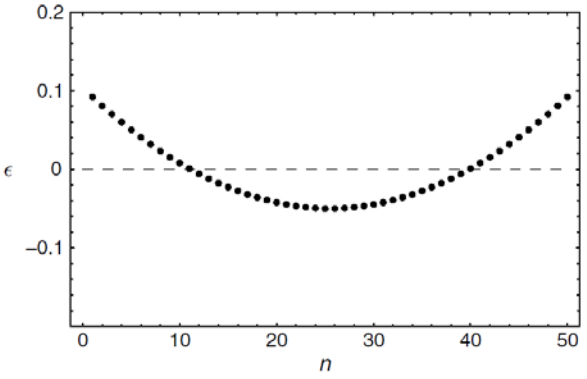

Figure 3.5: Profile of sarcomere strengths for a stress fiber with 50 sarcomeres.
In Peterson et al,[41] the degree of phosphorylation in peripheral sarcomeres was ~1.15-fold greater than that in central sarcomeres, but the full spatial distribution was unknown. Assuming a smooth and symmetric profile, for small enough variation ε the profile will be quadratic. Using the condition $\sum_{n=1}^{N} \varepsilon_n = 0$ results in the quadratic ε profile shown. ε ranges from −0.05 to 0.1 under these conditions. This ε profile is used in Figs. 3.6 and 3.7.

Figure 3.6 presents numerical solutions for the length dynamics of all 50 sarcomeres in a stress fiber with the ε profile of Fig. 3.5 and using all other parameters as defined above. For simplicity we have assumed that all sarcomeres have initial length 1 μm. Analytical solutions are also presented for the most peripheral sarcomere, $n = 1$, and the central sarcomere, $n = 25$. The numerical solutions were obtained by solving the $2N$ coupled ordinary differential equations for sarcomere length and overlap obtained by substituting the expression for the tension, Eq. 3.34, into the y and z dynamics, the first part of Eq. 3.32 and Eq. 3.36, respectively. Note that for the parameter values estimated above, the analytical prediction is very close to the exact numerical solution. Sarcomeres with $\varepsilon > 0$ contract, those with $\varepsilon < 0$ expand and those with very small ε remain approximately unchanged in length throughout the entire episode, as observed in Peterson et al.[41] This is rephrased in Fig. 3.7 as a sarcomere length profile evolving in time. Note that under these conditions of small ε, our model predicts the sarcomere length profile has at all times the same shape as the ε profile (quadratic here) with only the amplitude changing in time. It would be of great interest to experimentally measure the full sarcomere length profile.

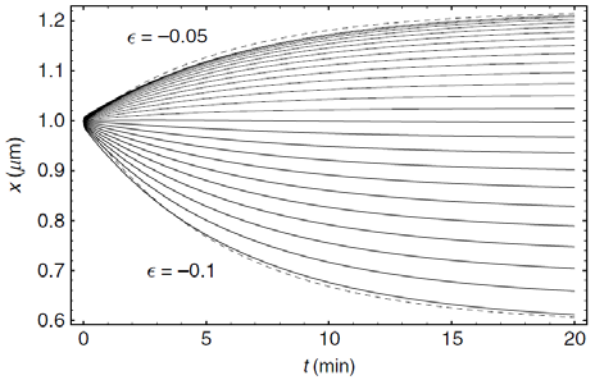

Figure 3.6: Model predictions for the length evolution of all sarcomeres in a 50-sarcomere stress fiber.
Solid lines are exact numerical solutions and dashed lines are analytical solutions for sarcomeres n = 1 and 25 only. Analytical solutions are from Eq. 3.51, $y = \varepsilon f_s e^{-t/\tau_{sarc}}$, where $\tau_{sarc} \approx 6$ min. Analytical and numerical solutions are in close agreement. All parameters values are as for Fig. 3.4 and the ε profile is that of Fig. 3.5. Weak sarcomeres expand (ε < 0, upper curves) while strong sarcomeres contract (ε > 0, lower curves). Sarcomeres with myosin activity near the mean value remain approximately unchanged in length.

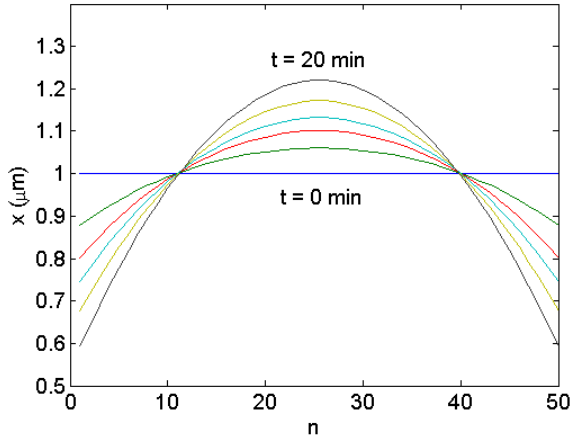

Figure 3.7: Sarcomere length profiles.
Model predictions for sarcomere length profile at t = 0, 2, 4, 6, 10 and 20 min for the 50-sarcomere stress fiber of Fig. 3.6. At all times the profile has the same shape as the ε profile, in this case quadratic; only the amplitude changes. Note that initially all sarcomeres have equal length, l = 1 μm. With time the weak central sarcomeres expand while the strong peripheral sarcomeres shorten. By t = 20 min, the fiber reaches steady state. For a quadratic ε profile, the crossovers between shortening and lengthening sarcomeres are at $n \approx 12$ and 38.

VI. Discussion

Model. We developed a model of stress fibers, basic cytoskeletal contractile machines. Based on currently available experimental information, the model assumes a sarcomeric structure. The essential ingredients are myosin contractility, passive elasticity from c-titin, internal resistance forces due to actin filament overlap and actin turnover. The last two are intimately connected by a feedback mechanism in our model: when interference between opposing actin filaments becomes substantial and the overlap force large, depolymerization rates are augmented. Within this broad framework, such a mechanism is inescapable: in its absence, unlimited

quantities of actin filament could grow and accumulate in the overlap region in a completely unphysical fashion.

Model parameters. These physical elements were measured by a set of key model parameters: (i) f_s and λ, the stall force and internal drag coefficient of a myosin minifilament; (ii) the titin spring constant k_t; (iii) the overlap force constant, k; (iv) v_+, the actin barbed end polymerization rate and (v) p^*, the overlap force above which actin depolymerization is enhanced. Of these, f_s, λ, k_t and v_+ are directly measurable and we have estimated p^*.

Fast turnover-overlap relaxation, slow sarcomere relaxation. Each of the many sarcomeres comprising the fiber contains oppositely-oriented actin filaments which at some instant have a certain growth rate and degree of overlap. An important feature emerging from the model is that the overlap and filament growth or shrinkage rate relax very rapidly in seconds, while sarcomere lengths relax on a much longer timescale of minutes. During this slow relaxation episode filament growth rates adjust very slowly, determined only by the current value of the slowly changing sarcomere lengths. Thus, the fast polymerization-overlap system is enslaved to the slow sarcomere length system.

Fast turnover kinetics. We find that two qualitatively different classes of stress fiber kinetics are possible, depending on whether turnover is rapid or slow. The class a given system belongs to is determined by the dimensionless turnover rate $r \equiv \lambda v_+/p^*$. For systems where turnover is fast, $r >> 1$, filament growth rates can adjust rapidly and are compliant to contractile and elastic forces. Sarcomere kinetics evolve as they would if one simply ignored turnover and filament crowding: sarcomere length change results from contractile myosin and elastic titin forces working against internal myosin viscosity, with the actin filaments compliantly growing or shrinking as the sarcomere grows or shrinks. Hence, the sarcomere relaxation time is

$\tau_{sarc} = \bar{\lambda}/k_t$. The filament growth process offers negligible resistance and does not affect the force balance. During the initial fast phase the actin growth rate is rapidly tuned to match that of the sarcomere by adjusting the overlap, and thereafter the growth rates are maintained equal by continuous slow overlap adjustment in tune with the evolving sarcomere growth rate. The recipe for the overlap to achieve this tuning is the quasi-steady state relation, Eq. 3.38, which for small overlap deviations is $k\delta z = (k_t y - \delta T)/r$. Using Eq. 3.41 and noting filament growth rate equals $-v_+\delta z/z^*$, the quasi-steady state relation translates to an explicit equality of filament and sarcomere growth rates, $v_+ - v_- = -\dot{y}$.

Real stress fibers: slow turnover kinetics. We estimate that real stress fiber systems which have been studied experimentally belong to the slow turnover class, $r << 1$. The behavior is very different since polymerization kinetics are now sluggish and adjustment of actin growth rate requires substantial forces. Myosin and titin forces now determine the filament growth rate not via the sarcomere growth rate, but by a direct force balance: the overlap force matches the myosin and titin forces. There is sufficient time to establish this force balance before filament growth or shrinkage since turnover is slow. Once the overlap force is determined, this determines the filament growth rate which depends only on overlap. The sarcomere can then only change length as fast as the filaments themselves can change length; hence the sarcomere growth rate is equal to this slow rate-limiting filament growth rate. The early fast relaxation episode consists in the filament rapidly translating at fixed length until the overlap matches the myosin and titin forces. Thereafter the overlap maintains this force balance by slow adjustments; this is the quasi-steady state relation $k\delta z = k_t y - \delta T$, Eq. 3.46, which determines the filament and sarcomere growth rate $\dot{y} = -v_+\delta z/z^* \approx -v_+(k_t y - \delta T)/p^*$ taking small overlap as an example. This result shows how the sarcomere relaxation time results from titin elastic forces acting on the

polymerization-overlap system to determine filament growth or shrinkage. The polymerization-overlap system has an effective internal 'drag coefficient' equal to p^*/v_+, since an imposed force p^* generates a response in filament growth rate of order v_+. Thus the relaxation time is

$$\tau_{\text{sarc}} = \frac{p^*}{k_t v_+} \quad . \tag{3.56}$$

This is one of the model's principal predictions.

Experimental stress fiber systems. We applied our model to the experiments of Peterson *et al*[41] in which sarcomere expansion and contraction was observed after myosin stimulation. For such stress fiber systems we estimate the dimensionless turnover parameter $r \approx 0.1$, squarely in the slow turnover class. We estimate $p^* = 4$ pN and used the muscle titin value $k_t \approx 3.75\times10^{-3}$ pN/nm,[102] while $v_+ \approx 3$ nm/s is available from experimental actin turnover measurements.[44] Using these in Eq. 3.56 gives $\tau_{\text{sarc}} \approx 6$ min, close to the observed relaxation time. Note that even though several model parameter values (f_s, β and k_t) were estimated from striated muscle, τ_{sarc} differs from muscle sarcomere relaxation times which are typically on the order of seconds.[118,119] This is as expected since the stress fiber mechanisms articulated by the present model are quite different to those believed to govern muscle. Whereas we predict that actin filament length change is the rate-limiting process in stress fibers, it has been proposed that in striated muscle actin filament length is maintained constant by the molecular ruler nebulin[120] or by the activity of the pointed end capping protein tropomodulin.[121] Moreover, in striated muscle actin does not undergo treadmilling[121] in contrast to stress fibers.[103]

Effect of sarcomere variation amplitude. An important aspect of the relaxation kinetics is the extent of myosin activity variation along the fiber from differential stimulation. The relative variation is named ε in our model. For the experiments of Peterson et al[41] this was apparently

small, with $|\varepsilon|$ likely to be considerably less than unity for all sarcomeres. For this case we find that sarcomere length changes during relaxation are $O(\varepsilon)$ whereas tension changes are much smaller, $\sim O(\varepsilon^2)$. Our model as phrased here is geared for relatively small ε; we note that for larger variations, $\varepsilon > 0.2$, it generates unphysical negative sarcomere lengths. In reality, when a sarcomere becomes as short as the length of a myosin minifilament, ~0.3 μm, minifilaments from adjacent sarcomeres would abut and prevent further contraction.

Role of cellular titin. We find that a force that responds to sarcomere length is necessary in order for a stable steady state sarcomere length profile to be possible. The discovery of c-titin in stress fibers[91] strongly suggests titin fulfills this role, and further emphasizes the similarity between the well-known sarcomeric structure of muscle and that of stress fibers. It is possible that titin has additional and more complex roles. A kinase domain that may actively respond to force in muscle is present in c-titin.[91]

Actin turnover mechanism and its regulation. Turnover regulation is necessary in order that a steady state be accessible but the precise mode of turnover and the mechanisms regulating it are unknown. Our model invokes a simple feedback mechanism whereby pointed end overlap promotes pointed end dissociation. Other possible mechanisms include regulation of the severing protein cofilin which may play an important role in actin disassembly as suggested by recent experiments using cofilin knockdown cells.[106] It has been suggested that cofilin's actin binding mechanism[122] could make its activity force-dependent.[123] Another possibility is that the pointed end depolymerization rate is fixed and regulation occurs instead through force-sensitivity of nucleators at the polymerizing barbed end, possibly formins.[123-125] The detailed behavior depends on structural details near the barbed end and is beyond the scope of the present paper. For example, if one assumes the titin connects to a Z-line-like region but not directly to actin

filaments, as in Fig. 3.1, we find a timescale $\tau_{sarc} = p^*/(k_t v_-^0)$ where p^* now denotes the threshold value of the force tending to pull the nucleator away from the barbed end above which the actin association rate is strongly augmented. Whatever particular mechanisms may turn out to be operative, our model has attempted to articulate certain quite general features. For example, the relaxation time of Eq. 3.56 may have broad significance provided the characteristic turnover rate v_+ and threshold force p^* are appropriately reinterpreted. Future and more detailed experimental studies of stress fiber kinetics promise to shed light on these important questions.

Chapter 4

Recoil after Severing Reveals Stress Fiber Contraction Mechanisms

In this chapter, we develop a mathematical model of stress fibers motivated by an experiment in which stress fibers in living cells were severed with laser nanoscissors. The severed fibers recoiled rapidly over ~5 s. The dramatic recoil allowed us to use our model to determine the balance of internal and external forces on the fiber, and to make predictions of fiber behavior in the presence of viscous connections between the stress fiber and its surroundings. This model was published in 2009.[126]

I. Introduction

In many processes, cells assemble force-producing contractile machines from myosin motor proteins, actin filaments, and other structural and regulatory components. Examples include the muscle myofibril whose contraction pumps the heart or moves limbs, the contractile ring that pinches the cell into two daughters during cytokinesis, and the stress fiber. Stress fibers are tension-generating actomyosin bundles terminating at one or both ends in transmembrane focal adhesions anchored to the extracellular matrix (see Fig. 4.1). By coupling to the extracellular matrix and exerting force, they enable cells to mechanically influence their environment and sense its mechanical properties. Stress fibers contribute to adhesion of vascular endothelial cells to the basal lamina,[34] generate contraction in myofibroblasts which provokes tissue reorganization during wound healing,[5] and may assist cells in migration.[39]

What are the working parts of stress fibers and how do they coordinate to generate force? Stress fibers are similar in some respects to the thoroughly studied myofibrils of striated muscle.[6] A myofibril is built from many contractile repeat units (i.e., sarcomeres) arranged in series, each comprising an array of parallel bipolar myosin aggregates (i.e., thick filaments) interdigitated with two oppositely oriented actin filament arrays, one on either side. Sarcomeres contract when thick filament myosins pull inward on the actin arrays whose pointed ends lie in the central myosin zone. The actin barbed ends and the actin cross-linker α-actinin reside at the sarcomere boundaries (i.e., Z disks) which are connected to the thick filament centers by the giant spring-like protein titin.

Stress fibers in stationary cells appear to be organized in a sarcomeric myofibril-like fashion. Along the fiber axis, zones of α-actinin alternate with zones of nonmuscle myosin-II[41] and actin polarity alternates periodically.[39] Moreover, a nonmuscle isoform of titin, c-titin, localizes periodically to stress fibers.[91] Thus, it is natural to ask whether the operating principles are similar to those of myofibrils. Striated muscle sarcomere kinetics depends on two fundamental relations: the isometric sarcomere force-length relation[109] (see Fig. 4.2) and the force-velocity relation giving myosin-generated force versus sarcomere contraction velocity.[92] The analogous relations for stress fibers, if they exist, are unknown.

Establishing a representative model of stress fibers is challenging because in stationary cultured cells they normally exert isometric tension with little kinetic activity that could reveal contraction mechanisms. Laser ablation is a powerful method that can reveal otherwise hidden internal forces in such situations. Recently Kumar et al. severed single stress fibers in living endothelial cells using femtosecond laser ablation and measured rapid fiber recoil (~1 μm/s) over ~5 s (see Fig. 4.1).[44] Although contractility of isolated stress fibers was previously

demonstrated,[127] the quantitative nature of the in vivo data of Kumar et al.[44] provides the opportunity for quantitative modeling of stress fiber mechanisms. We will argue that because such large velocities are realized, recoil kinetics reveal information not only about the internal fiber machinery but also about its coupling to the cellular environment.

Several models of stress fibers have been developed. In the tensegrity model of Luo et al.,[128] tension from viscoelastic cables is resisted by elastic struts under compression. This is a general framework successfully reproducing observed recoil kinetics and other features such as widening of the severed ends.[44] However, the model's relationship to the measured sarcomeric organization and actin filament polarity distribution of stress fibers is not direct. Other models aimed to explain the relaxation kinetics after chemical stimulation observed by Peterson et al.[41] Stachowiak and O'Shaughnessy investigated the role of actin turnover in stress fiber relaxation (Chapter 3),[86] while Besser and Schwarz proposed a feedback loop between focal adhesion-based signaling and fiber contraction.[129]

Here, we develop a systematic quantitative model of the stress fiber based on known components and existing experimental findings. The model consists of a balance of forces in a sarcomeric organization: (1) Contractile forces, exerted by nonmuscle myosin II, characterized by a force-velocity relation. (2) Elastic forces, characterized by a force-length relation that we infer from experimental data. (3) Viscous forces, both internal and external to the fiber. Applied to the kinetics revealed by the fiber-severing assay, the model predicts a stress fiber force-length relation similar to that of muscle. We find that the internal viscosity is relatively small but substantial external drag forces act on the retracting fiber, corresponding to an effective cytosolic viscosity $\sim 10^4$ times that of water. In addition to nonspecific interactions, this may reflect

specific interactions with cytoskeletal or membrane proteins. Thus, the severed stress fiber can be viewed as a natural internal probe of the cell's effective viscosity.

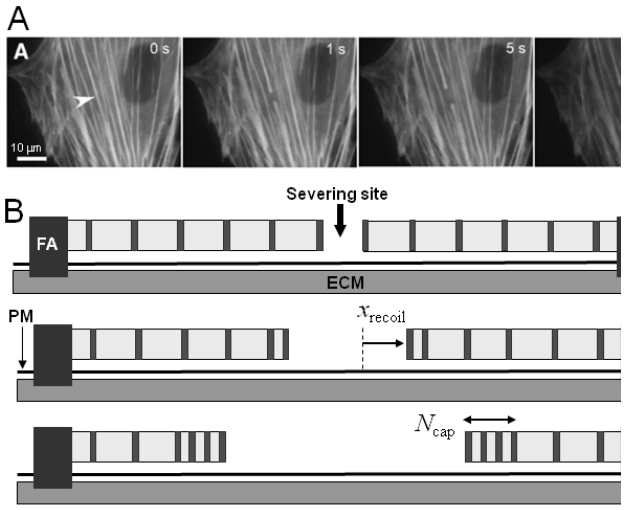

Figure 4.1: Recoil of severed stress fibers. (A) Kumar et al. tracked EYFP-actin stress fiber recoil after severing with a femtosecond laser nanoscissor.[44] (Arrowhead) Incision position. (B) Schematic of a severed stress fiber. Regions of myosin (dark) alternate with α-actinin (light). Each fiber end connects to a focal adhesion (FA) anchored to the extracellular matrix (ECM) through the plasma membrane (PM). Our model predicts that sarcomeres near the severed end contract first, resulting in a growing cap of N_{cap} collapsed sarcomeres.

II. Stress Fiber Forces

Contractile force

Stress fiber contraction depends on nonmuscle myosin-II motor proteins,[44,127] which aggregate into ~0.3 μm long bipolar minifilaments, each containing 10–30 molecules.[11,93] Both minifilament formation and force generation are promoted by phosphorylation of the myosin regulatory light chain,[94] which is regulated by both myosin light chain kinase (MLCK) and Rho-kinase (ROCK).[130] In a sarcomeric arrangement, motor activity is characterized by a force-velocity relation by analogy with striated muscle.[92] Although this relation has not been measured for nonmuscle myosin II, several principal features can be estimated (see Table 4.1): (1) From gliding assays, the maximum rate at which bipolar minifilaments can contract a sarcomere (at zero load) is $v_{myo}^{0} \approx 0.6$ μm/s.[113] (2) The stall force of a minifilament (at zero velocity) is

estimated to be $f_s \approx 17$ pN, using measurements of muscle myosin-II since nonmuscle myosin-II forces have not been directly measured to the best of our knowledge. (3) The slope of the force-velocity relation at stall, γ_{myo} (same meaning as λ in Chapter 3).

Elastic forces: force-length relation

The striated muscle force-length relation is well established[109] and is typically represented as isometric tension versus sarcomere length as in Fig. 4.2A. On the ascending limb, tension decreases with decreasing sarcomere length where actin pointed ends first overlap in the myosin region. Tension decreases more rapidly in the steepest portion at the onset of compressive stresses when thick filaments are forced against Z disks.[109,131] Although the stress fiber force-length relation has not been directly measured in living cells, two experiments suggest a similar form with two distinct regions on the ascending limb (see Fig. 4.2B): (Experiment 1) Peterson et al. treated fibroblasts with the phosphatase inhibitor calyculin A,[41] inducing small spatial variations in myosin phosphorylation level about the mean value along stress fibers. This caused peripheral (central) sarcomeres to contract (expand). Now a sarcomere whose myosin stall force is δf_s per minifilament above the mean will contract distance $\Delta x \approx \delta f_s/k$, where k is the stress fiber force constant per minifilament. Stachowiak and O'Shaughnessy[86] estimated that $\delta f_s = 0.06 f_s$ for those sarcomeres which contracted by amount $\delta x = 0.3$ μm,[41] implying $k \approx 3.4$ pN/μm. This is a small value, close to that of muscle titin.[102] (Experiment 2) Other evidence suggests that a much larger value onsets at smaller lengths: sarcomeres shrank an estimated amount $d_{sarc} \approx 0.28$ μm after severing[44] (see Table 4.1), reaching a collapsed state where enough compressive force developed to balance the tensile myosin stall force. The force constant required to stall myosin after a contraction of d_{sarc} is >>3.4 pN/μm.

Thus, taken together, Experiments 1 and 2 suggest a force-length relation with two distinct portions in its ascending limb as in Fig. 4.2B. One portion reflects tensile forces, perhaps from c-titin, which are much smaller than the myosin contractile forces (elastic constant k_2); the other reflects strong compressive forces at short sarcomere lengths (elastic constant k_1). The latter stalls contraction after severing at sarcomere length $x_{\text{sarc}}^{\text{coll}} = x_{\text{sarc}}^{0} - d_{\text{sarc}}$, where x_{sarc}^{0} is the initial sarcomere length.

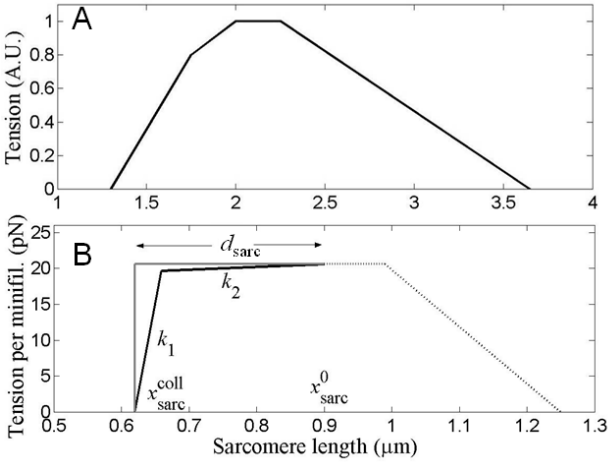

Figure 4.2: Force-length relations.
(A) Striated muscle sarcomere force-length relation measured by Gordon et al.[109] The ascending limb spans lengths ~1.3–2 μm.
(B) Proposed stress fiber force-length relation: a shallow, tensile leg with elastic constant k_2 = 4 pN/μm and a steep, compressive leg with elastic constant k_1 = 500 pN/μm intersect at length $x_{\text{sarc}}^{*} = [f_s + k_1(x_{\text{sarc}}^{0} - d_{\text{sarc}})](k_1 - k_2)^{-1} \approx 0.66$ μm. At the minimum length $x_{\text{sarc}}^{\text{coll}} = x_{\text{sarc}}^{0} - d_{\text{sarc}} \approx 0.62$ μm (collapsed sarcomere) the elastic resistance stalls the myosin. Hard core limit in gray.

Viscous forces

Two classes of viscous drag forces may be present. Internal drag depends on the sarcomere contraction velocity whereas external drag depends on the relative velocity between the stress fiber and its surroundings. We will find that the existing experimental data cannot be explained without invoking external viscous forces.

III. Model of Severed Stress Fibers

The model

In this section, a model is built incorporating the forces discussed in the previous section. The model, depicted in Fig. 4.3, describes one of the two stress fiber pieces after severing, comprising N_{tot} sarcomeres in series. The severed end is free (n = 1), whereas the other end is anchored to a focal adhesion ($n = N_{tot}$). Fiber kinetics results from the balance of contractile, elastic, and viscous forces acting on each sarcomere of length x_{sarc} and contraction velocity v_{sarc}.

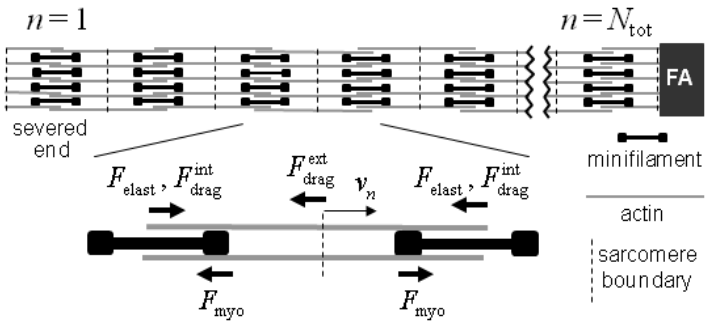

Figure 4.3: Model of severed stress fibers.
External drag acts on bipolar actin bundle n, proportional to its velocity v_n. Other forces are internal drag, elastic, and myosin forces from sarcomeres to its left and right (see Eq. 4.1).

The contractile myosin force in each sarcomere obeys force-velocity relation $F_{myo}(v_{sarc})$ per minifilament. Since this has not been measured for stress fibers, we consider two forms: (1) Linear, $F_{myo} = f_s - \gamma_{myo} v_{sarc}$. (2) The well-known hyperbolic Hill relation for muscle,[92] $F_{myo}/f_s = \alpha(v_{sarc}/v_{myo}^0 + \beta)^{-1} - \beta$, where α and β are dimensionless parameters.

In each sarcomere, the elastic force per minifilament at longer sarcomere lengths is $F_{elast}(x_{sarc}) = k_2 x_{sarc}$, which reflects weak tensile force, possibly from titin. Below a threshold sarcomere length x_{sarc}^* strong compressive forces onset, $F_{elast}(x_{sarc}) = k_1(x_{sarc} - x_{sarc}^{coll}) - f_s$; which balance the stall force at the collapsed sarcomere length x_{sarc}^{coll}. Thus the maximum possible

sarcomere shrinkage is $d_{\text{sarc}} \equiv x_{\text{sarc}}^{0} - x_{\text{sarc}}^{\text{coll}}$. The elastic force is presented in Fig. 4.2B is an isometric force-length relation (summed with the myosin contribution) to aid comparison with the analogous relation for muscle of Fig. 4.2A.

The internal and external drag forces per minifilament are determined by the corresponding friction coefficients γ_{int} and γ_{ext}: $F_{\text{drag}}^{\text{int}}(v_{\text{sarc}}) = \gamma_{\text{int}} v_{\text{sarc}}$ and $F_{\text{drag}}^{\text{ext}}(v) = \gamma_{\text{ext}} v$, where v is actin velocity relative to the cytoplasm.

It is convenient to apply the force balance to the n^{th} bipolar actin bundle at x_{n} moving with velocity v_{n}, pulled by two minifilaments to either side (see Fig. 4.3). Thus, sarcomere n has length $x_{\text{sarc}} = x_{\text{n+1}} - x_{\text{n}}$ and contraction velocity $v_{\text{sarc}} = v_{\text{n}} - v_{\text{n+1}}$. The force balance reads

$$\begin{aligned} F_{\text{drag}}^{\text{ext}}(v_{\text{n}}) = & -F_{\text{myo}}(v_{\text{n-1}} - v_{\text{n}}) + F_{\text{myo}}(v_{\text{n}} - v_{\text{n+1}}) \\ & + F_{\text{drag}}^{\text{int}}(v_{\text{n-1}} - v_{\text{n}}) - F_{\text{drag}}^{\text{int}}(v_{\text{n}} - v_{\text{n+1}}) \\ & - F_{\text{elast}}(x_{\text{n}} - x_{\text{n-1}}) + F_{\text{elast}}(x_{\text{n+1}} - x_{\text{n}}) \end{aligned} \quad . \qquad (4.1)$$

The severed-end boundary condition ($n = 1$) is $F_{\text{drag}}^{\text{ext}}(v) = F_{\text{myo}}(v_{\text{sarc}}) + F_{\text{elast}}(x_{\text{sarc}}) - F_{\text{drag}}^{\text{int}}(v_{\text{sarc}})$, since internal forces act on one side of the bundle only, whereas $v = 0$ at the fixed adhesion ($n = N_{\text{tot}} + 1$). Thus, we neglect possible alterations in severed-end sarcomere properties due to laser ablation; for example, the widening of severed ends observed by Kumar et al.[44]

Since $v_{\text{n}} \equiv dx_{\text{n}}/dt$, Eq. 4.1 is a closed system solvable for the time-dependent velocities and locations of all actin bundles (and hence sarcomeres).

Parameters

The parameter values used in our model are listed in Table 4.1. Since stress fiber elastic constants have not been directly measured, we use the muscle value in the steep region (k_1) and

the value for muscle titin in the shallow region (k_2). Note that the internal and external drag coefficients are key parameters that are not known. A major objective of this work is to use our model to infer their values using the measured post-severing recoil data.

Table 4.1: Parameter values in the model of severed stress fibers.

Symbol	Meaning	Value	Legend
	Fixed parameter values		
x_{sarc}^0	Initial sarcomere length	0.9 μm	**(A)**
N_{tot}	Number of sarcomeres	12	**(B)**
d_{sarc}	Sarcomere collapse distance	0.28 μm	**(B)**
f_s	Myosin-II minifilament stall force	17 pN	**(C)**
v_{myo}^0	No-load myosin velocity	0.6 μm/s	**(D)**
γ_{myo}	Force-velocity relation slope	28 pN·s/μm	**(E)**
k_1	Compressive elasticity	500 pN/μm	**(F)**
k_2	Tensile elasticity	4 pN/μm	**(G)**
γ_{ext}	External drag coefficient	5.3 pN·s/μm	**(H)**
γ_{int}	Internal drag coefficient	5.0 pN·s/μm	**(H)**
n_{mini}	Number of minifilaments per sarcomere	50	**(I)**
w	Stress fiber diameter	0.5 μm	**(J)**

Legend:
(A) From Sanger et al.[108]
(B) Images from Kumar et al. indicate relative shortening ~1/3 after severing; total recoil distance was ~3.35 μm.[44] Thus, $N_{\text{tot}} \approx 12$ sarcomeres each shrank by $d_{\text{sarc}} \approx 0.28$ μm.
(C) Assumes 10 myosins on each side of a minifilament,[11] each with the muscle myosin stall force, 1.7 pN[83].
(D) Bipolar minifilaments can contract actin at twice the velocity measured in gliding assays.[113]
(E) For a linear force-velocity relation, $\gamma_{\text{myo}} = f_s / v_{\text{myo}}^0$. Same meaning as λ in Chapter 3.
(F) Value for steep region in striated muscle relation.[109]
(G) From muscle titin.[102]
(H) Fit to experimental data.
(I) Assumes two actin filaments per minifilament[117] and 100 actin filaments in parallel, consistent with electron micrographs showing stress fibers ~10 filaments across.[39]
(J) From Kumar et al.[44]

Dynamics of the collapsed cap

As will become clear, Eq. 4.1 reveals a sequential collapse of sarcomeres propagating inward from the free severed end. After severing, the end sarcomere finds itself in an extraordinarily asymmetrical situation: myosin pulling forces on one side are unopposed by myosins on the other (severed) side. The large imbalance is resisted by weak drag forces only. Thus, the end sarcomere swiftly contracts to its minimum length. This collapsed sarcomere is inactive, its myosin contractility exactly negated by elastic resistance. Hence, the second sarcomere finds itself in the same asymmetrical situation and subsequently collapses, and so on: a collapse front propagates inward, leaving in its wake a growing cap of N_{cap} collapsed sarcomeres at the severed end (Fig. 4.1B).

What equations govern the cap growth in time, $N_{cap}(t)$? Cap dynamics are most clearly phrased in the hard-core model, defined as (1) In the force-length relation, $k_1 \to \infty$ and $k_2 \to 0$, excellent approximations since there is one very shallow and one very steep region (Fig. 4.2B). (2) The continuous limit is taken (v_{n+1} - $v_n \to \partial v/\partial n$, etc.), which accurately describes many sarcomere behavior. (3) A linear force-velocity relation is assumed. Equation 4.1 then simplifies to (see Appendix A for derivation)

$$v = \xi^2 \frac{\partial^2 v}{\partial n^2}, \quad \xi^2 = \frac{\gamma_{myo} + \gamma_{int}}{\gamma_{ext}} \qquad \left(N_{cap} \le n \le N_{tot}\right) \tag{4.2}$$

where the velocity penetration depth ξ plays a crucial role in the severed fiber's evolution. The first N_{cap} sarcomeres are collapsed ($1 \le n < N_{cap}$) whereas this equation describes the uncollapsed portion of the fiber. It is to be solved for the fiber velocity profile $v(n)$ subject to boundary condition $v = \xi^2(v^0_{sarc} + \partial v/\partial n)/N_{cap}$ at the collapse front $n = N_{cap}$, where $v^0_{sarc} \equiv \tilde{f}_s/(\gamma_{myo} + \gamma_{int})$ and $\tilde{f}_s$ is the effective stall force at $t = 0$ including the elastic contribution (see Appendix A). In

Appendix B, we show that the collapsed cap length N_{cap} and sarcomere length profile x_{sarc} obey the equations

$$\frac{dN_{cap}}{dt} = \theta^{-1} v_{sarc}\left(N_{cap}\right), \qquad \theta \equiv \left.\frac{\partial x_{sarc}}{\partial n}\right|_{n=N_{cap}} \tag{4.3}$$
$$\frac{\partial x_{sarc}}{\partial N_{cap}} = -\theta \frac{v_{sarc}(n)}{v_{sarc}\left(N_{cap}\right)},$$

IV. Solutions of Model Equations

For a given cap length N_{cap}, Eq. 4.2 is solved for the stress fiber velocity profile $v(n)$. This gives the severed-end recoil velocity $v_{recoil} = v(N_{cap})$ and the sarcomere contraction velocity profile $v_{sarc} = -\partial v/\partial n$:

$$v_{recoil} = \frac{\xi v_{sarc}^0}{1 + N_{cap}/\xi}, \qquad \left(n \geq N_{cap}\right) \tag{4.4}$$
$$v_{sarc}(n) = -\theta \frac{v_{sarc}^0}{1 + N_{cap}/\xi} e^{-\left(n - N_{cap}\right)/\xi},$$

Short time recoil

Immediately after severing ($N_{cap} = 1$), the first sarcomere contracts with velocity $v_{sarc}^0/(1 + 1/\xi)$ (Eq. 4.4) and collapses in time $\tau_{coll} = \tau_{coll}^0 (1 + 1/\xi)$ where $\tau_{coll}^0 = d_{sarc}/v_{sarc}^0$ and v_{sarc}^0 are, respectively, the collapse time and velocity in the absence of external drag ($\xi \to \infty$). From Eq. 4.4, the length profile at the instant of the first sarcomere collapse is $x_{sarc}(n) = x_{sarc}^0 - d_{sarc} e^{-(n-1)/\xi}$.

Steady state

Equation 4.3 is solved for the sarcomere length profile as a function of cap length in Appendix B. After the first collapse ($t = \tau_{coll}$), a steady-state profile is established relative to the moving collapse front at $n = N_{cap}$:

$$x_{sarc}(n) = x_{sarc}^{0} - d_{sarc} e^{-(n - N_{cap})/\xi} \qquad (t > \tau_{coll},\ n \geq N_{cap}) \tag{4.5}$$

Note this matches the profile at the instant of the first collapse. With $\theta = d_{sarc}/\xi$, Eq. 4.3 is then solved for cap length as a function of time,

$$N_{cap}(t) = \xi\left[\left(2t/\tau_{coll}^{0} - C\right)^{1/2} - 1\right] \qquad (t > \tau_{coll}) \tag{4.6}$$

where $C = 1 - \xi^{-2}$ was determined by the initial condition $N_{cap} = 1$ at $t = \tau_{coll}$.

Initially, the severed end recoils at constant velocity (Eq. 4.4 with $N_{cap} = 1$). Using $N_{cap}(t)$ from Eq. 4.6 in Eq. 4.4 gives the recoil velocity at later times when the steady-state sarcomere profile is established. Thus,

$$x_{recoil}(t) = \begin{cases} \xi v_{sarc}^{0} t/(1 + 1/\xi) & (t < \tau_{coll}) \\ d_{sarc}\xi\left(2t/\tau_{coll}^{0} - C\right)^{1/2} & (t < \tau_{coll}) \end{cases} . \tag{4.7}$$

These results apply until all sarcomeres have collapsed and the stress fiber has length $N_{tot}\, x_{sarc}^{coll}$. This occurs after time $T_{coll} \approx (\tau_{coll}^{0}/2)(N_{tot}/\xi)^2$, obtained by setting $N_{cap} = N_{tot} + 1$ in Eq. 4.6.

V. Model Results and Comparison to Experimental Data

Comparison of Model Results to the Experimental Recoil Curve

In the experiments of Kumar et al.[44] (Fig. 4.1), severed end displacement $x_{recoil}(t)$ was followed in time. The measured recoil is plotted in Fig. 4.4 together with the hard core model predictions, Eq. 4.7 (dashed line), using Table 4.1 parameter values. Also shown are numerical

solutions to the exact discrete model equations (Eq. 4.1), using both the linear (thick solid line) and Hill (dotted line) force-velocity relations. We fitted the numerical solutions to the experimental data[44] using only the drag force coefficients as fitting parameters. For internal drag, the best fit values γ_{int} = 5.0 pN·s/μm (linear) and γ_{int} = 0 (Hill) were considerably less than the effective drag due to myosin, γ_{myo} = 28 pN·s/μm. Best fit external drag coefficients were γ_{ext} = 5.3 pN·s/μm (linear) and γ_{ext} = 4.3 pN·s/μm (Hill).

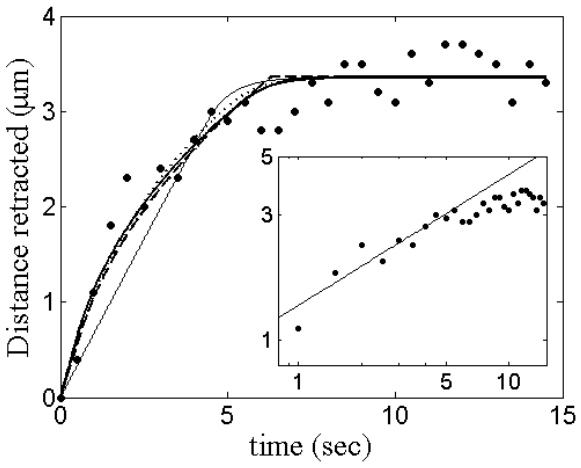

Figure 4.4: Recoil kinetics: model predictions compared to experimental results.
(Solid circles) Experimental data from Kumar et al.[44] (Thick solid line) Numerical solution of Eq. 4.1 using the linear force-velocity relation with best-fit values γ_{ext} = 5.3 pN·s/μm and γ_{int} = 5 pN·s/μm. (Dotted line) Numerical solution using the Hill force-velocity relation with best-fit values γ_{ext} = 4.3 pN·s/μm and γ_{int} = 0. All other parameters as in Table 4.1. (Dashed line) Hard core model, Eq. 4.7, truncated at $x_{recoil} = N_{tot}d_{sarc}$. (Thin solid line) Recoil curve with γ_{ext} = 0, fit for best corresponding internal drag, γ_{int} = 338 pN·s/μm. (Inset) Log-log plot showing experimental recoil distance[44] (solid circles) and predicted $t^{1/2}$ law (solid line).

The results in Fig. 4.4 demonstrate the following: (1) With the parameters of Table 4.1, model predictions are in excellent agreement with experiment. (2) Results for the hard core and exact discrete models are almost indistinguishable, showing that the continuous limit and hard core approximation to the force-length relation accurately describe stress fiber severing. (3) Linear and nonlinear force-velocity relations yield similar results, both indicating that myosin dominates internal dissipation. Thus, hereafter we consider only the linear force-velocity relation.

An important prediction of the hard-core model is that for intermediate times (before complete fiber collapse), severed end displacement follows a one-half power law, $x_{recoil} \sim t^{1/2}$ (see

Eq. 4.7 for $t >> \tau_{coll}^{0}$). The measured recoil profile is in rather close agreement with this prediction (Fig. 4.4, inset). In the next section, we will show that this power law results directly from external drag.

External Drag Results in Nonuniform Sarcomere Length Profile and a Collapsed Cap

The state of the severed stress fiber at any instant is specified by the lengths of all sarcomeres. Model predictions were presented above. Using Table 4.1 parameter values, their main features can be summarized as (1) Immediately after severing, the sarcomere at the severed end contracts at rate v_{sarc} = 0.45 μm/s and collapses after $\tau_{coll} \approx 0.62$ s. (2) Thereafter a cap of $N_{cap}(t)$ collapsed sarcomeres grows at the severed end as successive sarcomeres collapse (Fig. 4.5). The cap growth law predicted by the hard-core model (Eq. 4.6) agrees closely with that of the exact discrete model (Fig. 4.5, inset). (3) After collapse of the first sarcomere, noncollapsed sarcomeres attain a steady-state exponential length profile of width $\xi \approx 2.5$ (Eq. 4.5). This is evident in Fig. 4.6, where a collapsed cap grows, ahead of which only ~ξ sarcomeres have significantly contracted at any instant. Continuous hard-core and discrete model profiles are in good agreement. (4) Complete fiber collapse occurs after $T_{coll} \approx 5.2$ s (cap engulfs entire fiber). (5) Before total fiber collapse, cap growth follows a one-half power law, $N_{cap} \sim t^{1/2}$.

In summary, the severed stress fiber comprises three zones (see Fig. 4.6): a collapsed portion near the severed end; a contracting zone of ~ξ partially collapsed sarcomeres; and an undisturbed portion near the adhesion. The origin of this highly nonuniform profile is drag force exerted on the recoiling fiber by its surroundings, which causes nonuniform sarcomere contraction velocities (Eq. 4.4). Were drag force absent, every sarcomere would experience the

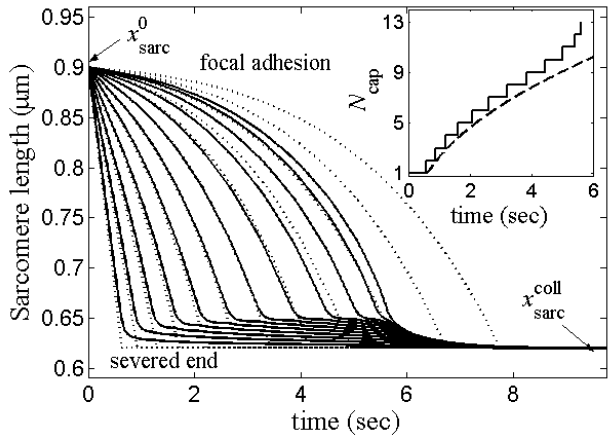

Figure 4.5: Sequential sarcomere collapse. Numerical (solid lines, Eq. 4.1) and hard core model (dotted lines, Eq. 4.4) solutions for sarcomere length evolution using parameters from Table 4.1. (Inset) Numerical (solid line, Eq. 4.1) and hard core model (dashed line, Eq. 4.6) solutions for collapsed cap growth. For numerical solution, a sarcomere was defined as collapsed when $x_{sarc} < x^*_{sarc}$.

same forces: the myosin contractile force f_s would be resisted only by internal friction (γ_{int} + γ_{myo}) v^0_{sarc}, where the effective myosin drag coefficient γ_{myo} is the slope of the myosin force-velocity relation. Equating forces, all sarcomeres would contract with the same velocity $v^0_{sarc} \approx f_s/(\gamma_{myo} + \gamma_{int})$ and collapse in the same time $\tau^0_{coll} = d_{sarc}/v^0_{sarc}$. The sarcomere profile would be uniform at all times. We find that this zero external drag scenario is inconsistent with the measured recoil profile: setting $\gamma_{ext} = 0$, the model predicts almost constant recoil velocity (see Fig. 4.4, thin solid line) in clear contradiction to the pronounced curvature of the observed profile.

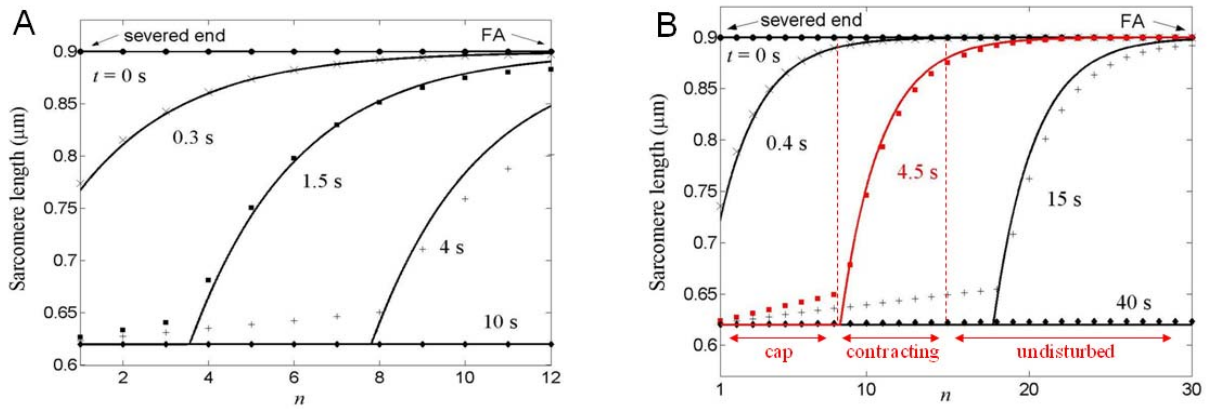

Figure 4.6: Evolution of the sarcomere length profile. Evolution of sarcomere length profile according to numerical solutions (Eq. 4.1, symbols) and hard core model (Eq. 4.5, solid lines) for fibers of N_{tot} = 12 (A) and N_{tot} = 30 (B) sarcomeres. Other parameters from Table 4.1. Three regions of differing sarcomere contractile activity are indicated for the N_{tot} = 30 fiber 4.5 s after severing (red).

Effect of external drag: scaling arguments

How does external drag modify the drag-free scenario? What is the origin of the predicted $t^{1/2}$ laws for recoil and cap length at intermediate times (Eqs. 4.7 and 4.6)? Consider the following simple scaling arguments. Central to the discussion is the velocity penetration length ξ (Eq. 4.4), the width of the contracting zone: only these $\sim\xi$ sarcomeres have substantial contraction velocity v_{sarc}. Note that the larger the external drag, the smaller this penetration depth. (1) *Early transient*. Consider the sarcomere at the severed end. Immediately after severing, it feels the forces discussed previously, but now an additional external drag $\gamma_{\mathrm{ext}}v$ resists contraction. Its velocity relative to the surroundings is $v \approx \xi v_{\mathrm{sarc}}$ since $\sim\xi$ sarcomeres are contracting. Balancing forces now gives contraction velocity $v_{\mathrm{sarc}} = v_{\mathrm{sarc}}^0/(1 + 1/\xi)$ and collapse time $\tau_{\mathrm{coll}} = \tau_{\mathrm{coll}}^0(1 + 1/\xi)$. External drag prolongs collapse by the factor $1 + 1/\xi \approx 1.4$. (2) *Steady state*. At large times, resistance to contraction of the first uncollapsed sarcomere is dominated by the large drag force $\approx N_{\mathrm{cap}}\gamma_{\mathrm{ext}}v_{\mathrm{recoil}}$ acting on the cap moving with velocity $v_{\mathrm{recoil}} = dx_{\mathrm{recoil}}/dt$. Note its total drag is proportional to cap size N_{cap}. Equating this to the myosin contraction force f_s yields $v_{\mathrm{recoil}} \approx v_{\mathrm{sarc}}^0 \xi^2/N_{\mathrm{cap}}$. Now the cap growth rate $dN_{\mathrm{cap}}/dt \approx v_{\mathrm{sarc}}/\delta x_{\mathrm{sarc}}$ is proportional to $v_{\mathrm{sarc}} \approx v_{\mathrm{recoil}}/\xi$, the sarcomere shrinkage rate in the contracting zone across which velocity falls to zero from the value v_{recoil} at the cap. Here $\delta x_{\mathrm{sarc}} \approx d_{\mathrm{sarc}}/\xi$ is the length of the first uncollapsed sarcomere relative to the collapsed length (the remaining slack). Across the contracting zone, the slack changes from zero at the cap to d_{sarc} at the edge of the unaffected zone. Hence, the cap dynamics are $dN_{\mathrm{cap}}/dt \approx \xi^2/(\tau_{\mathrm{coll}}^0 N_{\mathrm{cap}})$ with solution

$$N_{\mathrm{cap}} = \xi\left(2t/\tau_{\mathrm{coll}}^0\right)^{1/2}, \quad x_{\mathrm{recoil}} = N_{\mathrm{cap}}d_{\mathrm{sarc}} \qquad \left(t >> \tau_{\mathrm{coll}}^0\right) \tag{4.8}$$

These are precisely the results predicted by the hard core model for large times (Eqs. 4.6 and 4.7). The arguments reveal that for such times the experimentally observed recoil distance is simply the total cap length. Thus, recoil distance and cap size are fundamentally related. The experimental data are consistent with this $t^{1/2}$ recoil law (Fig. 4.4, inset).

External Drag Prolongs Relaxation of Force on Focal Adhesions

Focal adhesions play important roles in a cell's mechanical communication with its environment and can respond to applied force.[82,132] Immediately after severing, the tension vanishes at the severed stress fiber ends and thus the force exerted by the severed fiber on its anchoring adhesions will eventually decay to zero. We used our model to calculate this decay (Fig. 4.7). The predicted decay time equals the end recoil relaxation time ($T_{\mathrm{coll}} \approx 5.2$ s) since the total external drag on the retracting fiber is communicated to the adhesion. Finite decay time of the force is entirely due to external drag: without drag, decay would be instantaneous, since the vanishing tension is the same throughout the fiber.

Kumar et al. used traction force microscopy to measure total cellular traction reduction after severing a stress fiber. This includes contributions from all focal adhesions.[44] Although focal adhesions were not visualized and single adhesion forces not measured, consistent with our model's predictions, substrate relaxation near the intact stress fiber end (where an adhesion is expected to reside) appeared to occur on a timescale similar to that of fiber recoil.

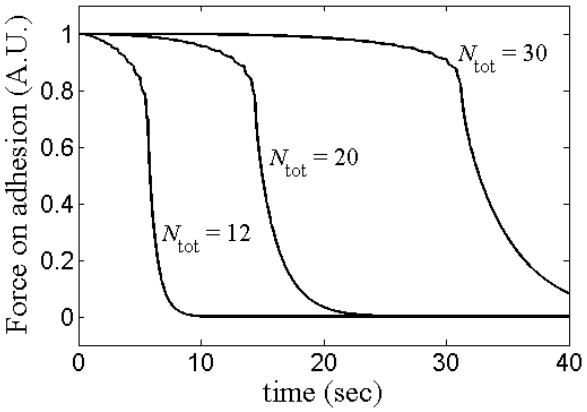

Figure 4.7: Force exerted by a severed stress fiber on its anchoring adhesion
Model predictions for fibers of three lengths as indicated. All other parameters from Table 4.1. Force profiles are numerical solutions of Eq. 4.1 for force exerted on the actin bundle connected to the adhesion ($n = N_{tot} + 1$). Note that the total force on the adhesion may have contributions from other attached stress fibers.

VI. Discussion

We developed a model of stress fibers starting from the experimentally established organization of actin, myosin, and other components. The model was applied to fiber kinetics after severing. Comparing model predictions to a recent experimental severing study enabled us to test contraction mechanisms and to quantitatively infer fundamental stress fiber properties.

Force-length relation

As for muscle, a fundamental property is the single sarcomere force-length relation. We find the profile is similar to that of muscle (Fig. 4.2A) in that there are two distinct regions on the ascending limb (Fig. 4.2B): (1) *Shallow region*. At normal operating lengths, resistance to length change is weak. The long sarcomere relaxation times observed in Peterson et al.[41] imply a small force constant similar to that of muscle titin,[102] k_2 = 4.0 pN/μm per minifilament. This suggests the shallow region originates in tensile stress due to c-titin,[91] consistent with evidence of elastic contribution to stress fiber stress,[133,134] although apparently inconsistent with other observations.[44] This remains an important question to resolve by future experiment. (2) *Steep region*. In the severing experiments of Kumar et al.,[44] after sarcomeres contracted, total

estimated distance d_{sarc} = 0.28 μm compressive elastic forces suddenly built up and stalled the myosin contractile force, f_s = 17 pN per minifilament. We found that the corresponding force constant at these small lengths is much greater than in the shallow region, and we used the value from muscle, k_1 = 500 pN/μm. These forces presumably originate from interference of overlapping actin filaments within myosin regions and from myosin-myosin interference between adjacent sarcomeres. Note the steep ascending region in muscle (Fig. 4.2A) likely also has its origin in compressive elastic forces.[109]

The experimental data currently available is not consistent with a simple constant slope relation. Severing experiments dictate that the single force constant value would be $k \approx f_s/d_{sarc} \approx$ 60 pN/μm per minifilament. Although this model can fit the severing data well (it is mathematically equivalent to a viscoelastic cable[44]), it cannot explain the slow relaxation seen in Peterson et al.[41]

Assuming each sarcomere contains n_{mini} = 50 minifilaments in parallel and is w = 0.5 μm wide (see Table 4.1), the total sarcomere force constant is $n_{mini}k_2$ = 200 pN/μm at normal operating lengths. This implies an effective modulus ~10^3 pN/μm^2, considerably less than the value ~10^5-10^6 pN/μm^2 reported by Deguchi et al. for isolated stress fibers.[134] The mechanical properties of these latter fibers may have been altered by isolation and the absence of ATP. Future mechanical studies in living cells may resolve this discrepancy.

External drag force

We find that substantial external drag forces must be invoked to explain the curvature in the experimental recoil profile (see Fig. 4.4). Our model leads to drag coefficient $\gamma_{ext} \approx$ 5.3 pN·s/μm per minifilament. Now the total drag coefficient of a cylindrical sarcomere of length

x^0_{sarc} = 0.9 μm in a medium with viscosity η_{cyt} is $n_{mini}\gamma_{ext} = 2\pi\eta_{cyt}\, x^0_{sarc}/(\ln x^0_{sarc}/w + 0.25)$.[135] Our model then implies effective cytosolic viscosity $\eta_{cyt} \approx 39$ Pa·s, or ~10^4 times the viscosity of water. Thus, severed fiber recoil kinetics contain information about how the stress fiber interacts with its surroundings in the cell. Indeed, the recoiling stress fiber is an internal probe of effective cellular viscosity. Our result is similar in magnitude to that from the microrheological study of fibroblasts by Tseng et al., who measured an effective cytosolic viscosity of 10 Pa·s at frequency 0.16 s^{-1}.[136] Other studies of macrophages have reported apparent viscosities in the range 10^2-10^3 Pa·s.[137,138] Variations in reported values are expected, since viscosity depends on the time- and length-scale probed, reflecting structural heterogeneity and the complex nonlinear viscoelastic response of living cells.

The effective cytosolic viscous drag may originate not only from nonspecific interactions with the cytosol but also from breaking of dynamic cross links between the stress fiber and its surroundings. Extracellular matrix proteins are concentrated along stress fibers, indicating possible interactions between stress fibers and transmembrane proteins,[139] and electron microscopy reveals connections between stress fibers and the surrounding cytoskeleton.[140] Indeed, buckled stress fibers exhibit 2 μm wavelength undulations, possibly suggesting lateral connections.[133]

Internal drag force

From the model, we conclude that most internal dissipation is due to myosin: fitting to the experimental recoil data, we found internal drag coefficient γ_{int} = 5.0 pN·s/μm, smaller than the myosin force-velocity slope at stall, γ_{myo}, which represents an effective myosin internal drag coefficient. The nonmyosin component may derive from friction between overlapping F-actin in

the myosin zones at sarcomere centers or displacement of dynamic α-actinin cross links by myosin which, unlike striated muscle, must accompany sarcomere shrinkage. Another possibility, investigated by Stachowiak and O'Shaughnessy (Chapter 3),[86] is that when sarcomeres change length, actin filaments adjust via polymerization or depolymerization. Applying this framework to severing kinetics, filaments would shrink during recoil (as in contractile ring constriction) and γ_{int} would represent an effective polymerization-derived value.[86] Following a perturbation, this model (Chapter 3)[86] identified an additional early transient with a smaller γ_{int} value; this picture could thus explain curvature in the end recoil profile, and would then lead to an external drag coefficient smaller than the value implied by the present model assuming fixed actin lengths. Future severing experiments studying stress fibers of different lengths can distinguish between these two pictures, since the two models predict very different length-dependencies.

Effect of myosin inhibition

Kumar et al. severed stress fibers after reducing myosin phosphorylation levels by treatment with inhibitors of the kinases ROCK and MLCK.[44] Recoil was diminished by 60% 17 s after severing (ROCK inhibition) and by 92% 8.5 s after severing (MLCK inhibition). To model these experiments, we set myosin stall force to zero ($f_s = 0$). We found that the recoil rate was retarded, with 60% recoil loss after 8.5 s and 34% loss after 17 s, but the eventual total recoil distance was virtually unchanged due to weak passive elastic forces (see Fig. 4.8). This agrees with previous studies indicating a passive elastic contribution to contraction in the absence of ATP.[134] However, the predicted recoil rate exceeds that measured by Kumar et al.,[44] which may be explained by disruption of stress fiber structure due to compromised minifilament formation

when myosin phosphorylation is inhibited.[94] It would be interesting to sever stress fibers treated with blebbistatin, which inhibits myosin force-generation but not phosphorylation.[141]

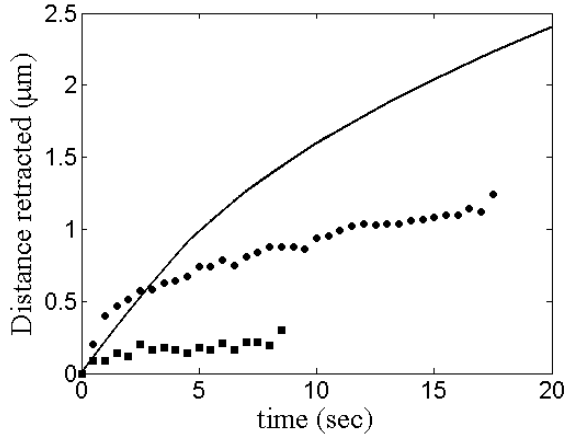

Figure 4.8: Effect of inhibition of myosin phosphorylation on stress fiber recoil.
Circles: ROCK inhibition, from Kumar et al.[44] Squares: MLCK inhibition, from Kumar et al.[44] Solid line: Model prediction with myosin stall force f_s = 0. Numerical solution of Eq. 4.1, all other parameters from Table 4.1.

Relaxation of cellular traction

Our model predicts that after severing, the force exerted by the severed stress fiber on its adhesion decays to zero over the recoil timescale, T_{coll} = 5.2 s (Fig. 4.7). Using traction force microscopy, Kumar et al. measured a loss of >50% of the cell's total traction over 30 s after severing a single stress fiber.[44] This large drop suggests tension loss in one fiber precipitates on longer timescales tension loss elsewhere in the cytoskeletal network by physical or biochemical mechanisms beyond the scope of our single fiber model. Over yet longer timescales of minutes, loss of force applied on focal adhesions causes adhesion disassembly[82,132] by increasing the off-rate of a mechanosensitive component.[132]

Experimentally testable predictions

The model makes numerous quantitative predictions that can be tested by future

experiments: (1) Sarcomere length profiles. External drag leads to dramatically inhomogeneous stress fiber collapse kinetics after severing, since contraction of a given sarcomere is opposed by the net drag on the entire fiber section between it and the severed end. Thus, more interior sarcomeres contract more slowly. We predict a sarcomere profile with three zones (see Fig. 4.6) including a cap of collapsed sarcomeres at the severed end. The predicted sarcomere length profiles (Eq. 4.5 and Fig. 4.6) could be directly measured by labeling a periodic stress fiber component (e.g., myosin-II or α-actinin). (2) Fiber length dependence. We compared our model to a single experimental recoil profile for a severed fiber containing N_{tot} = 12 sarcomeres. Experiments following severed stress fibers of different lengths could test our prediction that total fiber collapse time-scales as N_{tot}^2, another consequence of external drag. Were external drag absent, collapse time would be independent of fiber length. (3) Sarcomere length dependence. Assuming a sarcomere's external drag coefficient is proportional to its length (for example, there may be a constant number of connections with the surroundings per unit length), our model predicts that stress fibers with initially longer sarcomeres recoil more slowly and total collapse time-scales linearly with sarcomere length, $T_{\mathrm{coll}} \sim x_{\mathrm{sarc}}^0$ (see Fig. 4.9). (4) End recoil and collapsed cap: power law time dependencies. We predict that end recoil distance and collapsed cap length grow as power laws in time: $x_{\mathrm{recoil}} \sim N_{\mathrm{cap}} \sim t^{1/2}$ (see Eq. 4.8), consistent with current end recoil data (Fig. 4.4, inset). Severing longer stress fibers, where the power law window is larger, would more stringently test the end recoil law. (5) Forces on focal adhesions. The predicted adhesion force decay after severing (Fig. 4.7) could be directly measured using techniques measuring forces on focal adhesions.[82] For adhesions attached to just a single stress fiber, we predict the decay time increases with stress fiber length as $\sim N_{\mathrm{tot}}^2$. This may also describe the short time decay for adhesions attached to multiple stress fibers. (6) Modifying

fiber-cell coupling. An interesting possibility is to sever stress fibers in cells where candidate linker proteins between stress fibers and their surroundings are interfered with. In our model this would modify the external drag coefficient γ_{ext}. Comparing with model predictions may thus help identify such proteins.

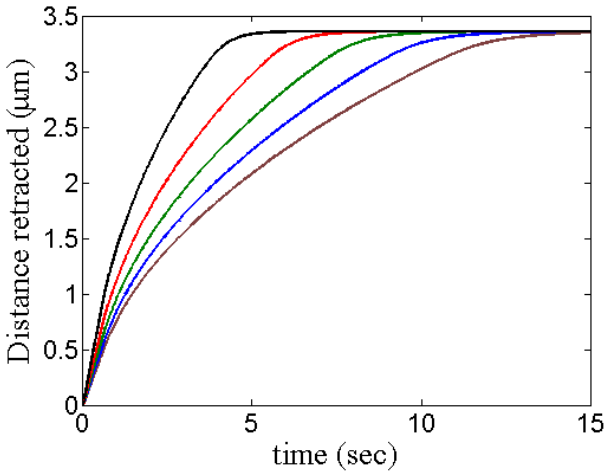

Figure 4.9: Predicted recoil of severed stress fibers with different initial sarcomere lengths. Initial sarcomere lengths x_{sarc}^0 = 0.6 μm (black), 0.9 μm (red), 1.2 μm (green), 1.5 μm (blue) and 1.8 μm (brown). The external drag coefficient was assumed proportional to sarcomere length ($\gamma_{ext} \sim x_{sarc}^0$), with γ_{ext} = 5:3 pN·s/μm when x_{sarc}^0 = 0.9 μm. All other parameters from Table 4.1. Numerical solutions of Eq. 4.1.

Appendix A: Equation for the Velocity Profile

The hard core model assumes a linear myosin force-velocity relation and approximates the shallow (steep) portion of the force-length relation (Fig. 4.2B), as flat (infinitely steep). Thus contraction is stalled in collapsed sarcomeres ($n < N_{cap}$), whereas for active sarcomeres, $F_{elast}(x_{sarc}) \rightarrow 0$. The myosin force terms are expressed as $F_{myo}(v_{sarc}) = \tilde{f}_s - \gamma_{myo} v_{sarc}$, where $\tilde{f}_s = f_s + k_2 x_{sarc}^0$ is the effective stall force including the elastic contribution at the initial sarcomere length (see Fig. 4.2B). Thus, the fiber dynamics (Eq. 4.1) for active sarcomeres ($n \geq N_{cap}$) simplify to

$$\gamma_{ext} v_n = (\gamma_{myo} + \gamma_{int})(v_{n-1} - v_n) - (\gamma_{myo} + \gamma_{int})(v_n - v_{n+1}) \qquad (4.9)$$

Note that the slope of the force-velocity relation γ_{myo} emerges as a contribution to the total internal drag coefficient. The continuous limit then yields Eq. 4.2. Strictly, this limit is valid provided $\xi >> 1$. In practice, we find that even for our best-fit value $\xi \approx 2.5$, it provides an excellent approximation.

Appendix B: Equations and Solutions for the Sarcomere Profile and Collapsed Cap Length

It is convenient to express the sarcomere lengths as functions of N_{cap} in favor of time, $x_{sarc}(n,t) \rightarrow x_{sarc}(n,N_{cap})$ (time-dependence is recovered later using the cap solution $N_{cap}(t)$). Then the sarcomere shrinkage velocity can be written $v_{sarc}(n) = -(\partial x_{sarc}/\partial N_{cap})(dN_{cap}/dt)$. Meanwhile, in the continuous limit, the cap growth rate is the product of the sarcomere contraction velocity and length gradient at the cap front, $dN_{cap}/dt = \theta^{-1} v_{sarc}(N_{cap})$, where $\theta \equiv \partial x_{sarc}=\partial n|_{n = Ncap}$. These expressions give the cap and sarcomere dynamics (Eq. 4.3).

Using the explicit solution for the sarcomere velocity profile (Eq. 4.4) and changing variables $x_{sarc}(n, N_{cap}) \rightarrow \tilde{x}_{sarc}(w,N_{cap})$, where $w = n - N_{cap}$ is the sarcomere location relative to the collapsed cap, the sarcomere length dynamics in Eq. 4.3 become

$$\frac{\partial \tilde{x}_{sarc}}{\partial w} - \frac{\partial \tilde{x}_{sarc}}{\partial N_{cap}} = e^{-w/\xi} \left. \frac{\partial \tilde{x}_{sarc}}{\partial w} \right|_{w=0} . \tag{4.10}$$

The boundary conditions are (1) The sarcomere at the cap boundary ($w = 0$) is collapsed, $x_{sarc} = x_{sarc}^{coll} \equiv x_{sarc}^{0} - d_{sarc}$; and (2) Far from the severed end, sarcomeres are undisturbed, $x_{sarc} = x_{sarc}^{0}$ for $w \rightarrow \infty$. The steady state solution, $\partial \tilde{x}_{sarc}/\partial N_{cap} = 0$, is the exponential profile of Eq. 4.5. The

profile, depending only on w, has constant shape and propagates inward at the same speed as the collapsed cap front.

Chapter 5

Coupling of Contraction and Actin Disassembly in Spontaneously Severing Stress Fibers

In Chapter 3, we developed a model of stress fibers including coupling between actin turnover and contractile forces. In Chapter 4, we developed a model of severed stress fiber recoil. In both cases, only a single experimental measurement was available for comparison with the models. In order to more accurately estimate parameters and compare alternative models a much larger dataset was needed. To this end, we collaborated with Dr. Mary Beckerle's laboratory at the University of Utah. Using time-lapse confocal imaging of living cells, the Beckerle lab observed spontaneous severing and recoil of stress fibers. Dr. Mark Smith, Elizabeth Blankman, and Laura Luettjohann of the University of Utah performed the imaging, while we performed the quantitative image analysis and mathematical modeling. We used quantitative image analysis to simultaneously measure the fiber length and the relative amount of fluorescently labeled actin and other components during recoil of spontaneously severed stress fibers. In this chapter, we present the results of this analysis and extend the model of Chapter 3 to the case of stress fiber severing. Our results show that actin turnover and contraction are coupled, as predicted by the model.

I. Introduction

Actomyosin structures in nonmuscle cells undergo continuous turnover while simultaneously generating tension and changing shape. To coordinate these processes, the

assembly and disassembly kinetics of cytoskeletal filaments are coupled to mechanical force. For example, increasing myosin-II activity in epithelial cells increases the actin turnover rate in the cytokinetic ring,[142] consistent with myosin-induced actin disassembly observed in vitro.[143] Indeed, actin and microtubule subunit on and off rates are directly related to the forces exerted on cytoskeletal filament ends[116,144] This principle is used during cell migration when actin polymerization at actin filament barbed ends generates forces to push plasma membrane at the leading edge forward,[145,146] and during mitosis when polymerization and depolymerization of microtubules generate forces to move chromosomes.[147] Consequently, understanding how the cytoskeleton behaves in mechanically dynamic environments requires understanding how turnover and mechanical forces are coupled.

Stress fibers are linear, tensile bundles composed of actin filaments and nonmuscle myosin-II minifilaments[93] that terminate in transmembrane focal adhesions, allowing transmission of contractile forces to the extracellular matrix.[148] In vivo, stress fibers generate contractile forces in myofibroblasts to provoke tissue reorganization during wound healing[5] and resist shear forces from blood flow in vascular endothelial cells.[34] Many stress fibers have a sarcomeric structure similar to striated muscle, albeit more disordered, with alternating actin filament polarity,[149] alternating localization of myosin-II and the actin filament crosslinking protein α-actinin,[41] and a nonmuscle isoform of the giant elastic protein titin.[91] Fluorescence recovery after photobleaching (FRAP) experiments showed that unlike striated muscle, stress fibers are highly dynamic, with α-actinin turning over in $t_{1/2}$ = 15 s, myosin light chain in 1 min, and actin in 3 min.[43] Actin turnover may occur by a treadmilling mechanism, as microinjected fluorescent actin subunits incorporated into the α-actinin puncta[103] where actin filament barbed ends are expected to reside in a sarcomeric structure.

Stress fibers sense and respond to mechanical signals. Polymerization of actin at stress fiber ends anchored in focal adhesions requires tension generated by myosin-II induced contraction.[150] Another pathway for mechanosensing involves the LIM protein zyxin. Cyclic stretching of stress fibers caused fiber thickening that depends on recruitment of zyxin.[88] Moreover, elevated stress fiber tension causes acute elongation and thinning events which are repaired after the recruitment of zyxin, α-actinin, and VASP, which restore the fiber's mechanical integrity by promoting actin assembly.[151] However, the mechanisms of coupling between mechanical force and actin turnover have not been elucidated.

Severing of stress fibers using laser ablation or mechanical means and observing the recoil has been a useful tool to study stress fibers.[44,152-155] Mathematical models of stress fiber recoil after severing have illuminated various aspects of stress fiber mechanics, such as the presence of elastic or viscous forces between the stress fiber and its surroundings (see Chapter 4),[126,152] or the influence of fluctuating sarcomere lengths.[153] However, these models did not take into account actin turnover. Another technique used to investigate stress fibers was treatment with the phosphatase inhibitor calyculin A, which caused peripheral stress fiber sarcomeres to contract while central sarcomeres elongated.[41] Since the sarcomere relaxation time was similar to the actin turnover time (~5 min), a mathematical model proposed a coupling between actin turnover and mechanics (see Chapter 3).[86] Sarcomere contraction was proposed to cause compressive stresses to build up between actin filaments as their overlap and density increase in the center of the sarcomere. These stresses were proposed to increase the actin disassembly rate, providing a means to regulate actin filament length. However, actin remodeling has never been directly measured during stress fiber contraction.

Here, we combine quantitative time-lapse imaging and image analysis with mathematical modeling to show that contraction and actin disassembly are coupled in stress fibers. We observe that stress fibers spontaneously sever and recoil, allowing analysis of stress fiber contraction without perturbation by laser severing or drug treatment. During recoil, stress fibers shorten by ~80% while shedding ~50% of their actin. The actin disassembly is delayed relative to recoil, causing the actin density to initially increase during recoil, then peak and decay when recoil is complete. We applied a version of our previous mathematical model of stress fibers that includes mechanosensitive actin disassembly (Chapter 3) to the case of spontaneous severing and recoil.[86] The model predictions agree with our experimental data, and show that actin disassembly is caused by depolymerization induced by myosin contractile forces. Actin filaments are predicted to shorten or lengthen in response to sarcomere contraction and expansion, respectively, endowing stress fiber sarcomeres with a wide range of stable operating lengths. Thus, we identify a mechanism by which coupling between mechanical forces and actin turnover allows stress fibers to dynamically respond to changing conditions in the cell.

II. Experimental Results

Failure of the stress fiber repair mechanism leads to spontaneous severing and recoil

To investigate the mechanisms of stress fiber contraction and remodeling, we performed time lapse imaging of mouse fibroblasts expressing actin-mCherry or actin-Apple. This revealed spontaneous, catastrophic breakage of stress fibers occurring at frequency 0.03 ± 0.01 events/min/cell (n = 83 cells, 1100 min of observation), as reported previously (Fig. 5.1A).[151] Following breakage, the newly severed ends retract and the two resulting stress fiber segments shorten until they reach a final steady length (Fig. 5.1B). These spontaneous severing events

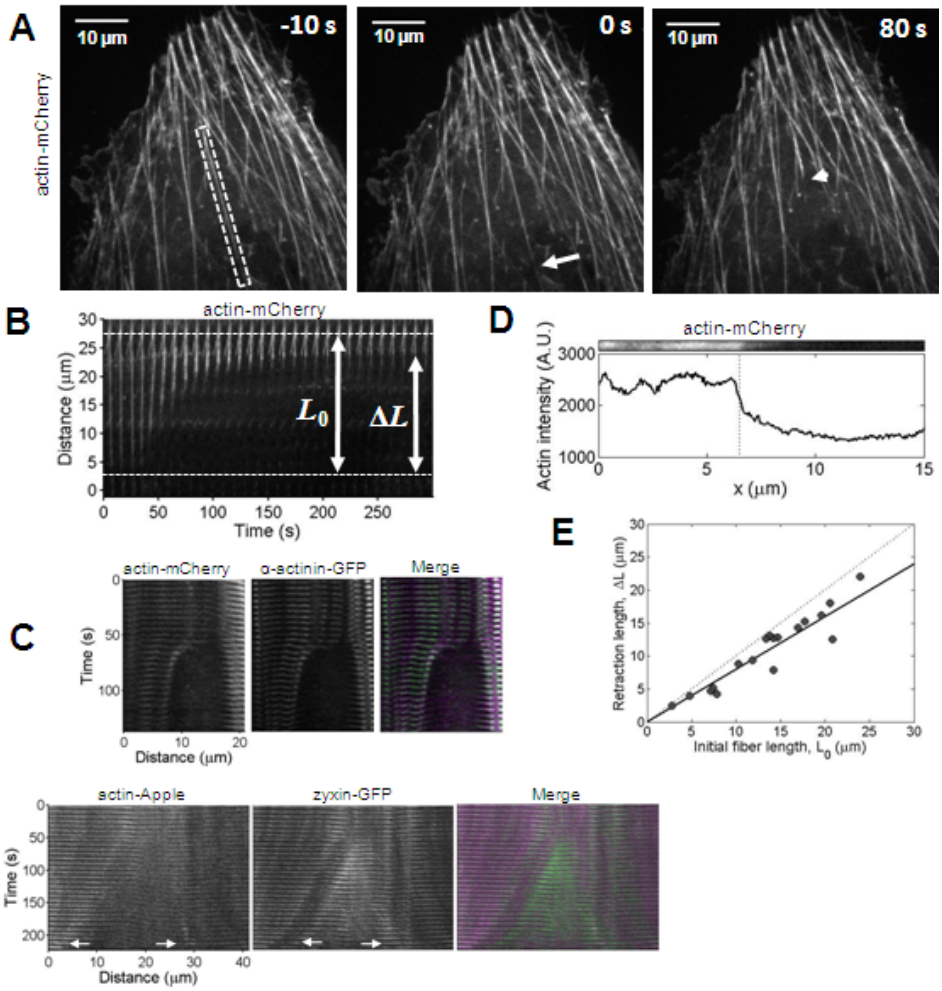

Figure 5.1: Stress fibers spontaneously fracture and recoil a constant fraction of their original length

(A) Time lapse confocal images of a spontaneously severing stress fiber in a mouse fibroblast expressing actin-mCherry. Arrow: location of the break in the fiber; arrowhead: severed end after the completion of recoil. t = 0 corresponds to the time of severing.

(B) Actin-mCherry kymograph of the spontaneously severing stress fiber highlighted in (A), indicating the initial fiber length (L_0) and the retraction length (ΔL). Dotted lines indicate the intact end of the fiber (top) and the position of the break (bottom).

(C) Kymographs showing spontaneous stress fiber severing in the absence and presence of repair protein recruitment. (Top) No α-actinin-GFP is recruited to the elongation site of this severing fiber, indicating a lack of recruitment of repair proteins. (Bottom) A stress fiber breaks and recoils after recruitment of zyxin-GFP to the site of elongation, indicating a failure of the stress fiber repair process. Arrows indicate the severed ends (bottom).

(D) Actin-mCherry intensity profile along a recoiling stress fiber. The dotted line indicates the severed end position, defined to be the location of the minimum of $\partial I/\partial x$, where I is the actin signal.

(E) Retraction length as a function of initial stress fiber length (n = 18). Solid line: best fit line, $\Delta L = 0.8L_0$. Dotted line: $\Delta L = L_0$.

All micrographs from the Beckerle lab (University of Utah).

allowed us to study stress fiber contraction and remodeling without artificial perturbations such as drug treatment or laser ablation.[41,44]

Spontaneous severing is preceded by elongation and thinning of a localized region of the stress fiber, lasting 10-60 s.[151] 82% of elongating sites are stabilized and repaired after recruitment of the LIM protein zyxin, actin filament crosslinking protein α-actinin, and actin barbed end binding protein VASP to the elongation site, while 18% proceed to breakage.[151] Time lapse imaging of cells expressing zyxin-GFP or α-actinin-GFP revealed that in some severing stress fibers no repair proteins are recruited to the elongation site (n = 4) while in others zyxin and α-actinin are recruited before breakage (n = 8, Fig. 5.1C). Thus, spontaneous severing occurs both without recruitment of repair proteins and after the failure of repair proteins to stabilize an elongating stress fiber.

Spontaneously severed stress fibers contract uniformly and lack significant mechanical coupling to the surrounding cytoskeleton

Analysis of severed stress fiber recoil can reveal whether stress fibers are mechanically coupled to the surrounding cytoskeleton via elastic or viscous crosslinks.[126,152] To characterize spontaneously severed stress fibers, we tracked the length of spontaneously severed stress fibers as a function of time by measuring from the intact end (anchored to a focal adhesion or another stress fiber) to the severed end, whose position was defined as the position of the maximum fall-off of actin signal along the fiber axis (Fig. 5.1D). Plotting the retraction length (ΔL) as a function of initial stress fiber length (L_0) revealed a direct proportionality, with fibers of lengths up to ~25 μm all shortening by 80 ± 3% during recoil (mean ± SEM, n = 18, Fig. 5.1B,E). This result contrasts with previous measurements of laser-severed stress fibers, whose retraction

length plateaued at ~6 μm and ~8 μm in epithelial cells and fibroblasts, respectively.[152] This plateau was proposed to be caused by elastic coupling between the stress fiber and its surroundings,[152] the compliance of which defines a maximum severed end displacement that can be induced by the fiber's tension. Thus, our analysis shows that spontaneously severed stress fibers are not elastically coupled to their surroundings.

We measured the duration of recoil by fitting a decaying exponential function to each stress fiber's length evolution curve and extracting the time scale (Fig. 5.2A). The recoil duration clustered between 15 and 30 s and was independent of the initial stress fiber length, although 4 observed fibers took significantly longer giving a mean duration of $\tau = 48 \pm 13$ s (n = 18, Fig. 5.2B). We also tested whether shortening occurs uniformly along the stress fibers by measuring the initial contraction rates of fiber segments located between fiduciary marks identified in cells expressing α-actinin-GFP or zyxin-GFP (Fig. 5.2C). This revealed a nearly uniform rate of contraction along the stress fiber (Fig. 5.2D). A constant recoil duration and uniform contraction are hallmarks of contraction in the absence of drag forces between the stress fiber and its surroundings. Such drag forces would cause the recoil duration to increase with the square of the initial fiber length because longer fibers experience more drag forces (see Chapter 4).[126] Moreover, the contraction velocity would decay exponentially from the severed inward because myosins further into the fiber work against a larger total drag force (see Chapter 4).[126] Thus, spontaneously severed stress fibers are mechanically isolated from the surrounding cytoskeleton.

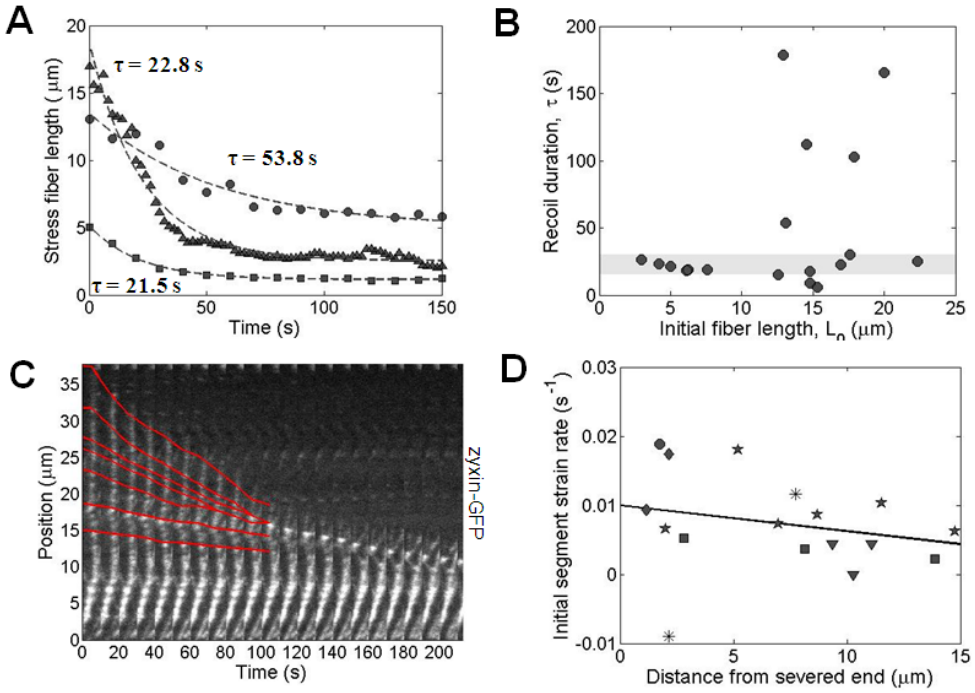

Figure 5.2: Recoil duration is independent of stress fiber length and contraction occurs uniformly along the fiber
(A) Stress fiber length as a function of time for three spontaneously severed stress fibers. Recoil duration τ was defined as the time scale of the best fit decaying exponential function, $L(t) = (L_0 - \Delta L) + \Delta L e^{-t/\tau}$ (dashed lines).
(B) Recoil duration as a function of initial stress fiber length (n = 18). Most stress fibers recoil in 15-30 s regardless of their initial length (gray band).
(C) Zyxin-GFP kymograph of a stress fiber undergoing recoil. Fiduciary marks (red lines) define the boundaries of stress fiber segments. Micrographs from the Beckerle lab (University of Utah).
(D) Initial contraction rate of stress fiber segments bounded by fiduciary marks as a function of distance from the severed end (n = 17). Contraction rates are expressed as strain rates after normalizing by the initial segment length. Different symbols indicate different stress fibers. The best fit line to all data points (solid line) has a slope that is not significantly different from 0 (p = 0.35).

Stress fibers lose half of their actin during recoil, but the linear actin density doubles

Because actin in stress fibers is dynamic and turns over in 3-5 min,[43,44] we hypothesized that actin remodeling could accompany the dramatic shortening of stress fibers that we observed after spontaneous severing (Fig. 5.1B,E). To test this, we compared the total intensity of fluorescently labeled actin in stress fibers at the time of severing and after recoil. This revealed that actin was shed during recoil as 51 ± 5% (n = 16) of the actin in the stress fiber was lost (Fig.

5.3A). Nevertheless, because the fraction of actin lost was less than the fractional shortening of the fiber (0.8, Fig. 5.1D), the linear actin density (total actin fluorescence divided by fiber length) increased by a factor of 1.9 ± 0.2 (n = 16) during recoil (Fig. 5.3B). Similar behavior was exhibited by the actin filament binding protein α-actinin and zyxin, which binds to α-actinin. 42 ± 7% (n = 10) and 66 ± 8% (n = 6) of the α-actinin and zyxin were lost during recoil, and their linear densities increased by factors of 2.0 ± 0.2 and 1.6 ± 0.3, respectively.

Striated muscles becomes thicker when their linear actin density increases during sarcomere shortening.[156] We hypothesized that stress fibers would also thicken during recoil because the linear actin density doubles. To measure the apparent stress fiber width, we calculated the full-width half-maximum of the best fit Gaussian functions to actin intensity profiles taken perpendicular to the stress fiber axis (Fig. 5.3D). This revealed that the apparent stress fiber width increases by 17 ± 5% (n = 12) during recoil (Fig. 5.3C,E), corresponding to an apparent increase in the fiber cross sectional area of ~35%. This is a lower bound for the increase in thickness because the point spread function makes fibers appear thicker than they actually are. Therefore, we conclude that actin and actin-associated proteins are shed from the stress fiber during contraction but their linear density increases, causing an increase in the fiber thickness.

Actin depolymerization is delayed relative to recoil, causing the actin density to rise, peak, and decay

We next sought to determine whether actin disassembly causes contraction or whether contraction causes actin disassembly. Comparisons of the time evolution of stress fiber shortening and actin fluorescence in the fiber revealed that actin disassembly lags recoil (Fig. 5.4A). We defined the delay of depolymerization to be the difference between the

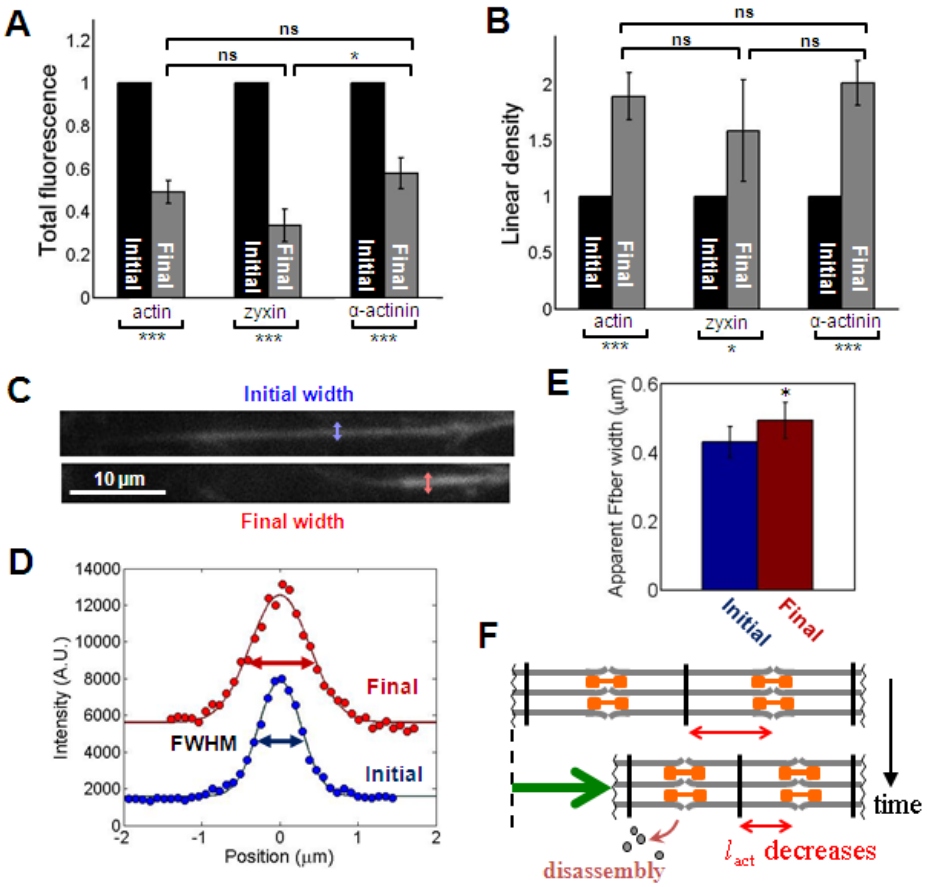

Figure 5.3: During recoil actin, α-actinin and zyxin are shed from the stress fiber while their densities increase
(A) Total fluorescence intensity of actin (n = 16), zyxin (n = 6), and α-actinin (n = 10) in stress fibers before and after recoil, normalized by the initial value.
(B) Linear density of actin (n = 16), zyxin (n = 6), and α-actinin (n = 10) in the stress fiber before and after recoil, normalized by the initial value.
(C) An actin-mCherry stress fiber just after severing and after recoil, with the stress fiber width indicated. Micrographs from the Beckerle lab (University of Utah).
(D) The apparent stress fiber width was determined by fitting Gaussian functions (solid lines) to measured actin intensity profiles perpendicular to the fiber axis (filled circles). The width was defined to be the full width at half max.
(E) The apparent stress fiber width increases by 17 ± 5% during recoil (n = 12).
(F) Schematic illustration of actin loss from a recoiling stress fiber.
Bar graphs show mean ± SEM.

depolymerization time scale (the time scale of the best fit decaying exponential function to the actin fluorescence curve) and the recoil duration (Fig. 5.2A), which revealed a depolymerization delay of 53 ± 23 s (n = 16) relative to recoil (Fig. 5.4B). This delay was evident in plots of the total actin fluorescence as a function of stress fiber length, which displayed a concave down

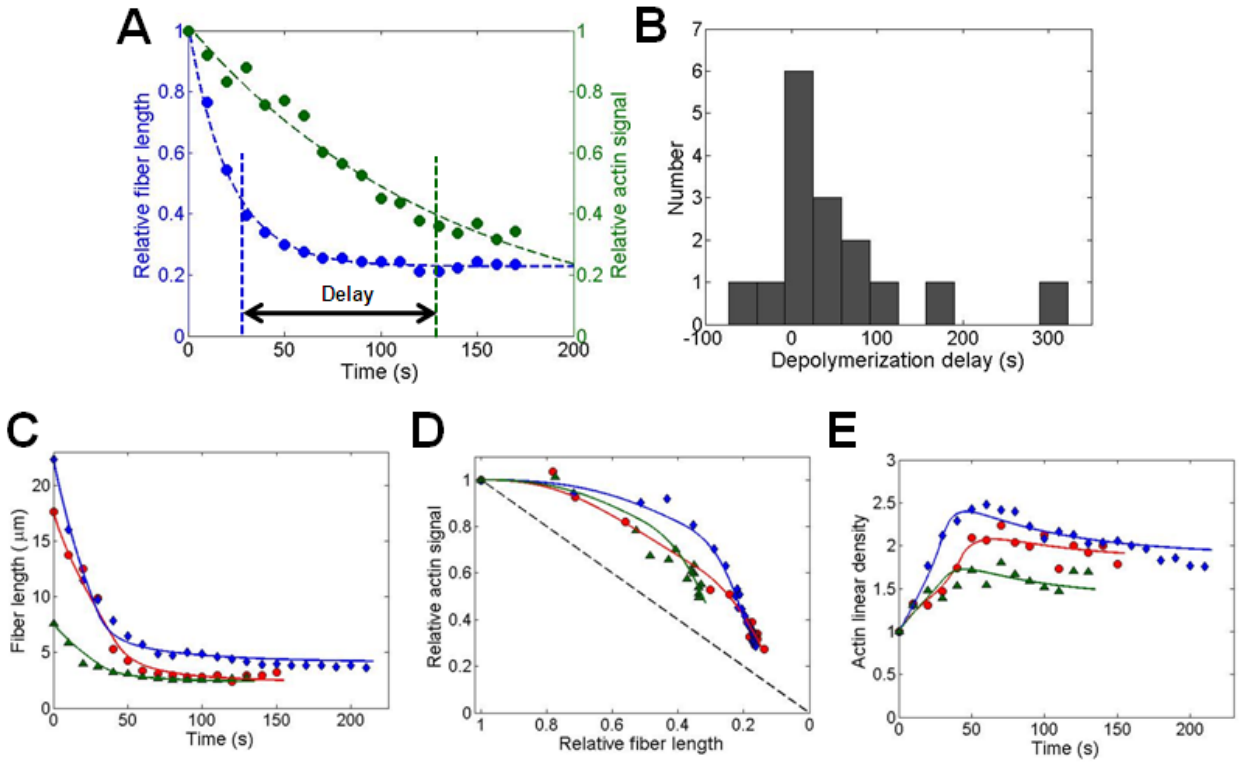

Figure 5.4: Actin depolymerization lags behind recoil, causing the actin density to peak and then decay

(A) Kinetics of recoil (blue) and the amount of actin (green) during the recoil of one stress fiber. Circles: measurements. Dashed lines: decaying exponential fits to extract the time scales. The depolymerization delay is defined as the difference between the actin depolymerization and recoil time scales.

(B) Histogram of depolymerization delay times (n = 16).

(C-E) Measured and model-predicted stress fiber length (C), total actin signal (D), and actin density (E) during recoil for 3 different stress fibers. Model curves were fit for the actin-actin elastic constant k, the sarcomere drag coefficient γ_{int}, and the minimum sarcomere length l_{min}. Blue diamonds: k = 17.8 pN/μm, γ_{int} = 463 pN·s/ μm, and l_{min} = 0.18 μm. Red circles: k = 29.5 pN/μm, γ_{int} = 587 pN·s/ μm, and l_{min} = 0.13 μm. Green triangles: k = 21.7 pN/μm, γ_{int} = 703 pN·s/ μm, and l_{min} = 0.3 μm. All other parameters, as in Table 5.1. In (D), the dashed line indicates the trajectory that would be followed if actin disassembled in proportion to recoil.

shape indicating that much of the actin depolymerization occurs after the stress fiber has stopped shortening (Fig. 5.4D). As a result, the actin density typically increases and reaches a peak value during recoil, followed by decay as depolymerization occurs at constant fiber length (Fig. 5.4E). The density then reaches a steady value higher than the original value (Fig. 5.3B and 5.4E). Thus, recoil of spontaneously severed fibers occurs faster than actin disassembly, causing the actin density to overshoot its final value, strongly suggesting that contraction drives actin disassembly.

Zyxin has no effect on actin disassembly during recoil

Zyxin is the key protein involved in stress fiber repair.[151] To test whether zyxin has a role in the remodeling of stress fibers after spontaneous severing, we observed stress fibers in fibroblasts derived from zyxin$^{-/-}$ mice[157] (Fig. 5.6C). The lack of zyxin did not significantly change the fractional shortening after severing, the recoil duration, nor the amount of actin disassembly compared to wild-type (Fig. 5.6F-H). Therefore, while zyxin has a key role in the repair process it does not appear to play a role in the recoil or actin remodeling of spontaneously severed stress fibers.

III. Model of Stress Fibers

To understand the mechanisms of stress fiber recoil and actin remodeling, we extended a previous model of stress fibers to allow for severing (Fig. 5.5A, see Chapter 3).[86] The model includes a mechanical force balance and actin turnover and therefore can be tested against our measurements of both recoil and actin remodeling. Parameter values are listed in Table 5.1.

Sarcomeric structure and actin turnover. The stress fiber has sarcomeric structure, with actin filament barbed ends residing at the sarcomere boundaries and pointed ends interacting with nonmuscle myosin-II minifilaments in sarcomere centers (Fig. 5.5A). We assume that actin turns over via a treadmilling-like mechanism, with actin subunits incorporating at actin barbed ends with rate v_+ and disassembly occurring in the sarcomere centers at rate v_-, consistent with observations of preferential incorporation of microinjected actin monomers into α-actinin regions.[103] To maintain a steady state actin filament length and to avoid unconstrained fluctuations,[107] the turnover rates must be regulated. We assume that the overlap of actin pointed ends[39] causes compressive elastic forces that mechanically regulate the disassembly rate

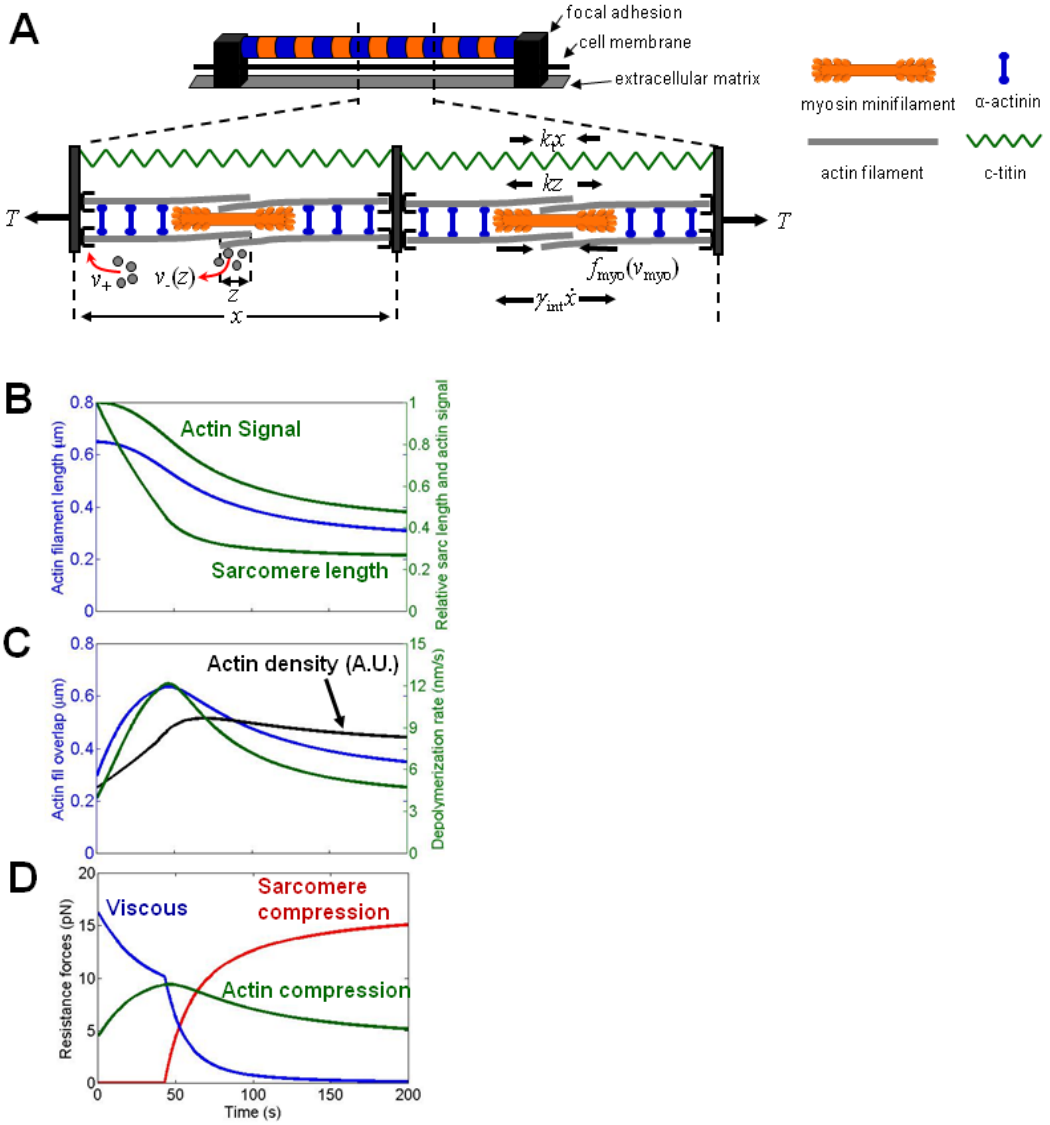

Figure 5.5: Mathematical model of stress fibers

(A) Mathematical model of stress fibers. Myosin contractile forces, f_{myo}, and elastic forces from titin, $k_t x$, tend to shorten the sarcomere, whereas the tension T, actin overlap force kz, and sarcomeric viscous forces $-\gamma_{int}\dot{x}$ resist contraction. The minimum sarcomere length is determined by sarcomeric elastic forces with elastic constant k_{sarc}. Actin turnover occurs by a treadmiling-like mechanism, with barbed end assembly at rate v_+ and disassembly near the pointed end at rate v_-^0 that increases with increasing actin overlap forces.

(B) Model predictions for stress fiber shortening, amount of actin in the sarcomere, and actin filament length over time during recoil of a spontaneously severed stress fiber. The actin signal is proportional to the actin filament length. All parameters as in Table 5.1.

(C) Model predictions for actin-actin overlap, depolymerization rate, and actin density. The overlap and depolymerization rate increase until recoil is finished and then decay. All parameters as in Table 5.1.

(D) Model predictions for the resistance forces to contraction. The myosin contractile forces work against both sarcomeric viscosity and actin-actin compression. At the completion of recoil, sarcomeric elasticity becomes dominant. All parameters as in Table 5.1.

according to $v_- = v_-^0 e^{kz/p^*}$, where v_-^0 is the disassembly rate in the absence of force, k is the elastic constant of pointed end overlap, z is the length of overlap between actin pointed ends, and p^* is the characteristic force that promotes disassembly. Equating the actin assembly and disassembly rates, at steady state the actin filament overlap is $z_{ss} = (p^*/k)\ln(v_+/v_-^0)$.

Actin assembly and disassembly can change either the sarcomere length or the actin filament overlap, resulting in the length balance equation,

$$\dot{x} + \dot{z} = v_+ - v_-^0 e^{kz/p^*}, \tag{5.1}$$

where dots denote time derivatives, and x is the sarcomere length.

Forces in the stress fiber. Each myosin-II minifilament exerts contractile force $f_{myo} = f_s + \gamma_{myo}(\dot{x} - v_+)$, where f_s is the stall force and γ_{myo} is the slope of the force-velocity relation at stall (see Table 5.1; γ_{myo} is the same as λ in Chapter 3). Note that even when the sarcomere length is not changing, the myosin is working at the actin polymerization velocity. Cellular titin[91] exerts a contractile force with elastic constant k_t. Contraction is resisted by internal viscous drag with coefficient γ_{int} and compressive elastic forces from pointed end overlap, kz. Since spontaneously severed stress fibers are not mechanically coupled to their surroundings (Fig. 5.1E and 5.2), the tension is uniform and all sarcomeres therefore have identical behavior. Thus, the force balance in each sarcomere is

$$T = f_s - \gamma_{myo}(v_+ - \dot{x}) + \gamma_{int}\dot{x} + k_t x - kz \quad , \tag{5.2}$$

where T is the stress fiber tension per minifilament. Finally, each sarcomere has minimum length l_{min} which is approached with spring constant k_{sarc}.

Solving the model. To solve for the fiber length and amount of actin in stress fibers after severing, we set $T = 0$ in Eq. 5.2 and take initial conditions $x(t = 0) = l_0$ and $z(t = 0) = z_{ss}$. Eqs. 5.1

Table 5.1: Parameter values used in the model of spontaneously severed stress fibers.

Symbol	Meaning	Value	Legend
Fixed parameter values			
l_0	Initial sarcomere length	1 μm	**(A)**
f_s	Myosin-II minifilament stall force	20 pN	**(B)**
γ_{myo}	Myosin-II minifilament drag coefficient	167 pN·s/μm	**(C)**
k_t	Titin spring constant per minifilament	4 pN/μm	**(D)**
k_{sarc}	Sarcomere brick wall spring constant	75 pN/μm	**(E)**
p^*	Characteristic compression to induce actin depolymerization	4.5 pN	**(F)**
v_+	Actin barbed end polymerization rate	4 nm/s	**(G)**
v_-^0	Actin pointed end depolymerization rate	1.5 nm/s	**(H)**
Fitting parameters			
k	Elastic constant of actin filament overlap	27.5 ± 6.4 pN/μm	**(I)**
γ_{int}	Internal sarcomere drag coefficient	1007 ± 276 pN·s/μm	**(I)**
l_{min}	Minimum sarcomere length after recoil	0.26 ± 0.03 μm	**(I)**

Legend:

(A) Measured by Sanger and Sanger[108] and Peterson et al.[41].

(B) Assumes 1.5 pN per myosin head as in striated muscle[83] and ~13 myosin-II molecules per minifilament.[11,158]

(C) γ_{myo} measures the reduction in myosin force as the sliding velocity increases, and is the slope of the myosin force-velocity relation near the stall force. $\gamma_{myo} = \beta f_s/(2v_{myo}^0)$, where v_{myo}^0 = 0.3 μm/s is the actin gliding velocity of nonmuscle myosin-II heads.[113] This velocity is doubled to account for the bipolar nature of the minifilament. The factor β = 5 is the value measured for striated muscle.[115] We take the value of γ_{myo} near the stall force because the stress fiber recoil time (15 – 30 s, Fig. 5.2B) is much larger than the time it would take for myosin to contract a sarcomere in the absence of any resistance ($l_0/2v_{myo}^0$ = 1.7 s). This parameter is the same as λ in Chapter 3.

(D) From Tskhovrebova et al.[102] at length <1 μm, assuming there is one titin molecule per myosin-II minifilament as observed in assemblies in vitro.[111]

(E) Has not been measured. Because the sarcomeres are less ordered than striated muscle, we assume the collapse spring constant is an order of magnitude smaller than the stiffness of the ascending limb of the muscle force-length curve, ~750 pN/μm.[109]

(F) $p^* \approx mk_BT/\delta$. Here, m = 3 is the number of actin filaments per myosin filament, taken to be similar to striated muscle,[117] and δ = 2.7 nm is the effective actin monomer size.[116]

(G) Assumed to be the sarcomere length (~1 μm) divided by the actin turnover time as measured by fluorescence recovery after photobleaching (FRAP, $t_{1/2}$ = 3-5 min).[43,44] Includes the contributions from both sets of filaments in the sarcomere.

(H) Twice the value measured in vitro for a single pointed end,[159] to account for both filaments in the sarcomere.

(I) Determined by fitting to the measured sarcomere length and actin density curves (Fig. 5.4C-E). Displayed as mean ± standard error of the mean (SEM) for n = 16 spontaneously severed stress fibers.

and 5.2 are then simultaneously solved numerically for the sarcomere length x and overlap length z over time. The actin filament lengths are $(x + z)/2$, the relative amount of actin in a sarcomere is $(x + z)/(l_0 + z_{ss})$, and the relative actin density is proportional to $(x + z)/x$.

IV. Model Results and Comparison to Experimental Data

Model predictions are in agreement with experimental measurements

Three model parameters have unknown values: the minimum sarcomere length l_{min}, the sarcomere drag coefficient γ_{int}, and the actin overlap elastic constant k. To determine their values, we fit the model to the measured sarcomere length and actin density curves for each stress fiber (n = 16, Fig. 5.4C-E, and Table 5.1). The fitting parameter space was directly searched to minimize the sum of squared errors between model and experiment, and the parameters were determinable because the mean cross correlations between parameters were -0.10, 0.28, and -0.79 for γ_{int} and l_{min}, γ_{int} and k, and l_{min} and k, respectively. The model was in excellent agreement with the experimental measurements, reproducing both the recoil curves (Fig. 5.4C) and the actin density over time (Fig. 5.4E). The actin density initially increases, then peaks and decays just as in the experiments (Fig. 5.4C).

The steady-state actin overlap is constant, explaining why the actin density is higher after recoil

We used the model to understand why the actin density after recoil is ~2-fold larger than before severing (Fig. 5.3B). The actin filament overlap at steady state is $z_{ss} = (p^*/k)\ln(v_+/v_-^0)$ (see above). This actin overlap is independent of the sarcomere length, and has value $z_{ss} \approx 0.3$ μm

using the parameters from Table 5.1. Therefore, the actin density after recoil is larger than the initial actin density (Fig. 5.3B) simply because the steady state actin overlap region is a larger fraction of the total sarcomere length in shorter sarcomeres.

Actin filament shortening accompanies recoil due to disassembly caused by compressive stresses

The actin filament length in stress fibers has not been measured, so we tracked it during recoil using our simulation. Immediately after severing, stress fiber sarcomeres begin shortening while the actin filament length remains roughly constant (Fig. 5.5B). During this initial period, the sarcomere shortening causes the actin overlap to increase (Fig. 5.5C), increasing the actin compression force (Fig. 5.5D) and the actin disassembly rate (Fig. 5.5C). This delay period during which the actin overlap builds up corresponds to the depolymerization delay measured in Fig. 5.4B. After the delay, the actin filament length decreases due to the elevated disassembly rate (Fig. 5.5B). Therefore, the model predicts that actin filament shortening accompanies recoil.

Both viscous and elastic forces resist sarcomere shortening during recoil

In Chapter 3, we estimated that changing the actin filament length is the rate limiting step in sarcomere length relaxation (i.e., that the actin overlap force is much larger than viscous resistance to contraction). This was quantified by the parameter $r = \gamma_{myo}/(p^*/v_+)$, which is the ratio of the myosin drag coefficient γ_{myo} and the 'actin disassembly drag coefficient', p^*/v_+, and which we estimated as $r \approx 0.1$. Here, using the parameters from Table 5.1, we estimate

$$r = \frac{\gamma_{int} + \gamma_{myo}}{p^*/v_+} \approx 1.04 \quad , \tag{5.3}$$

where the internal sarcomere drag γ_{int} now also contributes to the viscous resistance. This parameter was needed in the present model to account for the fact that spontaneously severed stress fibers recoil far more slowly than they would if the myosin drag were the only viscous contribution. Thus, viscous resistance and resistance from actin filament overlap are equally important in determining stress fiber dynamics (Fig. 5.5D).

Effects of actin turnover on stress fiber recoil

We next investigated the effects of altered actin assembly and disassembly rates on stress fiber recoil. Holding all other parameters constant, we varied the actin assembly (v_+) and disassembly (v_-^0) rates in the model. Since the minimum sarcomere length l_{min} is independent of the turnover rates, the total amount of shortening during recoil is independent of v_+ and v_-^0.

However, the actin turnover rates are predicted to influence both the recoil duration and the amount of actin disassembly (Fig. 5.6A,B). The model predicts that inhibiting actin assembly (disassembly) decreases (increases) the recoil duration (Fig. 5.6A,B). This effect arises because the steady state actin overlap, $z_{ss} = (p^*/k)\ln(v_+/v_-^0)$, decreases when assembly is inhibited and increases when disassembly is inhibited. A larger overlap increases the recoil duration because the elastic actin-actin forces resist constriction, while a smaller overlap decreases the recoil duration by reducing the resistance to contraction.

The model also predicts that the relative amount of actin remaining in the stress fiber after recoil decreases (increases) when actin assembly (disassembly) is inhibited (Fig. 5.6A,B). This effect also arises because of the effect of turnover on the steady state overlap z_{ss}. A reduction in the actin assembly rate v_+ decreases the overlap, and therefore a larger fraction of

actin is shed when the sarcomere shrinks, while the opposite occurs for a reduction in the disassembly rate.

To test these predictions, we altered the ability of actin filaments to assemble and disassemble by treating cells with 0.2-1 μM jasplakinolide, which stabilizes actin filaments by decreasing their depolymerization rate,[160] or 50 nM of the actin polymerization inhibitor cytochalasin D[161] (Fig. 5.6D,E). Both drugs caused a large increase in the rate of spontaneous stress fiber severing (Fig. 5.6D,E). In particular, cytochalasin D treatment often caused the entire network of stress fibers to rupture and contract.

As predicted by the model, neither drug affected the fractional shortening of severed stress fibers (Fig. 5.6F). Jasplakinolide treatment caused a diminished loss of actin during recoil, and cytochalasin D treatment caused an enhanced loss of actin during recoil (Fig. 5.6G), although the latter was not statistically significant ($p = 0.12$). These results are in agreement with the model predictions assuming that main effect of the drugs is to alter v_+ and v_-^0 (Fig. 5.6A,B). However, the recoil duration was not affected by either drug (Fig. 5.6H), which is not consistent with the model predictions (Fig. 5.6A,B) if the drugs' main effect is to alter v_+ and v_-^0. It is possible that the drugs have other effects that complicate the interpretation of the experiments.

V. Discussion

By analyzing the recoil kinetics and actin dynamics of spontaneously severed stress fibers, we have identified a mechanism of coupling between contractility and actin turnover. We observed that stress fibers shed ~50% of their actin as thy shorten after severing, while their linear actin density increases, peaks, and then decays to a new value 2-fold larger than the initial

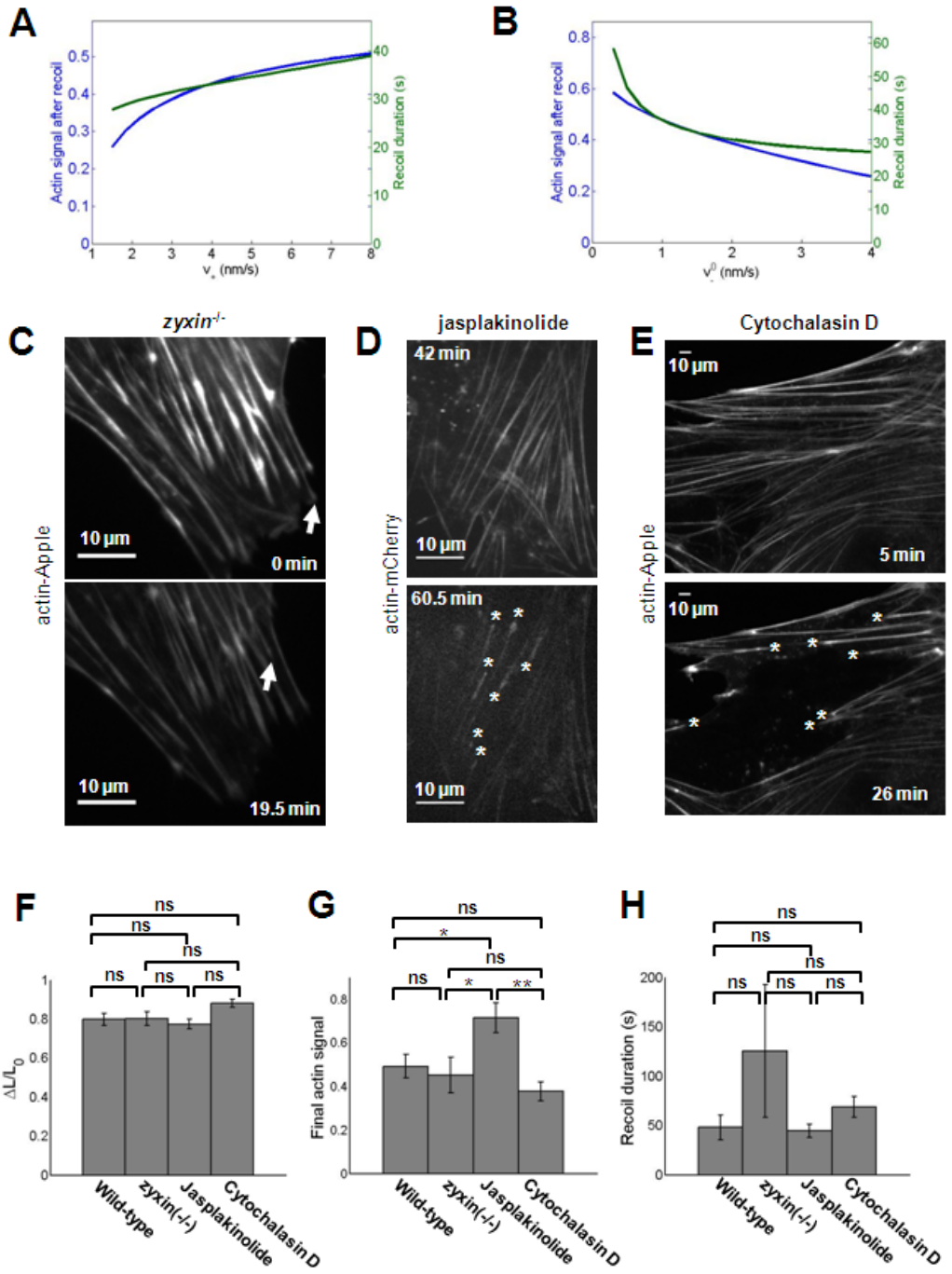

Figure 5.6. Effect of actin polymerization and depolymerization rates on recoil

(A) The model predicts that reducing the actin assembly rate v_+ decreases the recoil duration and the amount of actin remaining in the fiber after recoil.

(B) The model predicts that reducing the actin disassembly rate v_-^0 increases the recoil duration and the amount of actin remaining in the fiber after recoil.

(C) Time lapse confocal images of a spontaneously severing stress fiber in a *zyxin*$^{-/-}$ cell (arrows).

(D) Time lapse confocal images of a spontaneously severing stress fibers in a cell treated with 0.3 µM of jasplakinolide. Asterisks indicate severed ends. Time is measured after drug treatment.

(E) Time lapse confocal images of spontaneously severing stress fibers in a cell treated with cytochalasin D. Asterisks indicate severed ends. Time is measured after drug treatment.

(F) Fractional shortening of spontaneously severed stress fibers. A lack of zyxin (n=8), treatment with jasplakinolide (n = 15), and treatment with cytochalasin D (n = 12) do not alter the value from wild-type cells (n = 16).
(G) Relative amount of actin remaining in spontaneously severed stress fibers after recoil. The lack of zyxin has no effect (n = 8). However, treatment with jasplakinolide significantly decreased the amount of actin disassembly (n = 15) and treatment with cytochalasin D enhanced actin disassembly, although the difference was not statistically significant (n = 12, p = 0.12).
(H) Recoil duration of spontaneously severed stress fibers. A lack of zyxin (n=8), treatment with jasplakinolide (n = 15), and treatment with cytochalasin D (n = 12) do not alter the value from wild-type cells (n = 16).
Bar graphs show mean ± SEM. All micrographs from the Beckerle lab (University of Utah).

density. Our model explains this observation by positing that increasing actin density in the sarcomere causes compressive elastic forces that promote actin disassembly. During recoil, the actin density initially increases because the sarcomeres shrink faster than the actin filaments shorten. The increasing actin filament overlap force slows constriction and increases the actin disassembly rate. Eventually, the sarcomere reaches its minimum length and the density decreases as the disassembly continues. Therefore, the actin turnover in stress fibers is used to adjust the actin filament length in response to changes in the sarcomere length.

A key ingredient of our model is that compressive elastic forces resist the overlap of actin filaments in the centers of stress fiber sarcomeres. Such a force has not been measured in stress fibers, but when actin pointed ends overlap in striated muscle sarcomeres, the contractile force is reduced suggesting that a resistance force may be present.[109,131] Additionally, compression forces build up in vitro when surfaces with barbed-end tethered actin filaments are brought in close proximity.[162] From this study we estimate an elastic constant of ~2-5 pN/μm per actin filament, which is very close to the mean best fit value of ~9 pN/μm from our model (Table 5.1). The stiffness may be lower in vitro because of the lack of crosslinking proteins such as α-actinin that are present in stress fibers. The origin of the actin compression force is not clear. The situation is probably complex because the actin filaments are crosslinked and have a disordered organization compared to muscle, but the force may arise from bending or buckling of the actin filaments.

Another key model ingredient is the sensitivity of the actin disassembly rate to compressive forces in the actin filaments. This may occur by stresses on actin filament ends increasing the actin subunit off rate.[116] Alternatively, the activity of actin filament severing proteins such as cofilin may be sensitive to stress in the actin filament. In growth cones, it was shown that the presence of myosin contractility promotes the bending and breakage of actin filaments.[163] Our model is general and does not depend on any particular mechanism of stress-sensitivity. This will be an interesting subject for future studies.

What is the purpose of coupling of contraction and actin turnover in stress fiber sarcomeres? The ability to adjust actin filament lengths in response to changes in stress fiber length may allow the stress fiber to efficiently generate tension over a wide range of sarcomere lengths, appropriate for the dynamic mechanical conditions in nonmuscle cells. By contrast, actin filaments in striated muscle have stable lengths with little actin turnover, and muscle sarcomeres typically work over a relatively small range of lengths.[112]

Appendix A: Experimental Procedures

Materials

Cell lines. Production and immortalization of fibroblasts derived from wild-type and zyxin null mice was described previously.[157] Fibroblasts derived from zyxin$^{-/-}$ mice were stably rescued with N-terminally tagged zyxin by viral infection followed by FACS sorting to select cells expressing fluorescently tagged zyxin.[157]

Cell culture and transfection. Cells were cultured in DMEM supplemented with L-glutamine, penicillin/streptomycin, sodium pyruvate, and 10% fetal bovine serum (Hyclone) and

grown on coverslips coated with fibronectin (10 mg/ml). Transient transfections of DNA constructs for expression of fluorescently tagged proteins were performed using FuGENE HD transfection reagent (Roche). Time-lapse imaging of cells was performed 3–6 days after transfection.

DNA constructs. *pmCherry-actin-* The mCherry coding sequence was amplified from pRSET-B-mCherry, digested with AgeI and BglII and ligated in place of GFP in pEGFP-actin (Clontech, cat# PT3265-5). Other plasmids were generous gifts from Dr. Michael Davidson (Florida State University): pActin:mApple; Dr. Carol Otey (University of North Carolina, Chapel Hill): α-actinin-GFP.

Live-cell imaging for protein dynamic studies

Coverslips were mounted in a closed chamber (LIS), with DMEM/F12 media (Invitrogen) supplemented with 10% fetal bovine serum. Cells were maintained at 37°C using a microscope temperature control system (LIS). Imaging was performed on an Andor spinning disk confocal on an inverted Nikon TE300 microscope with a 603 1.4NA Nikon Plan Apochromat lens. Illumination was from solid state 488 and 568 nm lasers (Melles Griot), switched by an acousto-optic tunable filter based laser combiner (Andor Technology), and delivered by optical fiber to the Yokogawa CSU-10 scanhead. The emission light path was equipped with a dual bandpass filter (Semrock Inc). Timelapse image sequences were captured at 2 or 10 s intervals using either Andor DV887 1024X1024 EMCCD camera, or Andor DV885 512X512 EMCCD camera (Andor Technology). Stage motions were controlled in XY with a Ludl XY stage (Ludl Electronic Products) and in Z with a Piezo stage insert (Mad City Labs). Image acquisition was

performed using Andor IQ imaging software (Andor Technologies) on a PC workstation (Dell Computers).

Image analysis

Analysis of stress fiber recoil. At each time frame, a line was drawn along the stress fiber using ImageJ software (http://rsb.info.nih.gov/ij/). The line width was chosen to be slightly larger than the fiber width, typically 8-15 pixels. The actin fluorescence intensity profile along the line averaged over its width, $I(y)$, was measured and smoothed, where y increases in the direction of the severed end. The fiber length L is the distance between the position of the intact end and the position of the severed end, defined as the position where $\partial I/\partial y$ is minimum. Each fiber's $L(t)$ curve was fit with an exponential function, $L_f + \Delta L\exp(-t/\tau)$ to determine the recoil duration τ. In kymographs of α-actinin or zyxin fluorescence, fiduciary marks were identified as minima of $\partial I/\partial y$.

Quantitation of fluorescence in stress fibers. Using ImageJ software, for each time frame the total intensity of a labeled component was measured in a box drawn around the stress fiber, from the intact end to the position of the severed end. Background correction was made by subtracting the ctyoplasmic intensity immediately adjacent to the fiber. The photobleaching correction curve was taken as the mean of the decay of fluorescence intensity in 3 nearby quiescent stress fibers in the same cell. Severing events were discarded if these 3 photobleaching curves were not nearly identical. The optical sections of the confocal microscope were ~1.2 μm thick, >2 times thicker than a typical stress fiber. Therefore it was assumed that the entire stress fiber resides in a single section. This was confirmed by verifying that the intensity where two stress fibers intersect is equal to the sum of the individual fiber intensities near their intersection

(n = 5). Some severing events were rejected because of excessive photobleaching, movement out of the field of view, or lifting out of the focal plane.

Analysis of stress fiber width. ImageJ software was used to draw 5-pixel-wide lines across the stress fiber in the *y* direction, perpendicular to its axis. A Gaussian function was fit to the actin intensity profile along the line, $I(y) = [\sigma(2\pi)^{1/2}]^{-1}\exp[-(y-\mu)^2/(2\sigma^2)] + I_0$, and the width was defined as the full width half max, $2\sigma(2\ln 2)^{1/2}$. Each width measurement is the average of the width at the three locations: near the intact fiber end, in the center of the fiber, and near the severed end. Widths were measured either immediately after breakage or after recoil was complete.

Statistical analysis. Statistical significance for the recoil fraction, recoil duration, fluorescence intensity, and linear density were determined using unpaired, two-tailed t tests. Statistical significance for fiber width was determined using a paired, two-tailed t test. Differences were considered significant at the 95% confidence level. Statistical significance denoted as follows: *** $p < 0.001$; ** $p = 0.001$–0.01; * $p = 0.01$–0.05; ns, $p > 0.05$.

Chapter 6

Conclusion

In this thesis, we have made strides toward a mechanistic understanding of actomyosin contractility, a process fundamental to life. We developed detailed mathematical models of the actomyosin cytoskeleton in close collaboration with experimentalists, focusing on two prominent cytoskeletal structures: the contractile ring and stress fibers.

Cytokinesis and the contractile ring

While the protein composition and formation mechanism of the contractile ring have been studied in great detail, relatively little progress has been made in understanding ring constriction during cytokinesis. Unlike striated muscle, which has a sarcomeric structure specifically geared toward tension production, the ring appears to have a random organization and its mechanism of constriction is unknown. In this thesis, we presented a detailed model of how the ring works as a contractile machine to constrict and divide the cell into two daughter cells. This work is the result of a close collaboration with the laboratory of Thomas Pollard at Yale University, using the fission yeast model organism whose cytokinesis process is similar to, yet much simpler to study than that of animal cells. Our model is the first model to incorporate the measured concentrations of key ring components, and the first model to explicitly include ring anchoring and turnover.

To have useful predictive value any model of the ring must be able to predict the ring constriction rate, which is the most obvious and most easily measurable aspect of cytokinesis.

However, predicting the ring constriction rate in normal fission yeast cells is not possible given the current limited understanding of the septation process that is closely coupled to ring constriction. To overcome this obstacle, we studied ring constriction in fission yeast protoplasts whose cell wall had been digested, preventing septation and cell cleavage. The ring then constricted by sliding along the cell membrane, allowing direct comparison between model and experiment.

We concluded from our experimental and theoretical analysis that the ring is a tension-generating contractile machine. Our work indicates that to ensure optimum generation of tension, myosin oligomers bind and pull on actin filaments that are anchored at their barbed ends. The ring is strongly anchored to the membrane, ~20-fold more strongly than the precursor nodes that form the ring. Rapid formin and actin turnover refresh the ring organization so that the tension does not run down and allow for remodeling of the ring over a longer timescale, ensuring that actin maintains a constant concentration during constriction.

The model makes specific, novel predictions that can be tested experimentally: (1) Actin filament barbed ends are anchored to the membrane so that the ring can generate tension. This could be tested using electron microscopy. (2) Actin turns over ~3-fold faster than formin in the ring. This could be directly tested if a fluorescent label for actin could be developed that does not prevent its incorporation in to the ring. (3) The magnitude of the ring tension is ~40-80 pN and the tension fluctuates on a time scale of ~20 s. (4) The magnitude of the ring tension depends on the statistical correlations between actin filament and myosin oligomer positions (Eq. 2.1). This finding provides a framework for a novel set of measurements on contractile rings. Simultaneously measuring the spatial distribution of fluorescently labeled actin and myosin in

the ring could allow characterization of the ring structure by calculating the sarcomericity ψ_{sarc} (Eq. 2.1).

The work in this thesis is also the first demonstration of the force balance on the contractile ring during constriction. To our knowledge, the only direct measurements of ring tension were performed by Rappaport in 1967.[81] However, in that work the contractile ring was stalled during constriction using a needle so that the maximum ring tension was measured rather than the actual tension during constriction. By predicting and measuring the shape of the contractile ring in protoplasts, we showed that rings generate tension and work against external forces even when not stalled by an external probe. Since rings in protoplast constricted at the same rate as rings in intact cells, rings in intact cells would generate the same tension as the protoplast rings. While our work has begun to reveal the mechanisms of the contractile ring, it also shows that understanding the resistance forces to constriction is critical for understanding the dynamics of constriction. Thus, future work should investigate septation dynamics and how septum growth is coupled to the ring tension.

Stress fibers

While the structure of stress fibers appears to be related to the sarcomeric structure of muscle, stress fibers are more disordered and their mechanism of contraction is not fully characterized. As in muscle, myosin filaments in sarcomere centers interact with actin filaments to produce tension and contraction. However, whether the turnover of actin in stress fibers (which is not present in muscle) is involved in contraction and whether stress fibers are coupled to their surroundings is unknown.

In this thesis, we presented the first measurements and mathematical modeling of actin turnover and remodeling during stress fiber contraction. Analysis of the recoil of spontaneously severed fibers led us to conclude that stress fibers are not mechanically coupled to their surroundings and that actin turnover is coupled to contractile forces. Our work suggests that the overlap of actin filaments in the center of stress fiber sarcomeres causes a compressive elastic force that increases the rate of actin disassembly rate. This feedback between elastic stress and actin disassembly allows actin filaments to shorten and lengthen in response to contraction and extension, respectively, thereby endowing stress fiber sarcomeres with a large range of stable operating lengths. Thus, the mechanosensitivity gives the cell flexibility by allowing stress fibers to maintain structural integrity while undergoing large changes in length. It will be interesting to test whether this may be a general mechanism employed by other cytoskeletal structures in cells that must rapidly adjust and respond to mechanically dynamic environments.

Our conclusion that actin disassembly and compressive mechanical stress are coupled suggests several experiments. The mechanism of mechanosensitivity is unknown; in vitro methods could be used determine whether the activity of cofilin or other factors involved in actin filament disassembly are sensitive to compressive stress in actin filaments. In vitro experiments could also be designed to characterize the compressive force of that builds up when arrays of actin filaments overlap.

References

1. T. D. Pollard (2010). Mechanics of cytokinesis in eukaryotes. *Curr. Opin. Cell Biol.* 22, 50-56.

2. K. A. Beningo and Y. L. Wang (2002). Flexible substrata for the detection of cellular traction forces. *Trends Cell Biol.* 12, 79-84.

3. A. J. Ridley, M. A. Schwartz, K. Burridge, R. A. Firtel, M. H. Ginsberg, G. Borisy, J. T. Parsons and A. R. Horwitz (2003). Cell migration: Integrating signals from front to back. *Science* 302, 1704-1709.

4. G. Gabbiani, G. B. Ryan, P. R. Statkov, B. J. Hirschel and G. Majno (1972). Granulation tissue as a contractile organ - study of structure and function. *J. Exp. Med.* 135, 719-734.

5. J. J. Tomasek, G. Gabbiani, B. Hinz, C. Chaponnier and R. A. Brown (2002). Myofibroblasts and mechano-regulation of connective tissue remodelling. *Nat. Rev. Mol. Cell Biol.* 3, 349-363.

6. A. F. Huxley (1974). Muscular contraction *J. Physiol. (Lond.)* 243, 1-43.

7. R. Cooke (1997). Actomyosin interaction in striated muscle. *Physiol. Rev.* 77, 671-697.

8. G. T. Charras, C. K. Hu, M. Coughlin and T. J. Mitchison (2006). Reassembly of contractile actin cortex in cell blebs. *J. Cell Biol.* 175, 477-490.

9. C. A. Mandato and W. M. Bement (2001). Contraction and polymerization cooperate to assemble and close actomyosin rings around xenopus oocyte wounds. *J. Cell Biol.* 154, 785-797.

10. B. Alberts, D. Bray, J. Lewis, M. Raff, K. Roberts and J. D. Watson (2002). Molecular biology of the cell (New York, Garland Publishing).

11. A. B. Verkhovsky and G. G. Borisy (1993). Non-sarcomeric mode of myosin II organization in the fibroblast lamellum. *J. Cell Biol.* 123, 637-652.

12. R. Niederman and T. D. Pollard (1975). Human platelet myosin: 2. In vitro assembly and structure of myosin filaments. *J. Cell Biol.* 67, 72-92.

13. J. A. Knoblich (2001). Asymmetric cell division during animal development. *Nat. Rev. Mol. Cell Biol.* 2, 11-20.

14. T. Fujiwara, M. Bandi, M. Nitta, E. V. Ivanova, R. T. Bronson and D. Pellman (2005). Cytokinesis failure generating tetraploids promotes tumorigenesis in p53-null cells. *Nature* 437, 1043-1047.

15. U. S. Eggert, T. J. Mitchison and C. M. Field (2006). Animal cytokinesis: From parts list to mechanisms. *Annu. Rev. Biochem.* 75, 543-566.

16. C. M. Caldwell, R. A. Green and K. B. Kaplan (2007). APC mutations lead to cytokinetic failures in vitro and tetraploid genotypes in min mice. *J. Cell Biol.* 178, 1109-1120.

17. E. A. Harrington, D. Bebbington, J. Moore, R. K. Rasmussen, A. O. Ajose-Adeogun, T. Nakayama, J. A. Graham, C. Demur, T. Hercend, et al. (2004). VX-680, a potent and selective small-molecule inhibitor of the Aurora kinases, suppresses tumor growth in vivo. *Nat. Med.* 10, 262-267.

18. J. J. Reiners, M. Kleinman, A. Joiakim and P. A. Mathieu (2009). The chemotherapeutic agents xk469 (2-{4-[(7-chloro-2-quinoxalinyl)oxy]phenoxy}propionic acid) and SH80 (2-{4-[(7-bromo-2-quinolinyl)oxy]phenoxy}propionic acid) inhibit cytokinesis and promote polyploidy and induce senescence. *J. Pharmacol. Exp. Ther.* 328, 796-806.

19. M. K. Balasubramanian, E. Bi and M. Glotzer (2004). Comparative analysis of cytokinesis in budding yeast, fission yeast and animal cells. *Curr. Biol.* 14, R806-R818.

20. J. Q. Wu and T. D. Pollard (2005). Counting cytokinesis proteins globally and locally in fission yeast. *Science* 310, 310-314.

21. J. Q. Wu, V. Sirotkin, D. R. Kovar, M. Lord, C. C. Beltzner, J. R. Kuhn and T. D. Pollard (2006). Assembly of the cytokinetic contractile ring from a broad band of nodes in fission yeast. *J. Cell Biol.* 174, 391-402.

22. D. Vavylonis, J. Q. Wu, S. Hao, B. O'Shaughnessy and T. D. Pollard (2008). Assembly mechanism of the contractile ring for cytokinesis by fission yeast. *Science* 319, 97-100.

23. J. Q. Wu, J. R. Kuhn, D. R. Kovar and T. D. Pollard (2003). Spatial and temporal pathway for assembly and constriction of the contractile ring in fission yeast cytokinesis. *Dev. Cell* 5, 723-734.

24. R. J. Pelham and F. Chang (2002). Actin dynamics in the contractile ring during cytokinesis in fission yeast. *Nature* 419, 82-86.

25. E. Streiblova, I. Malek and K. Beran (1966). Structural changes in the cell wall of Schizosaccharomyces pombe during cell division. *J. Bacteriol.* 91, 428-35.

26. B. F. Johnson, B. Y. Yoo and G. B. Calleja (1973). Cell division in yeasts: Movement of organelles associated with cell plate growth of Schizosaccharomyces pombe. *J. Bacteriol.* 115, 358-66.

27. M. Sipiczki and A. Bozsik (2000). The use of morphomutants to investigate septum formation and cell separation in Schizosaccharomyces pombe. *Arch. Microbiol.* 174, 386-92.

28. M. Osumi, M. Sato, S. A. Ishijima, M. Konomi, T. Takagi and H. Yaguchi (1998). Dynamics of cell wall formation in fission yeast, Schizosaccharomyces pombe. *Fungal Genet. Biol.* 24, 178-206.

29. J. Jochova, I. Rupes and E. Streiblova (1991). F-actin contractile rings in protoplasts of the yeast Schizosaccharomyces. *Cell Biol. Int. Rep.* 15, 607-10.

30. M. Sipiczki, W. D. Heyer and J. Kohli (1985). Preparation and regeneration of protoplasts and spheroplasts for fusion and transformation of Schizosaccharomyces-pombe. *Curr. Microbiol.* 12, 169-173.

31. A. Carvalho, A. Desai and K. Oegema (2009). Structural memory in the contractile ring makes the duration of cytokinesis independent of cell size. *Cell* 137, 926-937.

32. S. Pellegrin and H. Mellor (2007). Actin stress fibres. *J. Cell Sci.* 120, 3491-3499.

33. G. E. White, M. A. Gimbrone and K. Fujiwara (1983). Factors influencing the expression of stress fibers in vascular endothelial cells in situ. *J. Cell Biol.* 97, 416-424.

34. A. J. Wong, T. D. Pollard and I. M. Herman (1983). Actin filament stress fibers in vascular endothelial cells in vivo. *Science* 219, 867-869.

35. A. J. Hayes, M. Benjamin and J. R. Ralphs (1999). Role of actin stress fibres in the development of the intervertebral disc: Cytoskeletal control of extracellular matrix assembly. *Dev. Dyn.* 215, 179-189.

36. J. R. Ralphs, A. D. Waggett and M. Benjamin (2002). Actin stress fibres and cell-cell adhesion molecules in tendons: Organisation in vivo and response to mechanical loading of tendon cells in vitro. *Matrix Biol.* 21, 67-74.

37. H. Iwamoto, M. Nakamuta, S. Tada, R. Sugimoto, M. Enjoji and H. Nawata (2000). A p160ROCK-specific inhibitor, Y-27632, attenuates rat hepatic stellate cell growth. *J. Hepatol.* 32, 762-770.

38. H. F. Yee (1998). Rho directs activation-associated changes in rat hepatic stellate cell morphology via regulation of the actin cytoskeleton. *Hepatology* 28, 843-850.

39. L. P. Cramer, M. Siebert and T. J. Mitchison (1997). Identification of novel graded polarity actin filament bundles in locomoting heart fibroblasts: Implications for the generation of motile force. *J. Cell Biol.* 136, 1287-1305.

40. W. E. Gordon (1978). Immunofluorescent and ultrastructural studies of sarcomeric units in stress fibers of cultured non-muscle cells. *Exp. Cell Res.* 117, 253-260.

41. L. J. Peterson, Z. Rajfur, A. S. Maddox, C. D. Freel, Y. Chen, M. Edlund, C. Otey and K. Burridge (2004). Simultaneous stretching and contraction of stress fibers in vivo. *Mol. Biol. Cell* 15, 3497-3508.

42. S. Clement, B. Hinz, V. Dugina, G. Gabbiani and C. Chaponnier (2005). The N-terminal Ac-EEED sequence plays a role in alpha-smooth-muscle actin incorporation into stress fibers. *J. Cell Sci.* 118, 1395-1404.

43. P. Hotulainen and P. Lappalainen (2006). Stress fibers are generated by two distinct actin assembly mechanisms in motile cells. *J. Cell Biol.* 173, 383-394.

44. S. Kumar, I. Z. Maxwell, A. Heisterkamp, T. R. Polte, T. P. Lele, M. Salanga, E. Mazur and D. E. Ingber (2006). Viscoelastic retraction of single living stress fibers and its impact on cell shape, cytoskeletal organization, and extracellular matrix mechanics. *Biophys. J.* 90, 3762-3773.

45. I. Mabuchi and M. Okuno (1977). Effect of myosin antibody on division of starfish blastomeres. *J. Cell Biol.* 74, 251-263.

46. A. De Lozanne and J. A. Spudich (1987). Disruption of the Dictyostelium myosin heavy-chain gene by homologous recombination. *Science* 236, 1086-1091.

47. T. D. Pollard and J. Q. Wu (2010). Understanding cytokinesis: Lessons from fission yeast. *Nat. Rev. Mol. Cell Biol.* 11, 149-155.

48. W. Ge and M. K. Balasubramanian (2008). Pxl1p, a paxillin-related protein, stabilizes the actomyosin ring during cytokinesis in fission yeast. *Mol. Biol. Cell* 19, 1680-1692.

49. R. Martin-Garcia and M. H. Valdivieso (2006). The fission yeast Chs2 protein interacts with the type-II myosin Myo3p and is required for the integrity of the actomyosin ring. *J. Cell Sci.* 119, 2768-79.

50. T. Kanbe, I. Kobayashi and K. Tanaka (1989). Dynamics of cytoplasmic organelles in the cell cycle of the fission yeast Schizosaccharomyces pombe: 3-dimensional reconstruction from serial sections. *J. Cell Sci.* 94, 647-656.

51. T. Kamasaki, M. Osumi and I. Mabuchi (2007). Three-dimensional arrangement of F-actin in the contractile ring of fission yeast. *J. Cell Biol.* 178, 765-771.

52. E. Szafer-Glusman, M. G. Giansanti, R. Nishihama, B. Bolival, J. Pringle, M. Gatti and M. T. Fuller (2008). A role for very-long-chain fatty acids in furrow ingression during cytokinesis in Drosophila spermatocytes. *Curr. Biol.* 18, 1426-1431.

53. R. H. Roberts-Galbraith, J. S. Chen, J. Q. Wang and K. L. Gould (2009). The SH3 domains of two PCH family members cooperate in assembly of the Schizosaccharomyces pombe contractile ring. *J. Cell Biol.* 184, 113-127.

54. J. H. Liu, X. Tang, H. Y. Wang, S. Oliferenko and M. K. Balasubramanian (2002). The localization of the integral membrane protein Cps1p to the cell division site is dependent on the actomyosin ring and the septation-inducing network in Schizosaccharomyces pombe. *Mol. Biol. Cell* 13, 989-1000.

55. D. R. Kovar, E. S. Harris, R. Mahaffy, H. N. Higgs and T. D. Pollard (2006). Control of the assembly of ATP- and ADP-actin by formins and profilin. *Cell* 124, 423-435.

56. R. H. Carnahan and K. L. Gould (2003). The PCH family protein, Cdc15p, recruits two F-actin nucleation pathways to coordinate cytokinetic actin ring formation in Schizosaccharomyces pombe. *J. Cell Biol.* 162, 851-862.

57. T. E. Schroeder and J. J. Otto (1988). Immunofluorescent analysis of actin and myosin in isolated contractile rings of sea-urchin eggs. *Zool. Sci.* 5, 713-725.

58. N. I. Naqvi, K. Eng, K. L. Gould and M. K. Balasubramanian (1999). Evidence for F-actin-dependent and -independent mechanisms involved in assembly and stability of the medial actomyosin ring in fission yeast. *EMBO J.* 18, 854-862.

59. T. E. Schroeder (1972). The contractile ring. II. Determining its brief existence, volumetric changes, and vital role in cleaving arbacia eggs. *J. Cell Biol.* 53, 419-34.

60. K. Nakano and I. Mabuchi (2006). Actin-depolymerizing protein Adf1 is required for formation and maintenance of the contractile ring during cytokinesis in fission yeast. *Mol. Biol. Cell* 17, 1933-1945.

61. D. Biron, E. Alvarez-Lacalle, T. Tlusty and E. Moses (2005). Molecular model of the contractile ring. *Phys. Rev. Lett.* 95, 098102.

62. W. D. Zhang and D. N. Robinson (2005). Balance of actively generated contractile and resistive forces controls cytokinesis dynamics. *Proc. Natl. Acad. Sci. U.S.A.* 102, 7186-7191.

63. A. Zumdieck, K. Kruse, H. Bringmann, A. A. Hyman and F. Julicher (2007). Stress generation and filament turnover during actin ring constriction. *PLoS ONE* 2, e696.

64. S. G. Martin and F. Chang (2006). Dynamics of the formin for3p in actin cable assembly. *Curr. Biol.* 16, 1161-1170.

65. D. G. Drubin, K. G. Miller and D. Botstein (1988). Yeast actin-binding proteins - evidence for a role in morphogenesis. *J. Cell Biol.* 107, 2551-2561.

66. M. Lord and T. D. Pollard (2004). UCS protein Rng3p activates actin filament gliding by fission yeast myosin-II. *J. Cell Biol.* 167, 315-325.

67. S. C. Ti and T. D. Pollard (2011). Purification of actin from fission yeast Schizosaccharomyces pombe and characterization of functional differences from muscle actin. *J. Biol. Chem.* 286, 5784-5792.

68. L. Blanchoin and T. D. Pollard (1999). Mechanism of interaction of Acanthamoeba actophorin (ADF/cofilin) with actin filaments. *J. Biol. Chem.* 274, 15538-15546.

69. E. Andrianantoandro and T. D. Pollard (2006). Mechanism of actin filament turnover by severing and nucleation at different concentrations of ADF/cofilin. *Mol. Cell* 24, 13-23.

70. A. Michelot, J. Berro, C. Guerin, R. Boujemaa-Paterski, C. J. Staiger, J. L. Martiel and L. Blanchoin (2007). Actin-filament stochastic dynamics mediated by ADF/cofilin. *Curr. Biol.* 17, 825-833.

71. A. Yonetani, R. J. Lustig, J. B. Moseley, T. Takeda, B. L. Goode and F. Chang (2008). Regulation and targeting of the fission yeast formin cdc12p in cytokinesis. *Mol. Biol. Cell* 19, 2208-2219.

72. R. K. Meyer and U. Aebi (1990). Bundling of actin filaments by alpha-actinin depends on its molecular length. *J. Cell Biol.* 110, 2013-2024.

73. M. Claessens, M. Bathe, E. Frey and A. R. Bausch (2006). Actin-binding proteins sensitively mediate F-actin bundle stiffness. *Nat. Mater.* 5, 748-753.

74. J. Y. Xu, D. Wirtz and T. D. Pollard (1998). Dynamic cross-linking by alpha-actinin determines the mechanical properties of actin filament networks. *J. Biol. Chem.* 273, 9570-9576.

75. A. B. Verkhovsky, T. M. Svitkina and G. G. Borisy (1997). Polarity sorting of actin filaments in cytochalasin-treated fibroblasts. *J. Cell Sci.* 110, 1693-1704.

76. M. Zhou and Y.-L. Wang (2008). Distinct pathways for the early recruitment of myosin II and actin to the cytokinetic furrow. *Mol. Biol. Cell* 19, 318-326.

77. R. Albertson, B. Riggs and W. Sullivan (2005). Membrane traffic: A driving force in cytokinesis. *Trends Cell Biol.* 15, 92-101.

78. S. Mukhina, Y.-l. Wang and M. Murata-Hori (2007). Alpha-actinin is required for tightly regulated remodeling of the actin cortical network during cytokinesis. *Dev. Cell* 13, 554-565.

79. H. E. Huxley (1963). Electron microscope studies on structure of natural and synthetic protein filaments from striated muscle. *J. Mol. Biol.* 7, 281-308.

80. I. Mabuchi, S. Tsukita and T. Sawai (1988). Cleavage furrow isolated from newt eggs - contraction, organization of the actin filaments, and protein components of the furrow. *Proc. Natl. Acad. Sci. U.S.A.* 85, 5966-5970.

81. R. Rappaport (1967). Cell division: Direct measurement of maximum tension exerted by furrow of echinoderm eggs. *Science* 156, 1241-1243.

82. N. Q. Balaban, U. S. Schwarz, D. Riveline, P. Goichberg, G. Tzur, I. Sabanay, D. Mahalu, S. Safran, A. Bershadsky, et al. (2001). Force and focal adhesion assembly: A close relationship studied using elastic micropatterned substrates. *Nat. Cell Biol.* 3, 466-472.

83. J. Howard (2001). Mechanisms of motor proteins and the cytoskeleton (Sunderland, MA, Sinauer Associates).

84. G. H. Lan, C. W. Wolgemuth and S. X. Sun (2007). Z-ring force and cell shape during division in rod-like bacteria. *Proc. Natl. Acad. Sci. U.S.A.* 104, 16110-16115.

85. J. Berro, V. Sirotkin and T. D. Pollard (2010). Mathematical modeling of endocytic actin patch kinetics in fission yeast: Disassembly requires release of actin filament fragments. *Mol. Biol. Cell* 21, 2905-2915.

86. M. R. Stachowiak and B. O'Shaughnessy (2008). Kinetics of stress fibers. *New J. Phys.* 10, 025002.

87. T. D. Pollard and W. C. Earnshaw (2002). Cell biology (New York, W. B. Saunders).

88. M. Yoshigi, L. M. Hoffman, C. C. Jensen, H. J. Yost and M. C. Beckerle (2005). Mechanical force mobilizes zyxin from focal adhesions to actin filaments and regulates cytoskeletal reinforcement. *J. Cell Biol.* 171, 209-215.

89. D. E. Ingber (2003). Tensegrity I. Cell structure and hierarchical systems biology. *J. Cell Sci.* 116, 1157-1173.

90. R. Rappaport (1996). Cytokinesis in animal cells (Cambridge, Cambridge University Press).

91. P. J. Cavnar, S. G. Olenych and T. C. S. Keller (2007). Molecular identification and localization of cellular titin, a novel titin isoform in the fibroblast stress fiber. *Cell Motil. Cytoskeleton* 64, 418-433.

92. A. F. Huxley (1957). Muscle structure and theories of contraction. *Prog. Biophys. Mol. Biol.* 7, 255-318.

93. T. M. Svitkina, I. G. Surguchova, A. B. Verkhovsky, V. I. Gelfand, M. Moeremans and J. Demey (1989). Direct visualization of bipolar myosin filaments in stress fibers of cultured fibroblasts. *Cell Motil. Cytoskeleton* 12, 150-156.

94. J. L. Tan, S. Ravid and J. A. Spudich (1992). Control of nonmuscle myosins by phosphorylation. *Annu. Rev. Biochem.* 61, 721-759.

95. K. Sekimoto and H. Nakazawa (1996). Contraction of a bundle of actin filaments: 50 years after Szent-Gyorgyi. In Current topics in physics, Y. M. Cho, J. B. Hong and C. N. Yang, eds. (Singapore, World Scientific), pp. 394 - 405.

96. K. Kruse and F. Julicher (2000). Actively contracting bundles of polar filaments. *Phys. Rev. Lett.* 85, 1778-1781.

97. K. Takiguchi (1991). Heavy meromyosin induces sliding movements between antiparallel actin filaments. *J. Biochem.* 109, 520-527.

98. V. S. Deshpande, R. M. McMeeking and A. G. Evans (2006). A bio-chemo-mechanical model for cell contractility. *Proc. Natl. Acad. Sci. U.S.A.* 103, 14015-14020.

99. G. Civelekoglu-Scholey, A. W. Orr, I. Novak, J. J. Meister, M. A. Schwartz and A. Mogilner (2005). Model of coupled transient changes of Rac, Rho, adhesions and stress fibers alignment in endothelial cells responding to shear stress. *J. Theor. Biol.* 232, 569-585.

100. I. L. Novak, B. M. Slepchenko, A. Mogilner and L. M. Loew (2004). Cooperativity between cell contractility and adhesion. *Phys. Rev. Lett.* 93, 268109.

101. J. Denoth, E. Stussi, G. Csucs and G. Danuser (2002). Single muscle fiber contraction is dictated by inter-sarcomere dynamics. *J. Theor. Biol.* 216, 101-22.

102. L. Tskhovrebova, J. Trinick, J. A. Sleep and R. M. Simmons (1997). Elasticity and unfolding of single molecules of the giant muscle protein titin. *Nature* 387, 308-312.

103. K. K. Turnacioglu, J. W. Sanger and J. M. Sanger (1998). Sites of monomeric actin incorporation in living PtK2 and REF-52 cells. *Cell Motil. Cytoskeleton* 40, 59-70.

104. S. H. Zigmond (2004). Formin-induced nucleation of actin filaments. *Curr. Opin. Cell Biol.* 16, 99-105.

105. N. Watanabe, T. Kato, A. Fujita, T. Ishizaki and S. Narumiya (1999). Cooperation between mDia1 and ROCK in Rho-induced actin reorganization. *Nat. Cell Biol.* 1, 136-143.

106. P. Hotulainen, E. Paunola, M. K. Vartiainen and P. Lappalainen (2005). Actin-depolymerizing factor and cofilin-1 play overlapping roles in promoting rapid F-actin depolymerization in mammalian nonmuscle cells. *Mol. Biol. Cell* 16, 649-664.

107. D. Vavylonis, Q. Yang and B. O'Shaughnessy (2005). Actin polymerization kinetics, cap structure, and fluctuations. *Proc. Natl. Acad. Sci. U.S.A.* 102, 8543-8548.

108. J. W. Sanger, J. M. Sanger and B. M. Jockusch (1983). Differences in the stress fibers between fibroblasts and epithelial cells. *J. Cell Biol.* 96, 961-969.

109. A. M. Gordon, A. F. Huxley and F. J. Julian (1966). Variation in isometric tension with sarcomere length in vertebrate muscle fibres. *J. Physiol. (Lond.)* 184, 170-192.

110. L. Tskhovrebova and J. Trinick (2003). Titin: Properties and family relationships. *Nat. Rev. Mol. Cell Biol.* 4, 679-689.

111. K. J. Eilertsen, S. T. Kazmierski and T. C. S. Keller, III (1994). Cellular titin localization in stress fibers and interaction with myosin II filaments in vitro. *J. Cell Biol.* 126, 1201-1210.

112. T. J. Burkholder and R. L. Lieber (2001). Sarcomere length operating range of vertebrate muscles during movement. *J. Exp. Biol.* 204, 1529-1536.

113. F. Wang, E. V. Harvey, M. A. Conti, D. F. Wei and J. R. Sellers (2000). A conserved negatively charged amino acid modulates function in human nonmuscle myosin IIA. *Biochemistry* 39, 5555-5560.

114. A. H. Hu, F. Wang and J. R. Sellers (2002). Mutations in human nonmuscle myosin IIA found in patients with May-Hegglin anomaly and Fechtner syndrome result in impaired enzymatic function. *J. Biol. Chem.* 277, 46512-46517.

115. A. V. Hill (1938). The heat of shortening and the dynamic constants of muscle. *Proc. R. Soc. Lond., B, Biol. Sci.* 126, 136-195.

116. T. L. Hill (1981). Microfilament or microtubule assembly or disassembly against a force. *Proc. Natl. Acad. Sci. U.S.A.* 78, 5613-5617.

117. B. M. Millman (1998). The filament lattice of striated muscle. *Physiol. Rev.* 78, 359-391.

118. D. E. Rassier, W. Herzog and G. H. Pollack (2003). Dynamics of individual sarcomeres during and after stretch in activated single myofibrils. *Proc. R. Soc. Lond., B, Biol. Sci.* 270, 1735-1740.

119. I. A. Telley, J. Denoth, E. Stussi, G. Pfitzer and R. Stehle (2006). Half-sarcomere dynamics in myofibrils during activation and relaxation studied by tracking fluorescent markers. *Biophys. J.* 90, 514-530.

120. R. Horowits (2006). Nebulin regulation of actin filament lengths: New angles. *Trends Cell Biol.* 16, 121-124.

121. R. Littlefield, A. Almenar-Queralt and V. M. Fowler (2001). Actin dynamics at pointed ends regulates thin filament length in striated muscle. *Nat. Cell Biol.* 3, 544-551.

122. V. E. Galkin, A. Orlova, M. S. Vanloock, A. Shvetsov, E. Reisler and E. H. Egelman (2003). ADF/cofilin use an intrinsic mode of F-actin instability to disrupt actin filaments. *J. Cell Biol.* 163, 1057-1066.

123. J. Berro, A. Michelot, L. Blanchoin, D. R. Kovar and J. L. Martiel (2007). Attachment conditions control actin filament buckling and the production of forces. *Biophys. J.* 92, 2546-2558.

124. D. Vavylonis, D. R. Kovar, B. O'Shaughnessy and T. D. Pollard (2006). Model of formin-associated actin filament elongation. *Mol. Cell* 21, 455-466.

125. D. R. Kovar and T. D. Pollard (2004). Insertional assembly of actin filament barbed ends in association with formins produces piconewton forces. *Proc. Natl. Acad. Sci. U.S.A.* 101, 14725-14730.

126. M. R. Stachowiak and B. O'Shaughnessy (2009). Recoil after severing reveals stress fiber contraction mechanisms. *Biophys. J.* 97, 462-471.

127. K. Katoh, Y. Kano, M. Masuda, H. Onishi and K. Fujiwara (1998). Isolation and contraction of the stress fiber. *Mol. Biol. Cell* 9, 1919-1938.

128. Y. Luo, X. Xu, T. Lele, S. Kumar and D. E. Ingber (2008). A multi-modular tensegrity model of an actin stress fiber. *J. Biomech.* 41, 2379-2387.

129. A. Besser and U. S. Schwarz (2007). Coupling biochemistry and mechanics in cell adhesion: A model for inhomogeneous stress fiber contraction. *New J. Phys.* 9, 425.

130. K. Katoh, Y. Kano, M. Amano, H. Onishi, K. Kaibuchi and K. Fujiwara (2001). Rho-kinase-mediated contraction of isolated stress fibers. *J. Cell Biol.* 153, 569-583.

131. R. W. Ramsey and S. F. Street (1940). The isometric length-tension diagram of isolated skeletal muscle fibers of the frog. *J. Cell. Comp. Physiol.* 15, 11-34.

132. T. P. Lele, J. Pendse, S. Kumar, M. Salanga, J. Karavitis and D. E. Ingber (2006). Mechanical forces alter zyxin unbinding kinetics within focal adhesions of living cells. *J. Cell. Physiol.* 207, 187-194.

133. K. D. Costa, W. J. Hucker and F. C. P. Yin (2002). Buckling of actin stress fibers: A new wrinkle in the cytoskeletal tapestry. *Cell Motil. Cytoskeleton* 52, 266-274.

134. S. Deguchi, T. Ohashi and M. Sato (2006). Tensile properties of single stress fibers isolated from cultured vascular smooth muscle cells. *J. Biomech.* 39, 2603-2610.

135. M. M. Tirado and J. Garciadelatorre (1979). Translational friction coefficients of rigid, symmetric top macromolecules - application to circular cylinders. *J. Chem. Phys.* 71, 2581-2587.

136. Y. Tseng, T. P. Kole and D. Wirtz (2002). Micromechanical mapping of live cells by multiple-particle-tracking microrheology. *Biophys. J.* 83, 3162-3176.

137. P. A. Valberg and H. A. Feldman (1987). Magnetic particle motions within living cells - measurement of cytoplasmic viscosity and motile activity. *Biophys. J.* 52, 551-561.

138. A. R. Bausch, W. Moller and E. Sackmann (1999). Measurement of local viscoelasticity and forces in living cells by magnetic tweezers. *Biophys. J.* 76, 573-579.

139. R. O. Hynes and A. T. Destree (1978). Relationships between fibronectin (LETS protein) and actin. *Cell* 15, 875-886.

140. J. E. Heuser and M. W. Kirschner (1980). Filament organization revealed in platinum replicas of freeze-dried cytoskeletons. *J. Cell Biol.* 86, 212-234.

141. T. Watanabe, H. Hosoya and S. Yonemura (2007). Regulation of myosin II dynamics by phosphorylation and dephosphorylation of its light chain in epithelial cells. *Mol. Biol. Cell*, 605-616.

142. K. Murthy and P. Wadsworth (2005). Myosin-II-dependent localization and dynamics of F-actin during cytokinesis. *Curr. Biol.* 15, 724-731.

143. L. Haviv, D. Gillo, F. Backouche and A. Bernheim-Groswasser (2008). A cytoskeletal demolition worker: Myosin II acts as an actin depolymerization agent. *J. Mol. Biol.* 375, 325-330.

144. M. Dogterom and B. Yurke (1997). Measurement of the force-velocity relation for growing microtubules. *Science* 278, 856-860.

145. T. D. Pollard and G. G. Borisy (2003). Cellular motility driven by assembly and disassembly of actin filaments. *Cell* 112, 453-465.

146. M. Prass, K. Jacobson, A. Mogilner and M. Radmacher (2006). Direct measurement of the lamellipodial protrusive force in a migrating cell. *J. Cell Biol.* 174, 767-772.

147. M. Coue, V. A. Lombillo and J. R. McIntosh (1991). Microtubule depolymerization promotes particle and chromosome movement in vitro. *J. Cell Biol.* 112, 1165-1175.

148. K. Burridge, K. Fath, T. Kelly, G. Nuckolls and C. Turner (1988). Focal adhesions - transmembrane junctions between the extracellular-matrix and the cytoskeleton. *Annu. Rev. Cell Biol.* 4, 487-525.

149. L. P. Cramer (1997). Molecular mechanism of actin-dependent retrograde flow in lamellipodia of motile cells. *Front. Biosci.* 2, d260 - 270.

150. N. Endlich, C. A. Otey, W. Kriz and K. Endlich (2007). Movement of stress fibers away from focal adhesions identifies focal adhesions as sites of stress fiber assembly in stationary cells. *Cell Motil. Cytoskeleton* 64, 966-976.

151. M. A. Smith, E. Blankman, M. L. Gardel, L. Luettjohann, C. M. Waterman and M. C. Beckerle (2010). A zyxin-mediated mechanism for actin stress fiber maintenance and repair. *Dev. Cell* 19, 365-376.

152. J. Colombelli, A. Besser, H. Kress, E. G. Reynaud, P. Girard, E. Caussinus, U. Haselmann, J. V. Small, U. S. Schwarz, et al. (2009). Mechanosensing in actin stress fibers revealed by a close correlation between force and protein localization. *J. Cell Sci.* 122, 1665-1679.

153. R. J. Russell, S. L. Xia, R. B. Dickinson and T. P. Lele (2009). Sarcomere mechanics in capillary endothelial cells. *Biophys. J.* 97, 1578-1585.

154. M. P. Koonce, K. R. Strahs and M. W. Berns (1982). Repair of laser-severed stress fibers in myocardial non-muscle cells. *Exp. Cell Res.* 141, 375-384.

155. K. R. Strahs and M. W. Berns (1979). Laser microirradiation of stress fibers and intermediate filaments in non-muscle cells from cultured rat heart. *Exp. Cell Res.* 119, 31-45.

156. G. F. Elliott, J. Lowy and C. R. Worthington (1963). An x-ray and light-diffraction study of filament lattice of striated muscle in living state and in rigor. *J. Mol. Biol.* 6, 295-305.

157. L. M. Hoffman, C. C. Jensen, S. Kloeker, C. L. A. Wang, M. Yoshigi and M. C. Beckerle (2006). Genetic ablation of zyxin causes Mena/VASP mislocalization, increased motility and deficits in actin remodeling. *J. Cell Biol.* 172, 771-782.

158. K. M. Trybus and S. Lowey (1987). Assembly of smooth-muscle myosin minifilaments - effects of phosphorylation and nucleotide binding. *J. Cell Biol.* 105, 3007-3019.

159. T. D. Pollard (1986). Rate constants for the reactions of ATP-actin and ADP-actin with the ends of actin-filaments. *J. Cell Biol.* 103, 2747-2754.

160. M. R. Bubb, I. Spector, B. B. Beyer and K. M. Fosen (2000). Effects of jasplakinolide on the kinetics of actin polymerization - an explanation for certain in vivo observations. *J. Biol. Chem.* 275, 5163-5170.

161. P. Sampath and T. D. Pollard (1991). Effects of cytochalasin, phalloidin, and pH on the elongation of actin-filaments. *Biochemistry* 30, 1973-1980.

162. G. W. Greene, T. H. Anderson, H. Zeng, B. Zappone and J. N. Israelachvili (2009). Force amplification response of actin filaments under confined compression. *Proc. Natl. Acad. Sci. U.S.A.* 106, 445-449.

163. N. A. Medeiros, D. T. Burnette and P. Forscher (2006). Myosin II functions in actin-bundle turnover in neuronal growth cones. *Nat. Cell Biol.* 8, 215-226.